# Automatic quality assessment of end-to-side anastomoses using epicardial ultrasound images recorded from coronary artery bypass graft surgeries

Birgithe Kleemann Rasmussen, Linette Helena Poulsen and Mads Kristensen
Aalborg University
6 June 2019

AALBORG UNIVERSITY
STUDENT REPORT

**School of medicine and health**
**Biomedical Engineering and Infomatics**
Niels Jernes Vej 12
9220 Aalborg Øst
*http://www.smh.aau.dk/*

**Title**:
Automatic quality assessment of end-to-side anastomoses using epicardial ultrasound images recorded from coronary artery bypass graft surgeries

**Theme**:
Master's thesis

**Project period:**
Master, spring 2019

**Project group:**
18gr9413

**Participants:**
Birgithe Kleemann Rasmussen
Linette Helena Poulsen
Mads Kristensen

**Supervisor**:
Alex Skovsbo Jørgensen

**Number of pages:** 74

**Concluded:** 06/06/2019

**Abstract:**

*Introduction:* Intraoperative quality assessment of cardiac surgery is an essential tool to ensure the quality of the performed surgery and prevent potential revision. Coronary artery bypass graft (CABG) surgery has been shown to be related to a series of operative technical complications but remains one of the only major vascular surgeries that are not routinely intraoperatively assessed. Additionally, methods widely used for evaluating the anastomoses quality of the CABG-surgery are impractical to use or provide false insight into the quality of the anastomosis, to which epicardial ultrasonography (EUS) has been shown as a promising alternative as it can visualize structural information of the anastomosis. However, evaluation of anastomoses remains subjective to the physician, leading to cases of lacking or unnecessary revision to which the purpose of this project was to develop an objective quality assessment method.
*Methods:* 367 longitudinal EUS-frames recordings of anastomoses were available for this project to which 96 frames were used to develop the proposed methods. The methods comprised of a vessel detection algorithm, vessel lumen segmentation, and patency estimation. Two different segmentations were tested and compared: local-phase based snake and Chan-Vese to investigate which method produced the best anastomosis estimate.
*Results:* The methods were tested on the remaining 271 EUS-frames to which it was able to detect full or partial vessel structures from 89.67 % of the test frames, achieving an average Dice coefficient from sufficient detections of 0.8134 and 0.8187 for the local-phase based snake and Chan-Vese, respectively. This lead to a patency estimation of a maximum of 135 EUS-frames. Validation, when applying the patency estimation to corresponding manual annotations, resulted in the highest agreement of 88.15 % when compared with the Chan-Vese segmentation.
*Conclusion:* This project showed that the proposed method was able to detect and estimate the patency of anastomosis vessels from EUS-recordings, however, challenges persist when estimating the edges defined by manual expert annotations due to artifacts in the EUS-frames.

# Resumé

Koronararteriesygdom er på verdensplan en hyppig dødsårsag, hvor op mod hver syvende dødsfald estimeres at være relateret til sygdommen. Koronararteriesygdom kan behandles medicinsk og operationelt, hvortil koronararterie bypass graft (KABG) er en af de mest anvendte operationer i svære tilfælde, hvor flere stenoser forekommer. Under en KABG-operation bypasses en stenose eller okklusion med en arterie eller vene taget fra patientens brystkasse eller ben, hvilket er refereret til som graften. Graften syes på den forsnævrede koronararterie og aorta, hvorved blodforsyningen til myocardium genetableres. En række komplikationer er forbundet med operationen, hvilket kan medføre en forhøjet morbiditet og mortalitet. En årsag til, at post-operativ morbiditet og mortalitet kan opstå er, at anastomosen, som er forbindelsen mellem graft og koronararterie, kan indeholde en stenose som resultat af syningsfejl. I 9 % af KABG-operationer forefindes stenoser i anastomosen umiddelbart efter indgrebet. Anastomoserne kan kvalitetssikres intraoperativt for at nedsætte risikoen for postoperative stenoser, dog er der ikke på nuværende tidspunkt en kvalitetssikringsteknik, der anvendes på rutine basis under KABG-operationer. De typisk anvendte kvalitetssikringsteknikker fremstår desuden som værende upraktiske eller har tendens til at give et falsk indblik af anastomosekvaliteten. Hertil er epicardiel ultralyd en teknik, der har vist potentiale til at give strukturel information om kvaliteten af de udførte KABG-operationer. På nuværende tidspunkt vurderes kvaliteten manuelt, hvortil vurderingen kan forekomme subjektiv og dermed øge risikoen for at fejlvurdere stenosegraden af anastomosen.

Formålet med dette projekt har dertil været at udvikle en automatisk model, der på baggrund af epicardielle ultralydsbilleder, kan anvendes til objektiv vurdering af anastomosekvaliteten under KABG-operationer. Den automatiske model, udviklet i dette projekt, var inddelt i tre delelementer bestående af; karlumen detektering, karlumen segmentering samt en metode til estimering af karrenes åbenhed. I projektet var 367 epicardielle ultralydsbilleder inkluderet, hvor 96 af disse var anvendt til udvikling af modellen og de resterende 271 billeder var anvendt til validering af den udviklede model.

Til detektering af karlumen i epicardielle ultralydsbilleder blev der anvendt korrelationsberegninger mellem billederne og prædefinerede korrelationsmasker, som var designet ud fra udseende af karstrukturer. Hertil var det muligt at identificere en række mulige kar-kandidater, hvorudfra ét af disse blev valgt som det sande anastomose-kar. Udvælgelse af det sande anastomose-kar var baseret på sandsynlighed, hvor Mahalanobis afstande, baseret på specifikke features gældende for end-to-side anastomoser i længdesnit, blev anvendt. Denne detekteringsmetode resulterede i sufficient detektering af 91,15 % anastomoser, hvor en sufficient detektering blev defineret som en detektering, der havde en Dice koefficient over 0,5 sammenlignet med manuelle annoteringer af anastomose-karrene. Sufficiente detekterede karlumener blev anvendt som initiel kontur til segmenteringen, hvor to segmenteringsmetoder var designet for at opnå den bedst mulige estimering af karlumen. Disse bestod henholdsvis af en parametrisk og en geometrisk deformerbar model; local-phase based snake og Chan-Vese algoritme. Local-phase based snake opnåede en gennemsnitlig Dice koefficient på 0,8134 sammenlignet med manuelle annoteringer af anastomoserne, hvortil Chan-Vese algoritmen havde en gennemsnitlig Dice koefficient på 0,8187. Derudover viste resultaterne fra disse segmenteringsmetoder overensstemmelse i omridset af anastomosekarrene sammenlignet med de manuelle annoteringer.
Til estimering af åbenheden af karlumen blev diameteren af koronararterien og graften beregnet i 135 segmenteringer, hvorudfra stenoser kunne identificeres. Stenoser i anastomose-åbningen kunne estimeres med en nøjagtighed på 83,90 % og 88,15 % på segmenteringer udført af henholdsvis local-phase based snake og Chan-Vese algoritmen, sammenlignet med stenoser fundet i manuelle anastomose annoteringer. Den gennemsnitlige nøjagtighed af estimerede stenoser fundet i anastomoseåbning, hæl og tå var 76,02 % og 76,05 % udført på segmenteringer fra henholdsvis local-phase based snake og Chan-Vese algoritmen.

Den automatiske model udviklet i dette projekt, viste potentiale til at kunne anvendes som et beslutningsstøttesystem til kvalitetssikring af anastomoser under KABG-operationer. Dette vil være et system som vil kunne indikere mulige stenoser, for således at afhjælpe kirurgere under KABG-operationer. Dog bør modellen optimeres i forhold til at kunne identificere stenoser i flere typer anastomoser, derudover bør flere billeder inddrages af varierende anastomoser for således at gøre modellen mere robust over for mulige forskelligheder.

# Preface

This project is a master's thesis in Biomedical Engineering and Informatics at Aalborg University, department of Health, Science and Technology, conducted in the period 4th February to 6th June 2019 by group 19gr10403. Acknowledgements are given to the chief physician of thoracic surgery at Aalborg University Hospital for providing evaluations of epicardial ultrasonography images. Further acknowledgements are given to Alex Skovsbo Jørgensen for providing supervision and useful feedback during the writings of this project.

## Reading guide

This master is divided into six chapters. The first chapter presents an introduction to the project as an entirety. The second chapter contains the necessary background information for understanding the main purpose of the project. Chapter three describes the implemented methods to solve the problem derived from the previous chapter. Chapter four presents the results of the implemented methods. Chapter five contains the subjects for discussion of the implemented methods and the respective results, to which the sixth chapter states the conclusion of the project.
Citations are made in concordance to the Vancouver method: [citation number], e.g. [1]. If a citation refers to an entire section it is placed after a full stop, and if it refers to single sentence the citation is placed before full stop. If the following text relates to a specific source, the author of the source is stated followed by the citation.

# *Table of contents*

# 1. *Introduction*

Coronary artery disease (CAD) is a major cause of death globally, to which it was considered the leading cause of death worldwide in 2015. CAD develops when the coronary arteries are partially or completely blocked, resulting in insufficient blood flow to the myocardium, and consequently, may lead to heart failure or heart attack due to coronary ischemia. A typical cause of CAD is atherosclerosis that is a build up plaque in the blood vessels, which hardens and narrows the vessels. [1, 2, 3] The treatment of CAD is dependent on the degree of atherosclerosis, to which pharmacotherapy, percutaneous coronary intervention (PCI), and coronary artery bypass graft (CABG) surgery are possible treatments. CABG is one of the most performed surgeries and is often used for the more severe and complex cases of CAD, as it ensures more complete revascularization. [1, 4, 5] During a CABG-surgery the occluded coronary is bypassed with the use of a graft, which is a harvested artery or vein often taken from the patient's chest or leg. The graft is sutured to the aorta and the coronary artery, reestablishing the blood flow to the myocardium. [1, 6] Even though CABG is a commonly performed procedure, it is related to a series of complications, such as stroke and myocardial infarction, increasing the risk of morbidity and mortality. Studies have shown that $2-8\%$ of patients undergoing CABG experienced myocardial infarction, and $1-4\%$ had a stroke at a five year follow-up [5]. The long-term clinical outcome of CABG is dependent on early graft failure, which may be caused by sub-optimal patency in the graft or the bypassed coronary artery, as a result of suture errors during the surgery. [6, 7, 8, 9]

Despite the importance of early patency, no imaging tools are used on a routine basis to quality assess the patency intraoperatively during CABG-surgery [5]. However, several quality assessment methods are available, including angiography, transit time flow measurement (TTFM), and epicardial ultrasonography (EUS), to which different limitations and advantages are associated with each of these methods. Angiography, which is an imaging technique, is the golden standard. However, the technique is time consuming and usually not available in regular operating rooms, making it impractical to use for intraoperative quality assessment of anastomoses [5, 10]. TTFM is a technique used to measure blood flow using ultrasound. This method is associated with a high uncertainty when measuring the blood flow in vessels with minor sub-optimal patency, and it is not possible to locate stenoses in vessels [5, 11, 12, 13]. Lastly, EUS, which is also an imaging technique, is susceptible to subjective interpretation of the images to which the quality assessment may vary between operators. A strength of EUS is the ability to provide information about the internal anatomy of the myocardium and the location of the stenoses in the vessels, making it possible to evaluate possible suture errors [11, 14, 15]. EUS may be improved as a quality assessment technique by making the evaluation of the vessel patency more objective in order to avoid variations between operators.
Thus, in this project, it is aimed to design an objective quality assessment system in order to support the surgeons in the evaluation of the anastomoses in EUS-images during CABG-surgery.

# 2. *Background*

This chapter presents the necessary background knowledge for understanding coronary artery disease and the associated symptoms and treatment. In addition, coronary artery bypass graft surgery is described with the focus on quality assessment of the sutures, followed by a description of the current quality assessment techniques. This background presents information which leads up to the problem and the aim of this project.

## 2.1 Coronary artery disease

Coronary artery disease (CAD), also known as ischemic heart disease, is related to partial or complete blockage of the coronary arteries which supply the myocardium with blood. [1, 2] CAD is globally a major cause of death. In the United States approximately one of every seven deaths in 2014 were related to CAD, and in 2015 it was considered the leading cause of death in the world, where 8.92 million deaths were estimated to have been due to CAD. [2, 3] Furthermore, it is expected that 14.2 % of all deaths in 2030 will be caused by CAD [16]. In 2017 the prevalence of CAD in the United States was estimated to be 16.5 million among Americans aged above 20 years, which was approximately 6.3 % of the adult population. These estimates were based on data from the National Health and Nutrition Examination Survey 2011 to 2014. Risk factors associated with CAD include age, sex, smoking, hypertension, hypercholesterolemia, diabetes mellitus, obesity, family history, and lifestyle. [1, 2]
Partial or complete blockages in the coronary arteries reduce coronary circulation, which may lead to heart failure or heart attack, as a result of coronary ischemia. The partial blockage is a build up of plaque consisting of lipids and necrotic tissue in the coronary artery resulting in a gradually local narrowing, known as a stenosis. The stenosis of the artery prevents a dynamic dilation of the vessels when the myocardium has an increased need for oxygen, e.g. during physical or emotional stress. When the diameter of the vessel lumen has decreased with 50 %, the myocardium may start to require more oxygen than what can be supplied resulting in myocardium ischemia. Complete blockage, known as occlusion, may suddenly occur in the case of a thrombosis at the stenosis, ceasing blood flow to parts of the myocardium. Thrombosis is a result of plaque rupture, which typically occurs for non-calcified plaques, where deposit in the plaque is released and coagulate, increasing the risk of sudden occlusion in the coronary arteries. If no immediate treatment is performed, the complete blockage of the coronary artery may ultimately lead to death. [4, 17, 18]

### 2.1.1 Symptoms

CAD can be divided into chronic coronary heart disease, also known as stabile angina pectoris, and acute coronary syndrome, including unstable angina pectoris, myocardial infarction, and sudden cardiac death. [1, 17]
Insufficient blood flow and oxygen supply to the myocardium may lead to different symptoms such as angina, dyspnea, syncope and pulmonary edema. Depending on the type of CAD the symptoms may vary or be non-existing. In patients with chronic coronary heart disease, angina during physical or emotional stress is usually one of the first experienced symptoms as temporary ischemia develops when the blood supply to the myocardium is insufficient. Stabile angina pectoris may progress towards acute angina pectoris where more protracted, intense attacks of pain occur while in rest. [1, 18, 19]

### 2.1.2 Atherosclerosis

A healthy coronary artery contains none to a small amount of plaque that does not restrict the blood flow to the myocardium. Such an artery is illustrated in Figure 2.1(a). A frequent cause of stenosis in an artery is coronary atherosclerosis, which is a protracted formation of atherosclerotic plaques. The early formations of plaque have a tendency to be located where there is a disruption in laminar blood flow and places with oscillating shear stress, e.g near branch points and inner curvatures or injured vessel walls. These vulnerable locations are characterized by an adaptive thickening of the innermost layer of the arteries, tunica intima. This thickening starts developing after birth, and through the years it will spread to the surrounding intima, to which plaque may cover most of the coronary arteries in elderly people. With large formations of plaques follows a great risk of stenoses and occlusions of the coronary arteries, either due to large regions of plaques blocking the blood flow or due to formations of thrombus. [1, 4, 17, 20, 21, 22]
Plaques are composed of mixtures of fibrous tissue, cells and lipids and are characterized as regions of thickened tunica intima, resulting in hardened and narrowed arteries. [1, 4, 17, 21] Plaque is formed when low-density lipoprotein (LDL)-cholesterol gathers in the intima resulting in accumulations of cholesterol engorged macrophages and later accumulations of smooth muscle cells and lipid rich necrotic debris. [1, 21] In Figure 2.1(b) an artery with plaque formations resulting in a stenosis of the vessel lumen, is illustrated.

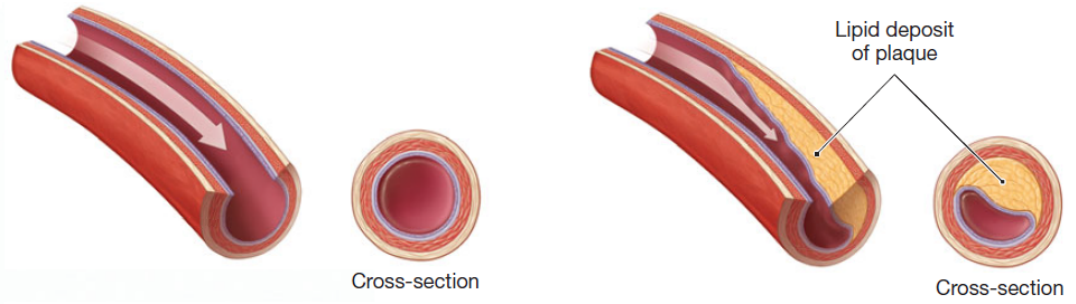


**(a)** *Healthy artery* **(b)** *Narrowed artery*

***Figure 2.1:*** *Illustration of a healthy artery and a narrowed artery containing plaques on the inner most layer, tunica intima. Edited from [18].*

### 2.1.3 Diagnosis of coronary artery disease

Diagnosis of chronic CAD is based on several examinations, where the initial examination is an evaluation of symptoms, risk factors, and tests with resting electrocardiography (ECG). Abnormalities in the ST segment and T waves in the ECG-signal might suggest angina and an abnormal Q wave might suggest myocardial infarction, both indicating the presence of CAD. However, not all people with CAD, especially stable angina, show signs of CAD in an ECG-test, making stress test ECG relevant for people who are able to exercise. During a stress test the individual is instructed to perform exercises while their ECG is being measured to investigate if any indications of CAD appear. Approximately 50 % of patients with a normal resting ECG-signal, show irregularities during stress test ECG when having an episode of angina pectoris. However, the diagnostic value of ECG is limited, thus diagnostic imaging techniques are recommended. [1, 23, 24]
Magnetic resonance imaging (MRI), and computed tomography (CT) with an intravenous contrast agent, and coronary angiography may be used to visualize the coronary arteries. The golden standard imaging tool for diagnosis of CAD is angiography, however invasive coronary angiography should not be performed as an initial test. [1, 19, 25] Invasive coronary angiography is used to visualize the coronary arteries directly to examine the degree of stenoses and occlusions, and is performed by inserting a catheter into a blood vessel in the arm, groin, or upper thigh. Afterwards, the catheter is moved towards the coronary arteries, usually guided by X-ray images. A contrast agent is then injected directly into the coronary arteries to highlight the vessels on X-ray images, where potential stenoses and occlusions may be visible as narrowed or blocked vessel lumens. [1] If patients have a low risk of having severe CAD based on symptoms and initial tests, CT- or MRI-angiography are

preferable, since they are non-invasive imaging alternatives to the traditional coronary angiography. CT-angiography is the more popular choice, because of faster acquisition time and spatial resolution, however, MRI-angiography is more suitable for people with poor renal function, since no contrast agent is necessary. [26]

## 2.2 Treatment of CAD

The treatment of CAD depends on the degree of atherosclerosis, thus the goal is to decrease the frequency and severity of angina symptoms experienced with CAD. Furthermore, it is attempted to reduce the incidence of acute coronary syndromes, prolong life, and enhance the quality of life. These goals can be accomplished by decreasing myocardial oxygen consumption and/or increasing myocardial oxygen supply, whereas three options for treatments are at disposal; pharmacotherapy, percutaneous coronary intervention (PCI), and coronary artery bypass grafting (CABG). The treatment depends on the severity of the CAD, number and positions of the atherosclerotic lesions and is decided by a multidisciplinary heart team. To determine the treatment, different risks factors are evaluated, including age, gender, and medical history. [1, 4, 5, 16, 19]
Pharmacotherapy typically comprises medication which purpose is to decrease blood pressure, heart rate, and cholesterol, so the risk for angina pectoris and myocardial infarction decreases [4]. In cases of multivessel CAD, pharmacotherapy may be insufficient and instead myocardial revascularization procedures, PCI and CABG, are performed [4, 5, 27].
PCI is a minor invasive operation where a balloon enclosed by a stent is directed up to the coronary artery stenosis using a catheter and a guidewire through an incision e.g. in the groin. The balloon with the stent is dilated and the stent is implanted in the vessel to scaffold the vessel. The stent is often covered in antimitotic drugs which are slowly released in the vessel wall with the purpose to inhibit cell proliferation and thereby prevent restenosis. The procedure is guided using angiography. [1, 28, 29] A step by step illustration of PCI is shown in Figure 2.2.

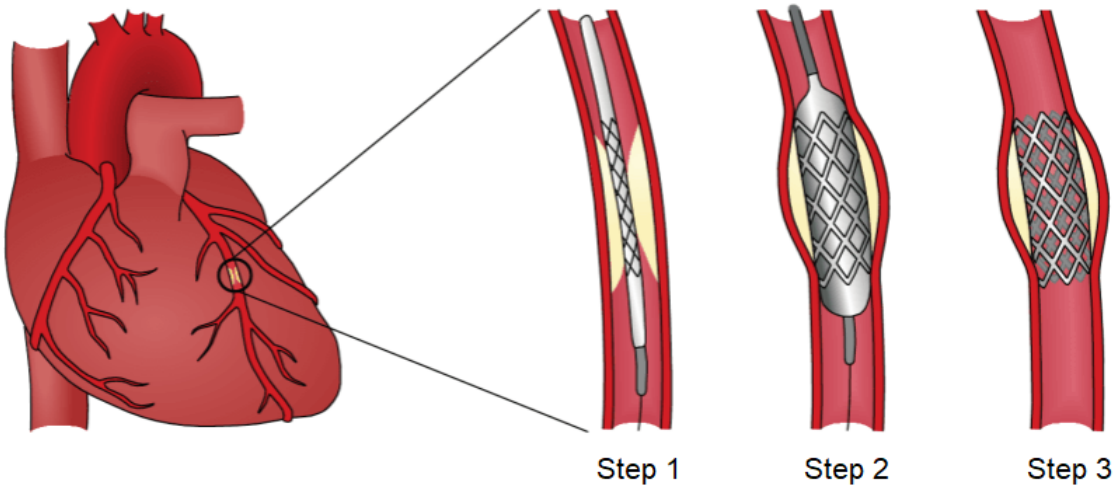


***Figure 2.2:*** *Illustration of a heart with a stenosis in a coronary artery which is treated by PCI. Step 1 illustrates the balloon enclosed by a stent in the coronary artery stenosis. Step 2 illustrates that the balloon is dilated, and step 3 illustrates that the balloon is removed and the stent is implanted to scaffold the vessel. Edited from [1].*

CABG is often used for more complex and severe CAD, including left main coronary artery stenoses or multivessel CAD, often with stenoses in more than three coronary branches, ensuring more complete and safe revascularization. [1, 4, 7, 16, 19, 30, 31] It is one of the most commonly performed operations with an average at a rate of 44 per 100,000 individuals stated by the Organisation for Economic Cooperation and Development [5].
The CABG-procedure is a comprehensive operation where the heart is exposed from the chest. The purpose of the operation is to bypass the coronary artery stenosis and/or occlusion to re-establish

the blood flow in the coronary circulation using the patient's own artery or vein as a graft. The graft is a vessel harvested from the patient during the procedure and is sutured on onto the aorta and to the native coronary artery beyond the stenosis or occlusion to establish the bypass. The CABG-procedure is illustrated in Figure 2.3(a).
The graft vessel used in CABG can be both an artery and a vein, where the artery is usually the left internal mammary artery (LIMA) that is taken from the chest, and the vein is often taken from the leg and is known as a saphenous vein. [1, 6] The venous bypass graft is the most commonly used graft in the procedure because it is less technical demanding than harvesting of the LIMA. However, the artery graft provides better results according to the long-term patency and outcome. [6]

The suture establishment between the graft and coronary artery is known as an anastomosis and is often performed as a side-to-side suture or an end-to-side procedure, where the side of the graft is connected to the coronary artery, or the end of the graft is sutured to the side of the coronary artery, respectively. The bypassed section of the coronary artery before the anastomosis is referred to as the heel and the area after the anastomosis following the blood flow is known as the toe. [6, 7] In Figure 2.3(b) the anastomosis types are illustrated with heel and toe outlined.

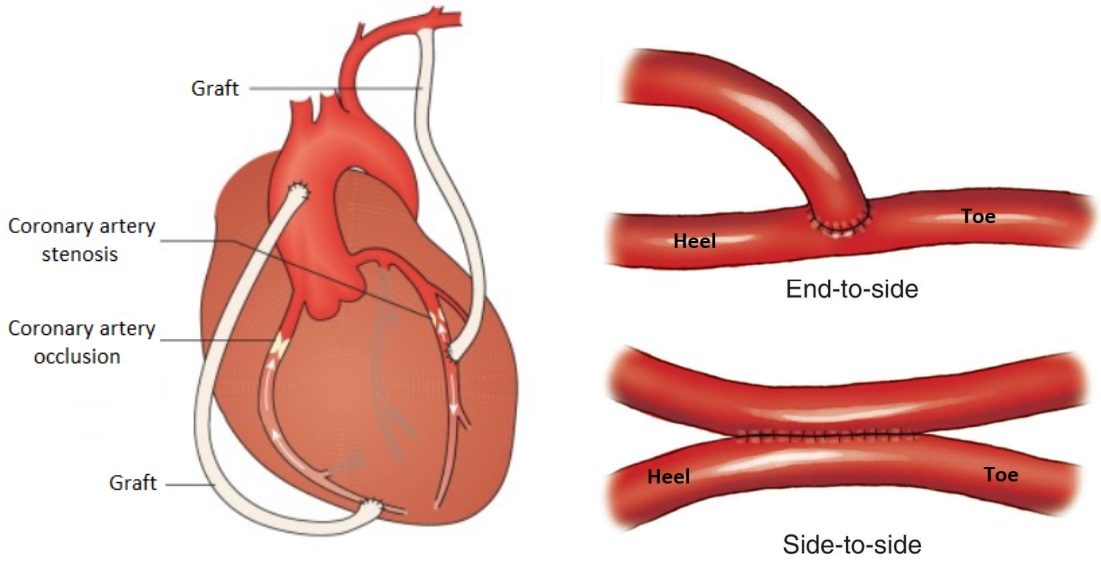


**(a)** *CABG-procedure* **(b)** *Anastomosis suture*

***Figure 2.3:*** *An illustration of CABG, where the bypass is established with grafts from the aorta to the coronary arteries after the stenosis or occlusion. Edited from [1]. And an illustration of the suture types; end-to-side and side-to-side with heel and toe marked. Edited from [32].*

The CABG-procedure is performed through a median sternotomy to expose the heart. The procedure can be performed on a beating heart, also known as off-pump coronary artery bypass grafting (OPCABG), or the heart can be stopped using a cardiopulmonary bypass machine, which is known as the conventional procedure. The cardiopulmonary bypass machine maintains the blood circulation where a pump substitutes for the heart and an oxygenator oxygenates the blood [1].
If the operation is performed on a beating heart, the region of interest is stabilized to avoid movement, while the rest of the heart still beats. OPCABG is a more technically demanding procedure but may be beneficial in terms of complications of cardiopulmonary bypass, for instance, increased blood-brain barrier permeability, stroke, respiratory failure, or systemic inflammatory reaction syndrome. [1, 5, 16, 19] Furthermore, a minimally invasive direct coronary artery bypass grafting (MIDCABG) procedure can be performed to avoid a comprehensive operation where a sternotomy is performed. Instead, the bypass operation is performed through a thoracotomy, and the heart is not stopped under the procedure. Thus, MIDCABG possesses the same advantage as OPCABG by avoiding cardiopulmonary bypass. Moreover, the operation is beneficial since it is a minor invasive procedure compared to the conventional bypass techniques, regarding the recovery period and reduced risk of infections. However, concerns regarding anastomoses quality have been expressed because the

procedure is performed on a beating heart through a small incision in the chest, which may be challenging. [14, 33, 34]

### 2.2.1 Importance of early patency

Even though CABG is used to treat CAD, it is still related to a series of complications and risks in mortality and morbidity. The complications include e.g. stroke, renal failure, myocardial infarction, and death. Follow-up trials of CABG show an all-cause mortality of 5 to 15 % as well as myocardial infarction in 2 to 8 % and stroke in 1 to 4 % at a five year follow-up. [5]
A study by Haaverstad et al. [35] has shown that in OPCABG up to 9.9 % of distal anastomoses require revision, based on Transit time flowmetry (TTFM) quality assessment [35]. Similarly, by using angiographic quality assessment in both MIDCABG and conventional CABG up to 9 % of patients show significant stenosis immediately or during short term follow-up [34, 36].

The long-term clinical outcome is dependent on the early patency of the graft and anastomosis after CABG-surgery [6, 7, 8, 9]. A study by Goldman et al. [8] has shown that if a LIMA graft was patent within the first week of surgery, there is an 88 % chance that it will remain patent 10 year post-surgery [8]. The patency of the graft and anastomosis can be evaluated by the FitzGibbon grading system, which divides the patency into three grades; A, B, and O [34, 37]. The definitions for the three grades can be seen in Table 2.1.

| Grade | Definitions |
|---|---|
| A | Excellent graft with unimpaired runoff |
| B | Stenosis reducing caliber of proximal or distal anastomoses or trunk to <50 % of the grafted coronary artery. |
| O | Occlusion |

***Table 2.1:*** *FitzGibbon grading system for patency of the vessels of the anastomosis. [34, 37]*

Early graft failure may be caused by sub-optimal patency of the graft and anastomosis, that in turn may be as a result of surgical technical complications. [5] These complications may occur due to the challenges of performing CABG, such as identifying the ideal anastomosis site as fat and myocardium may cover parts of the coronary arteries, as well as the presence of plaque and calcification within the coronary arteries that may complicate suturing of the graft and coronary artery [38].

### 2.2.2 Anastomosis errors

During CABG-procedure sub-optimal patency may occur due to different surgical errors. These errors are typically suture related, and can result in surgical stenoses of the coronary artery, graft, and/or in the anastomosis orifice. The use of epicardial ultrasonography (EUS) may display the location of such errors along with its type of error. Known suture errors are; pursestring effect, cross-over, oversutured heel or toe, and deep toe stitch as shown in Figure 2.4.
Pursestring happens when sutures are tightened too hard before being fashioned, resulting in a narrowing of the orifice in the anastomosis [11, 14]. An example of a pursestring suture is shown in Figure 2.4(a), where the anastomosis appears obstructed in the EUS-image. Cross-over sutures occur in cases where a stitch catches the opposite side of the anastomosis, to which the sides may be pulled towards each other causing sub-optimal patency [11, 14]. In a longitudinal EUS-image this may be displayed as a fixed obstruction inside the vessel lumen, as shown in Figure 2.4(b). Similarly, the oversutured heel and toe are cases where sutures near the heel and toe catch adjacent tissue of the anastomosis which causes either the heel or toe to be more enclosed, to which an oversutured toe is illustrated in Figure 2.4(c) [14]. Another similar suture is the deep toe stitch which is an error near the toe of the anastomosis. Instead of a stitch catching the opposite side of the anastomosis it catches the coronary artery and thereby causes a narrowing in the coronary artery, as shown in Figure 2.4(d) [11].

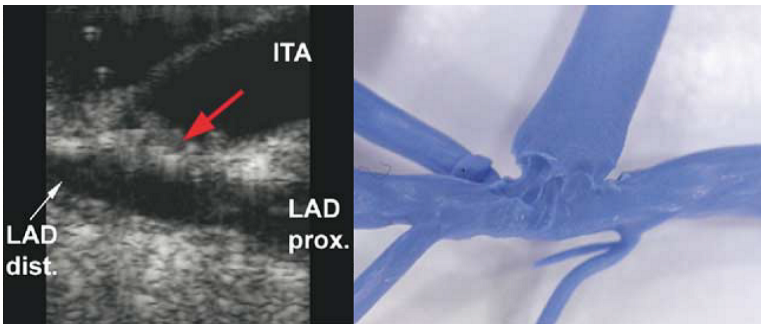


**(a)** *Pursestring suture, shown in EUS-image with associated cast, causing narrowing of the anastomosis. Edited from [11].*

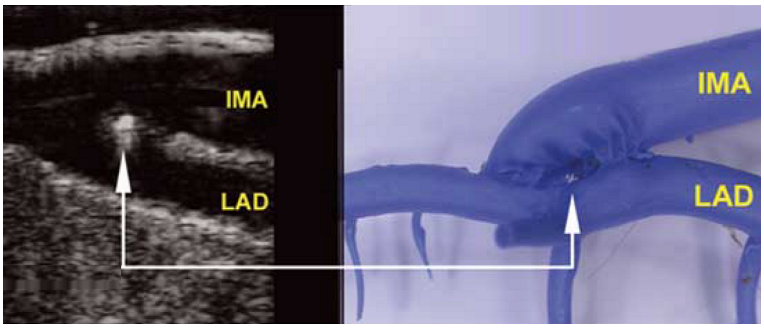


**(b)** *Cross-over suture, shown in EUS-image with associated cast, causing a narrowing in the middle of the anastomosis. Edited from [14].*

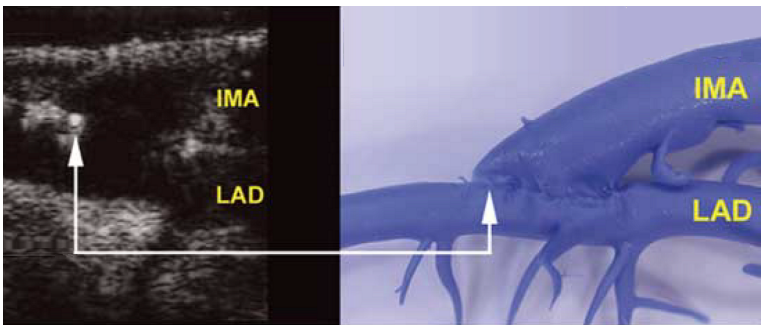


**(c)** *Oversutured toe, shown in EUS-image with associated cast, causing narrowing of the anastomosis at toe site. Edited from [14].*

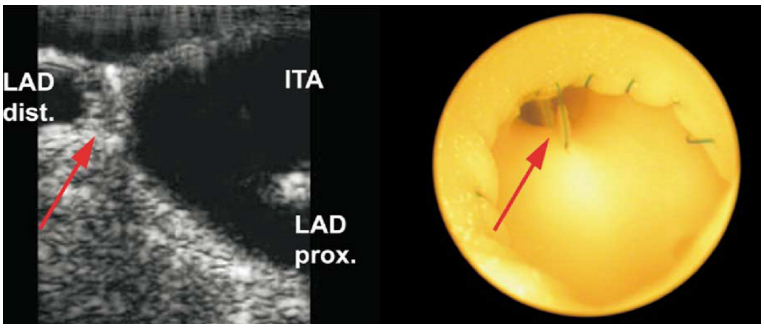


**(d)** *Deep toe suture, shown in EUS-image with associated angioscopic image with entry from ITA, causing obstruction of the coronary artery at toe site. Edited from [11].*

***Figure 2.4:*** *Visualization of different types of suture errors in anastomoses in longitudinal EUS-images with a corresponding anastomotic cast or angioscopic image. LAD: Left Anterior Descending Artery, IMA: Internal Mammary Artery (Graft), ITA: Internal Thoracic Artery (Graft).*

## 2.3 Quality assessment of anastomoses

Despite the importance of early patency, CABG is stated by Head et al. [5] to be the only major vascular surgical procedure that is not intraoperatively assessed using imaging tools on a routine basis. As shown in Figure 2.4 EUS may be used for quality assessment of the anastomosis allowing the surgeon to immediately perform revision of the anastomosis to ensure optimal patency in the vessels before closing the chest [11, 14]. However, EUS is one of several imaging tools available for intraoperative quality assessment of anastomoses, where tools such as angiography and TTFM are more commonly used in clinical practice. [10, 39]

### 2.3.1 Angiography

It is possible to assess the patency along the graft and coronary arteries through imaging techniques such as angiography that is considered to be the clinical gold standard allowing for an evaluation of the internal structure and lumen of the graft and anastomosis can be performed. [10] Angiography quality assessment of the bypass graft is normally performed post-surgery [6], but can also be used intraoperatively [5]. Examples of angiograms are illustrated in Figure 2.5. In Figure 2.5(a) a stenosis is visualized, shown as the narrowing of the coronary artery. In Figure 2.5(b) the lumen of the artery is dilated after PCI re-vascularization. [4]

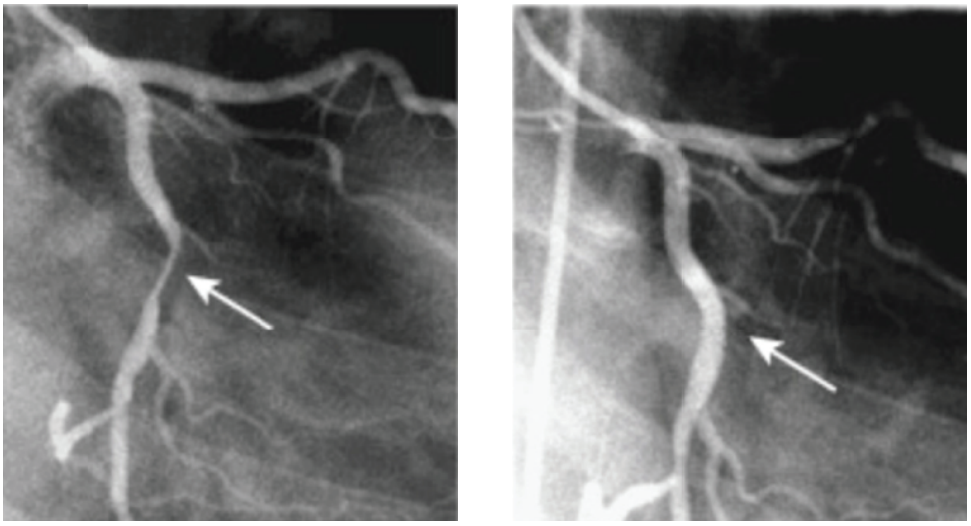

**(a)** *Before PCI re-vascularization* **(b)** *After PCI re-vascularization*

***Figure 2.5:*** *Angiograms showing the coronary arteries before and after a PCI re-vascularization. Edited from [4].*

However, drawbacks of using intraoperative angiography is expressed, as it is costly and may be time consuming to perform. Additionally, angiography is often not available in regular operating rooms, making it impractical to use intraoperatively on a routine basis. Alternatively, surgeries would have to be performed in a hybrid operating room. [5, 10] Furthermore, quality assessment using angiography can be challenging and exposes patients to large contrast volumes, and in rare cases the catheter may injure the graft or artery [6]. Given the impractical use of angiography, alternative methods for quality assessment of the bypass graft is available from which the most widely used is TTFM. [5]

### 2.3.2 Transit time flow measurement

Transit time flow measurement (TTFM) is a widely used intraoperative quality assessment method during CABG-surgery, where blood flow through the graft and anastomosis is measured. The transit time flow is measured with the use of a probe containing two transducers placed on opposite sides or the same side of a vessel with a small displacement in relation to each other along the flow direction. Ultrasound (US)-signals are transmitted through the blood in both directions between the two transducers, as illustrated in Figure 2.6. The transit time is then measured to calculate the flow, which is possible since the velocity of the sound waves varies depending on the flow direction. [39, 40, 41]

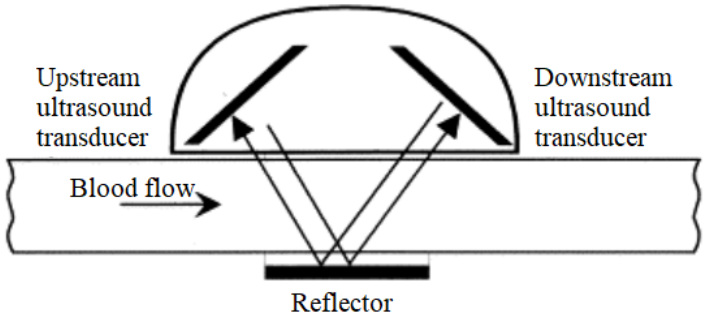


***Figure 2.6:*** *Illustration of the TTFM-procedure. Edited from [42].*

Additionally, a pulsatility index can be obtained from the TTFM-signal, which estimates the resistance of the blood flow. The pulsatility index is calculated by utilizing the maximum, minimum, and mean flow, which can be found in a TTFM-signal, as illustrated in Figure 2.7.

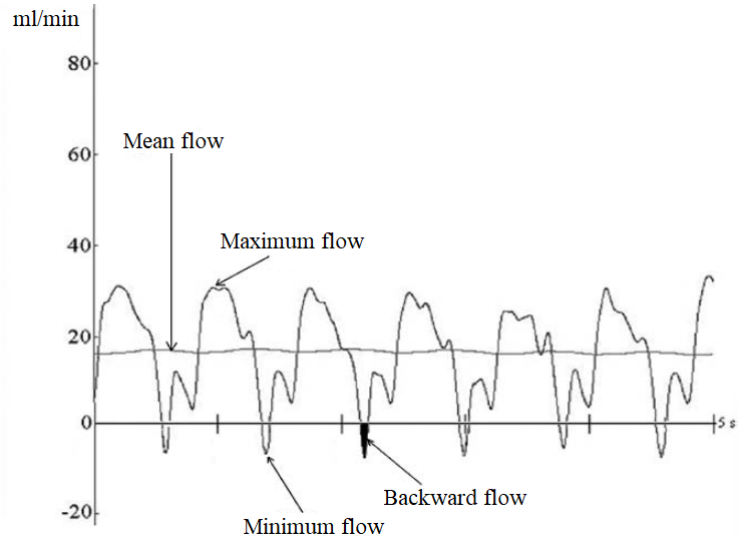


***Figure 2.7:*** *An example of a TTFM-signal where mean, maximum, and minimum flow as well as backward flow are indicated. Edited from [43].*

Stenoses and occlusions will affect the pulsatility index. However, other elements, such as blood pressure, competitive flow, and peripheral resistance might also have an influence on the flow, making it unclear what the cause of a possible high pulsatility index might be. [41] The performance of TTFM is sufficient when assessing truly good or severely stenosed anastomoses, where the stenoses are greater than 75 %, while the performance is limited when assessing grafts with minor anomalies giving false negative results and evaluations of the pulsatility index. Furthermore, the TTFM does not give precise information about where a stenosis might be located. [5, 11, 12, 13].
TTFM interpretation is also a subject of debate as there are no universally accepted threshold

criteria for when a graft is considered failed or not [39]. Interpretation of intermediate stenosis from TTFM may vary between surgeons, making the decision for anastomosis revision subjective [13].
A study by Di Giammarco et al. [12] shows an example of the limitations associated with TTFM for quality assessment by combining it with EUS. The example showed a TTFM mean flow and pulsatility index outside cut-off values indicating a failed anastomosis, but EUS-images showed clear patency through the anastomosis [12]. By combining the two modalities the study was able to avoid 37 unnecessary revisions of anastomoses than if evaluated on TTFM alone, and increased the positive predictive value from 10 to near 100 %. This indicates the importance of the morphological insight of anastomoses for quality assessment since TTFM may result in unnecessary revision or only detect severe stenosis $> 75$ %. [12]

### 2.3.3 Epicardial ultrasonography

The idea of using epicardial ultrasonography (EUS) for coronary anastomosis quality assessment was tested back in 1987 [44], but technical limitations of the transducer's size made it impractical, and prevented it from widespread use. Smaller transducers, used in recent studies have shown to be more practical, since it is easier to access and assess the anastomosis sites. [11, 14, 15]
EUS possesses several uses during CABG in terms of estimating optimal placement of the anastomosis, as well as it may display the internal anatomy and dimensions of the anastomosis using US. This makes it possible to detect complications resulting in sub-optimal patency, such as errors in the anastomosis, or detection of stenosis in the native coronary artery, as shown in Figure 2.4. [14, 15] Stenosis would be observed as a small to prominent narrowing of the vessel lumen, and patency can simply be measured as the diameter of the lumen at different marked areas of the anastomosis [14]. The anatomical structure of the anastomosis can be visualized in both cross sectional and longitudinal scans, where an example of a longitudinal EUS-scan is shown in Figure 2.8.

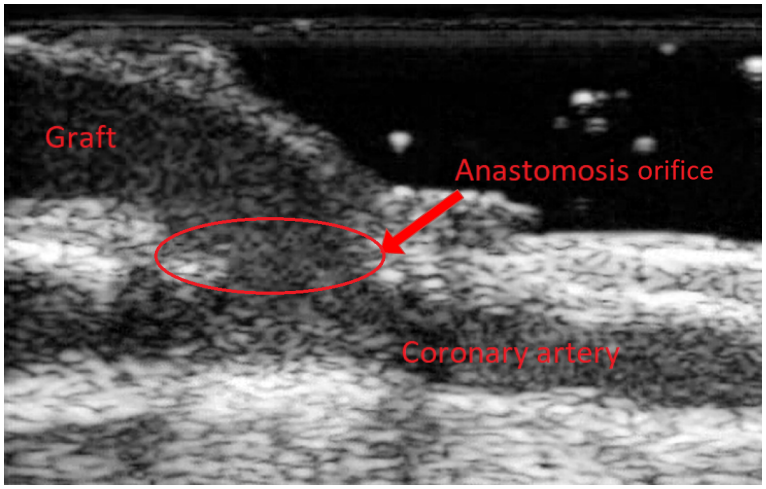


***Figure 2.8:*** *Longitudinal EUS-image of the coronary artery, graft, and anastomosis orifice.*

EUS may also differentiate between stenosis caused by calcifications or surgical errors, based on reflective information and shadowing in the image. This was shown to be a strength of the EUS compared to angiography in a study by Budde et al. [11], where this differentiation was not visible in the angiogram. [11] However, EUS is susceptible to subjective interpretation to which the quality assessment of an anastomosis may vary between operators [11] and interpretation of the scan may not always be immediate, to which the evaluation of the anastomoses is prolonged. Thus, the use of EUS to quality assess CABG-procedures requires some degree of training to accomplish a mutual interpretation of the visualization. [15]

## 2.4 Related works for vessel segmentation

The available intraoperative techniques for quality assessment of CABG are not used on a routine basis. Furthermore, several limitations are present such as the impractical use of angiography and the low performance and inadequate information of location using TTFM. Consequently, EUS shows advantages over these modalities, thus EUS remains the focus through the remaining project. Quality assessment of anastomoses is still subjectively evaluated, which may result in either unnecessary or lack of revision. To support surgeons during CABG, an objective intraoperative quality assessment framework may be beneficial to determine optimal anastomosis patency.
Studies utilizing EUS-images for quality assessment were investigated. However, a limited amount of studies addressing objective intraoperative quality assessment of anastomoses was found. Thus, the literature search was expanded to include the quantification of other vessels through the use of US-images.

A study by Jørgensen et al. [45] performed segmentation of vessel lumen in order to determine the stenotic rate of the anastomosis performed on healthy porcine vessels. This was performed on cross sectional EUS-images using active shape models, where the quality of the anastomosis was investigated at heel and toe site, and compared to a reference area of the native artery. This study used an automatic approach, to which watershed was implemented to detect the vessels without user interaction and initiate the active shape model segmentation. Using this method an average Dice similarity of $0.879 \pm 0.073$ was archived between model and ground truth segmentation. A limitation, pointed out in the study, is that the use of active shape models is data dependent, to which the lack of data may have caused the model to produce a larger error in smaller vessels, which may have affected accurate determination of stenotic rates. Furthermore, an absence of plaque may be considered, as the US-images were from healthy porcine vessels, and that plaque can cause shadowing which could affect the amount of tissue included in the segmentation. However, it is assumed that this may be accommodated if the method is trained on EUS-images containing plaque. [45]

Other studies addresses similar segmentation challenges of US-images, where a study by Santos et al. [46] automatically segmented the vessel lumen and boundaries of carotid artery in longitudinal US-images. These US-images were recorded using cervical US, and were thereby not recorded intraoperatively. Furthermore, the carotid arteries did not contain severe atherosclerosis. The segmentation of the vessels was performed using Chan-Vese level-set method, which Santos et al. [46] state to be a method robust to speckle noise and can adjust well to lumen boundaries in US-images. To avoid user interaction the Chan-Vese level-set method was initialized by contours found using sobel gradient operators. This study achieved a mean overlap of 96.73 % between manual and Chan-Vese segmentation. [46]

A semi-automatic approach for vessel segmentation is proposed by Ma et al. [47] which performed segmentation of vessels recorded in cross sectional plane by using local-phase based snakes. This study segmented the pelvic artery from swine and carotid artery as well as jugular vein from humans in US-images. The study provides no information about the presence of atherosclerosis and the amount of plaque. Local-phase based snakes is described as a method that recently has received increased attention as it is intensity-invariant compared to gradient-based segmentations. A Dice similarity of $0.919 \pm 0.021$ to $0.944 \pm 0.013$ was obtained between the automated and manual segmentation. This method was also compared to other snake based methods, and showed that the local-phase based snake was superior compared to gradient-based snakes when detecting the true edge of a vessel. The gradient based snakes were susceptible to detect false edges or overstep weak edges, as they were based on gradient information which may not always give accurate and robust segmentation as it was affected by poor image quality of US-images. [47]

Another semi-automatic approach for vessel segmentation is proposed by Hassan et al. [48] that used modified fuzzy c-means clustering to segment the carotid artery in US-images. The images were recorded on individuals with or without atherosclerosis with the purpose of plaque detection. Segmentation was performed on longitudinal US-images of the carotid artery, from which image features of the segmentation were used as input for a probabilistic neural network to classify the vessel as either normal or abnormal. This combination allowed for an accuracy of 98.4 %. [48]

## 2.5 Project aim

The focus of this project is quality assessment of anastomoses performed in CABG-operations, which is revascularization of coronary arteries that are partially or completely blocked as a result of atherosclerosis [1, 4, 18]. CABG is related to a series of operative technical complications in relation to the suture [5]. Studies have shown, by the use of angiography, that up to 9 % of patients have significant stenoses after CABG-operation during short term follow-up [34, 36]. Furthermore, the long-term clinical outcome depends on the early patency of the grafts and anastomoses [6, 7, 8, 9]. However, CABG is currently the only major vascular surgery that is not assessed using imaging tools intraoperatively on a routine basis [5].
Despite, the lack of use of intraoperatively quality assessment techniques during CABG on routine basis, some assessment methods are available but with different limitations. One of the available techniques is angiography, which is often used post-surgery due to its unavailability in the operating room, making it impractical to use intraoperatively. Additionally, it is a time consuming and costly procedure to perform. [5, 6, 10] Another quality assessment technique is TTFM, that utilizes flow information in the vessels to assess anastomoses. However, this technique also have limitations, including a low performance when assessing stenoses smaller than 75 %, which may lead to unnecessary revision of the anastomoses or false negative evaluations. Furthermore, TTFM provides no location information of the stenoses. [5, 11, 12, 13] Alternatively, EUS can be used as an intraoperatively quality assessment imaging tool. One of the strengths of EUS is that it is able to differentiate between surgical errors and calcifications in the coronary artery. Additionally, EUS can provide information about the internal anatomy and location of stenoses. [11, 14, 15] Commonly, the previously mentioned assessment techniques have no available automatic analysis tools, thus the techniques are susceptible to subjective interpretation to which the quality assessment may vary between operators. Due to the impractical use of angiography and the low performance and inadequate information of location using TTFM, EUS is the focus of this project. EUS may be improved by making the technique more objective to avoid the variations between operators. Thus, the aim of this project is to develop an automatic and objective quality assessment model using EUS-images with the intention of supporting surgeons in identifying sub-optimal patency in the anastomosis vessels.

### 2.5.1 Objectives

In this project it is chosen to investigate longitudinal EUS-images, given that previous studies have already identified vessels in cross-sectional US-images semi- or fully automatically [45, 47]. Furthermore, the project only includes images of end-to-side anastomoses, where both the graft and coronary artery are clearly visualized.
The aim is decomposed into the following objectives:

- Detection of the lumen of the anastomosis vessels
- Segmentation of coronary artery and graft
- Measure internal diameters of the coronary artery and graft
- Calculate, detect, and highlight areas of sub-optimal patency in the vessels
- Validate the performance of the detection-, segmentation-, and patency estimation algorithm

# 3. *Methodology*

This chapter presents a description and analysis of the available EUS-images. Afterward, the proposed methods for fulfilling the aim is described, followed by the method used for validation of detection, segmentation, and patency estimation.

## 3.1 Data description

EUS-sequences available in this project were obtained from patients who have undergone an on-pump CABG-procedure on Aalborg University Hospital. The images were recorded intraoperatively using the Medistim MiraQ Cardiac System with a 15 MHz L15 linear array probe. MiraQ is designed for cardiac surgery and combines US-imaging and TTFM for immediate assessment of the quality of CABG-procedure. The L15 imaging probe is a high-frequency US-probe and allows for direct contact with cardiac tissue. [49] The use of high frequencies results in a higher spatial resolution at the expense of attenuation of the US-waves, making high frequency transducers preferable when scanning superficial tissue, such as the exposed coronary arteries, as opposed to low frequency transducers which are more beneficial when scanning deeper tissues [50]. However, higher frequencies may result in increased speckle noise [51], which is shown as a granular pattern resulting in a decreased contrast resolution in the image and blurred edges between different tissue structures [52]. Speckle is caused by the scattering of the US-waves due to irregularities in tissue. [53]
During EUS-recording the probe was mounted on an EchoClip, as shown in Figure 3.1, to improve the image quality. The device stabilizes the imaging area with the use of two skin supports, where a cavity between the two supports prevents deformation of the vessel. The device is designed to keep the US contact gel in place, which increases the acoustic contact between the probe and the tissue. [54] With the EchoClip, the anastomosis vessels can both be recorded in the longitudinal and cross sectional plane, where an example of how the longitudinal scans are recorded, and the resulting output image of the scan can be seen in Figure 3.1.

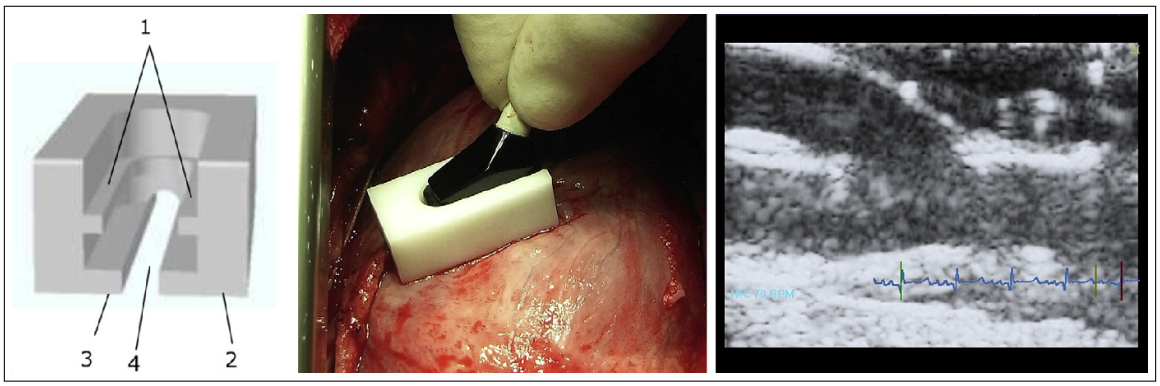


***Figure 3.1:*** *A three-dimensional illustration of an EchoClip device, where 1 is a fixing element that ensures that the US-probe is properly secured in the EchoClip, 2 and 3 refer to the skin supports, and 4 is the cavity where the vessel is placed to avoid deformation. The second image is an US-probe mounted on an EchoClip device recording longitudinal sequences of a vessel, and the resulting EUS-image. Edited from [54].*

In this project, only frames containing longitudinal end-to-side anastomoses were selected from the available EUS-sequences. Furthermore, the data set was limited to only include EUS-frames where the anastomosis orifice, heel and toe were clearly visualized. The EUS-frames were sorted on the basis of the expert manual annotations of the anastomosis vessels, to which longitudinal EUS-frames from 31 patients undergoing on-pump CABG-operation were available for this project. Some of these patients had more than one anastomosis, to which EUS-sequences from one patient could contain multiple anastomoses. A total of 367 EUS-frames were included, showing significant variations of the anastomoses.
The available data was separated into two sets; a development- and test set with associated manual annotations. EUS-sequences were randomly divided according to patients, thus all EUS-frames from a given patient were used for either development or test. The development set consisted of 96 EUS-frames from seven patients, and the test set consisted of 271 EUS-frames from 24 patients. The spatial resolution of the EUS-frames were $574 \times 632$ pixels.

### 3.1.1 Manual expert annotations

The manual expert annotations of the anatomical structures were performed on all included 367 EUS-frames by a researcher at Aalborg University. Different structures in the EUS-frames were annotated individually and labeled accordingly as either graft, coronary artery, plaque, suture error, side branch, or additional vessel structures in the frames, as shown in Figure 3.2(a). All the different manual annotation labels were sorted to suit the aim of this project, meaning that the individual labels needed to be directly influencing the patency of the anastomoses in both the graft and the coronary artery. This excluded labels such as side branches and additional vessel structures in the frames, as these were assumed irrelevant for the patency estimation of the anastomosis vessels.
A combined manual expert annotation was constructed, where the following labels were included; graft, coronary artery, plaque, and suture errors. These were included even if sections of the coronary artery or graft were separated into multiple segments in the EUS-frame. The combined manual expert annotation was constructed as a binary image, where pixels constituting the graft and coronary artery were labeled 1. Pixels constituting suture errors, plaque, and surrounding tissue to the vessel lumen were labeled 0. An example of manual expert annotations and the combined manual annotation are shown in Figure 3.2, where the individual labeled annotations in Figure 3.2(a) are sorted and combined in a binary segmentation in Figure 3.2(b).

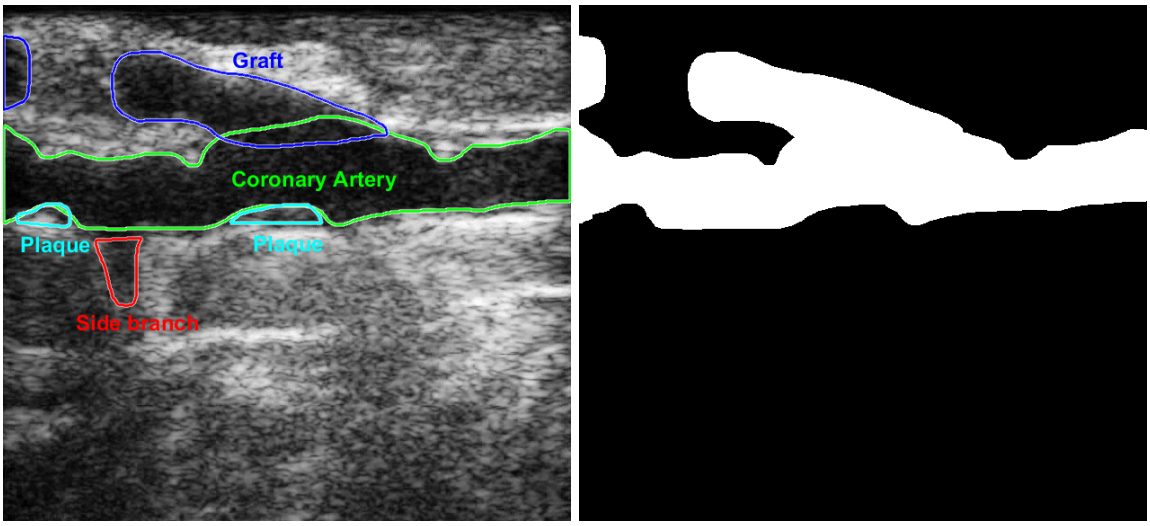


**(a)** *Manual expert annotations* **(b)** *Sorted and combined manual expert annotation*

***Figure 3.2:*** *An example of a manual expert annotations of individual elements present in the EUS-image, and the corresponding combined manual expert annotation, where only relevant structures are included.*

## 3.2 EUS-image appearance and analysis

The EUS-frames from the development set were analyzed to obtain descriptive characteristics and variability of the anastomosis vessels, plaque, and the surrounding myocardium. This information was used to support the design and development of the automatic quality assessment algorithm.
The appearance of the vessels in the EUS-images was characterized as a dark longitudinal region, corresponding to the vessel lumen, surrounded by brighter intensities representing the vessel wall and surrounding myocardial tissue, as seen in Figure 3.3 [55].

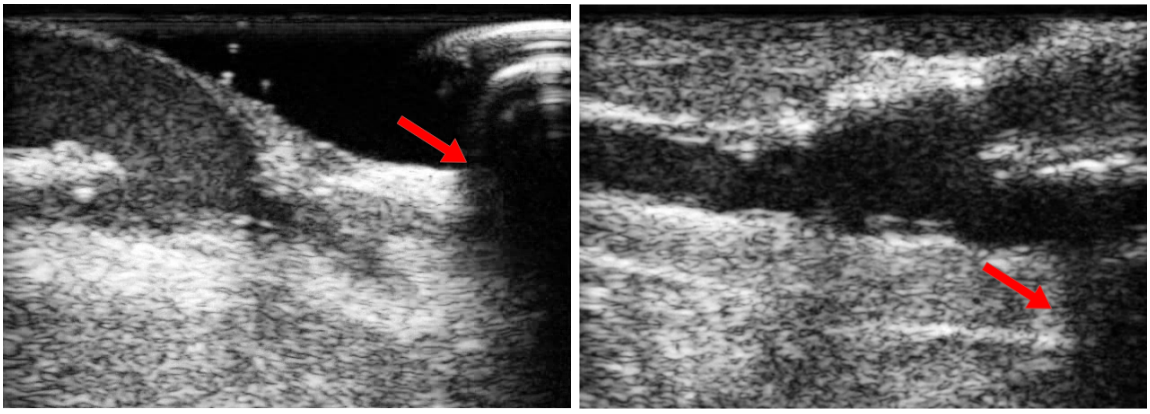

**(a)** *EUS-image with missing acoustic contact* **(b)** *EUS-image with shadowing as a result of plaque*

***Figure 3.3:*** *Longitudinal EUS-images with dark intensities in the graft (upper vessel) and coronary artery (lower vessel). The surrounding myocardial tissue consists of brighter intensities. Speckle is shown as a granular pattern visible in the tissue and vessel lumen. In (a) missing acoustic contact resulting in no structural information is pointed out, and in (b) shadowing as a result of plaque is pointed out.*

Common to all EUS-frames was that the graft was located above the bypassed coronary artery, and the anastomosis vessels appeared as a "y"-shape, as a result of the end-to-side suture. Given the placement of the US-probe, the anastomoses were typically orientated horizontally in the EUS-image. Furthermore, the location of the anastomoses were often centered in the image, but could vary between subjects. Additionally, the size and shape of the anastomoses appeared differently between subjects and frames.
Dependent on the recording, the EUS-frames expressed different artifacts, including speckle and missing acoustic contact, which can be seen in Figure 3.3(a). A lacking acoustic contact resulted in US-waves not being reflected in the tissue, thus no structural information of the tissue could be provided.
The presence of plaque in the EUS-frames could cause shadowing artifacts, depending on the type of plaque. The calcified plaque was shown as bright intensities which prevented structural information deeper in the tissue to be provided, as this plaque was hyperechoic. Likewise, the soft plaque was represented by high intensities, however, this type of plaque allowed underlying structured to be provided. A EUS-frame where a reduction in structural information is visible as a result of the presence of calcified plaque is shown in Figure 3.3(b).
To investigate the descriptive features of the anastomosis vessels in the EUS-frames, an analysis based on the manual expert annotations of the structures in the frames was performed. The manual annotations were used to isolate the vessels in the frames, allowing extraction of the descriptive properties of the vessels. This was done for all frames in the development data set. The properties that were seen as the most descriptive are listed in Table 3.1.

| | Mean | ± SD | Minimum | Maximum |
|---|---|---|---|---|
| Area | 52,055.729 | 19,126.948 | 19,600.000 | 87,394.000 |
| Mean intensity | 56.349 | 15.444 | 33.321 | 102.277 |
| MajorAxisLength | 557.465 | 158.797 | 238.764 | 766.860 |
| EquivDiameter | 252.771 | 49.108 | 157.973 | 333.577 |
| Extent | 0.473 | 0.100 | 0.272 | 0.697 |
| Orientation | -10.535 | 11.561 | -34.250 | 8.496 |
| Deformity | 0.031 | 0.005 | 0.024 | 0.043 |
| Ratio | 2.310 | 0.661 | 1.141 | 3.543 |
| WeightedCenterY | 203.442 | 72.959 | 103.400 | 402.352 |
| WeightedCenterX | 285.915 | 91.989 | 130.702 | 523.762 |

***Table 3.1:*** *Descriptive vessel lumen properties based on manual anastomosis annotations in the EUS-frames from the development data set. The values shown are the mean, standard deviation (SD), minimum, and maximum values for every property.*

In Table 3.1 the mean is an average calculated between all frames, where a corresponding standard deviation is shown along with the lowest and highest value for the given property. A property that described the number of pixels that make up the vessel lumen was the *area*, along with the vessel's *mean intensity*. In addition, the length in pixels when fitted within an ellipse, called *MajorAxisLength*, and diameter of a circle created with the same amount of pixels as the vessel lumen, called *EquivDiameter*, were investigated. Furthermore, the number of pixels of the vessel lumen that covers its bounding box, also known as *extent*, the *orientation* in a range of -90 to 90 degrees, the amount of *deformity*, which were calculated by dividing the boundary of the vessel with its area, the *ratio* of the bounding box, and lastly the *weighted centroids* of the vessel, weighted according to location and intensity of the vessel lumen were analyzed.

## 3.3 Proposed method

In order to fulfill the aim and objectives stated in section 2.5, the proposed method was separated in three constituent parts; vessel lumen detection, vessel lumen segmentation, and patency estimation, which were designed and implemented on the basis of the development set. The parts along with their flow are shown in Figure 3.4.

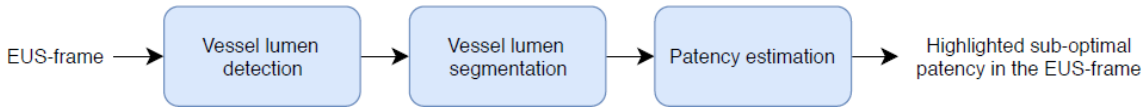


***Figure 3.4:*** *Flow of the proposed method. A EUS-frame was loaded into the algorithm. An initial contour of the vessel lumen was estimated using a detection algorithm and was used to initialize the segmentation of the anastomosis vessel lumen, which further was used to estimate the patency in the vessels. Lastly, the locations with sub-optimal patency were highlighted.*

EUS-frames were loaded into the algorithm and individually processed: 1) the vessel lumen detection algorithm that identified the vessel lumen of the coronary artery and graft and estimated an initial coarse contour of the anastomosis vessels. 2) The vessel lumen segmentation produced a fine contour estimation of the vessel lumen. 3) A patency estimation was performed based on the segmentation to objectively evaluate the patency of the vessels. Patency of the segmented vessel lumen was calculated to which areas of sub-optimal patency were identified and highlighted on the EUS-frames. Sub-optimal patency was determined using the same criteria as the FitzGibbon grading.

## 3.4 Vessel lumen detection

The vessel lumen detection was used to estimate the location, shape, and size of the anastomosis vessels, which further constituted an initial contour used for the vessel lumen segmentation. The detection was an essential part to automatically identify the vessels and assess the patency, and was divided into the following sections.

- Identification and exclusion of missing acoustic contact
- Search for vessel candidates based on structure and appearance
- Merging of vessel candidates
- Probability based selection of anastomosis vessels

Methods used as a part of the detection utilized both structural and intensity information in the EUS-frame to identify different structures, e.g. vessels, shadowing, and missing acoustic contact. A probability was assigned based on the characteristics of anastomosis vessels observed in EUS-images in section 3.2, where specific features were selected to identify the true vessels among several vessel candidates. It was desired to detect and outline a rough contour of the anastomosis vessels as one coherent object, including the graft and coronary artery, to obtain the best initial contour used to initialize in the segmentation, as in concordance with the appearance of the anastomosis vessels in the included EUS-frames.

### Identification and exclusion of missing acoustic contact

Missing acoustic contact was observed to appear in several EUS-frames and was considered problematic as it could remove edge information of the anastomosis vessels or appear similarly to side branches to the vessels. This could complicate the segmentation process of the true anastomosis vessels, thus it became relevant to identify and exclude these regions from the EUS-frames.
The regions showing missing acoustic contact were observed as larger areas of uniform intensities with a high reflection of US-waves at the top of the frame. The intensities of missing acoustic contact appeared often similar to the intensities of the vessel lumen, however, contained near to no speckle. Additionally, the regions were observed to be orientated vertically in the EUS-frame, where no structural information of the underlying tissue structure was provided. Examples of EUS-images with non-acoustic contact can be seen in Figure 3.3(a).
To identify these regions, a statistical texture analysis on the EUS-frames was performed. The analysis was based on intensity histogram features, where local entropy of the frames was calculated through equation 3.1. [56]

$$e = -\sum_{i=0}^{L-1} p(z_i) \cdot log_2(p(z_i)) \tag{3.1}$$

The output of the entropy filtering, $e$, was a map containing scalar values representing the statistical measure of randomness in the EUS-frames. High scalar values indicated high randomness, and lower values indicated low randomness. In the equation $p(z_i)$ was the corresponding histogram of the gray levels, $z$, in the respective frame, and $L$ represented the number of distinct gray levels. The entropy filtering was performed locally using a neighborhood kernel, which had a size of $25 \times 25$ pixels. This kernel size was chosen based on initial testing including several kernel sizes. The test showed that a smaller kernel size responded to smaller objects, resulting in many potential areas of missing acoustic contact, and a larger kernel size resulted in objects being merged in the frame. Thus, a kernel size of $25 \times 25$ was suitable for the detection of larger objects, such as areas of non-acoustic contact. The entropy filtering resulted in a reduction of the spatial dimensions, and to avoid this reduction, a symmetrical mirror padding was implemented.
It was intended that the entropy response would differentiate between tissue information and missing acoustic contact, given a uniformity of intensity in areas of missing acoustic contact, as seen in Figure 3.5(a). Thereby, these regions of missing acoustic contact would result in low randomness compared to the remaining frame containing a higher amount of speckle noise and texture information. In

Figure 3.5(b) an example of an entropy map produced from the EUS-frame shown in Figure 3.5(a) is shown.

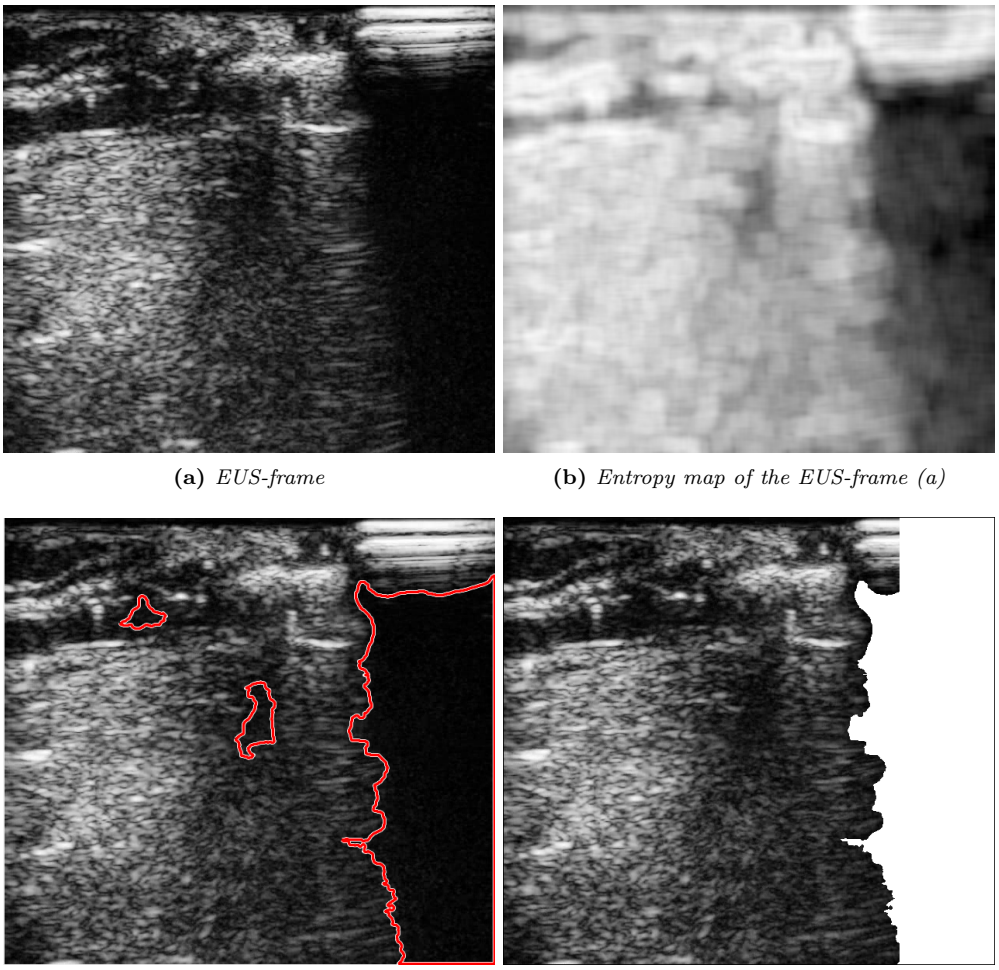

**(a)** *EUS-frame*

**(b)** *Entropy map of the EUS-frame (a)*

**(c)** *EUS-frame after identifying regions of low randomness*

**(d)** *EUS-frame after converting the pixels intensities of non-acoustic contact to 255*

***Figure 3.5:*** *Example illustrating the processes of identifying missing acoustic contact in an EUS-frame.*

As shown in Figure 3.5(b) the presence of speckle produces high entropy values, shown as bright intensities, and the lack of speckle, as seen in regions with shadowing or missing acoustic contact, provided low entropy values, shown as dark intensities. To separate the entropy map into regions of low and high randomness, the entropy map was binarized using a simple otsu threshold. In Figure 3.5(c) regions with low randomness are outlined. To avoid excluding objects located inside the vessel lumen as shown in the example, a criterion stating that the object had to be orientated in the range of $90 \pm 5$ degrees before being considered as missing acoustic contact. This range was specified based on an analysis of 25 EUS-frames from the development set showing missing acoustic contact, which were manually annotated. Based on the exclusion criteria, the two smaller objects in Figure 3.5(c) were not considered non-acoustic contact, and the major area to the right was considered as non-acoustic contact.
To further identify regions of missing acoustic contact, specifically the high reflective information above the uniform intensity areas, as seen in Figure 3.5(a), an additional criterion was defined. On a column by column basis, the amount of identified missing acoustic contact was compared to the length of the EUS-frame column. If the identified missing acoustic contact constituted 80 % or more of the column, the entire column was considered as missing acoustic contact. The 80 % threshold was based on the conviction, that the missing acoustic contact needed to be considerable before excluding more of the EUS-frame. The pixels in the identified objects which constituted the

missing acoustic contact, were changed to have a pixel intensity of 255 in the original EUS-frame, as shown in Figure 3.5(d). This was to clearly differentiate between areas of interest, which appeared dark, and the identified non-acoustic contact with the intention of simplifying forward operations of the detection. Given the previous mentioned criterion it was possible to identify some areas of shadowing, as these areas were orientated vertically in the frame and consisted of a low entropy.

### Search for vessel candidates based on structure and appearance

The anastomosis vessels needed to be identified in the EUS-frame in order to provide an initial contour for the segmentation. Identified vessel structures in the frame are referred to as vessel candidates and were found based on the structural characteristics and appearance of the anastomosis vessels.
Given that the appearance of the vessels was characterized by darker intensities in the vessel lumen surrounded by white pixels, templates with similar appearance were created, where an illustration of the template can be seen in Figure 3.6. Thus, information about the intensities, shape, and orientation of the vessels was used to detect vessel candidates by calculating the correlation between structures within an EUS-frame and the intensity appearance in the predefined templates. A normalized correlation between the EUS-frame and predefined templates was used as similarity measure, given that the vessels in the frames appeared recognizable and similar.
The templates were designed to roughly imitate the appearance of the vessels, by arranging pixels as a black tube, resembling the vessel lumen with white sections on either side of it, resembling the surrounding tissue. The tube consisted of pixels with intensities of 0, and the surrounding tissue consisted of pixel intensities of 255. To accommodate for the different orientations of the vessels, the templates were orientated accordingly; 0, 45, 90, and 135 degrees, as shown in Figure 3.6.

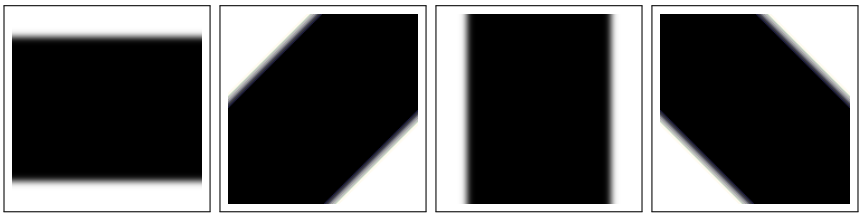

**(a)** *0 degree* **(b)** *45 degree* **(c)** *90 degree* **(d)** *135 degree*

***Figure 3.6:*** *Illustration of the four predefined templates with different orientations.*

The templates were further designed in three different sizes to accommodate for the varying vessel diameters in the EUS-frames. The sizes of the predefined templates were determined based on an analysis of the diameter of the anastomosis vessels in the 96 EUS-frames from the development set, to which the minimum and maximum diameters of the anastomosis vessels were found to be approximately 12 and 179 pixels, respectively. A template with a tube diameter of 12 pixels would not be beneficial due to the presence of speckle in the EUS-frames as these would correlate with the templates as well as the small vessels. Thus, it was chosen to create a template with a minimum tube diameter of 50 pixels. Furthermore, it was chosen to create a template with a maximum tube diameter of 200 pixels, due to a possibility of a larger vessel lumen diameter appearing in the test set. Additionally, a template with a tube diameter of 100 pixels was designed to accommodate for the large variation between the two templates. The dimensions of the templates varied depending on the orientation and the diameter. The templates orientated 0 and 90 degrees were designed with a length of 5, 10, and 20 pixels for each diameter, which was chosen to avoid elongation of the vessels. The templates with an orientation of 45 and 135 degrees had a length of 25, 50, and 100 pixels, for each diameter, which was necessary in order to properly represent an angle of a vessel.

In order to use the templates to locate the vessels, a normalized correlation calculation was performed between each template and EUS-frame. The normalized correlation was calculated using equation 3.2.

$$\gamma(u,v) = \frac{\sum_{x,y}[f(x,y) - \bar{f}_{u,v}][t(x-u,y-v) - \bar{t}]}{(\sum_{x,y}[f(x,y) - \bar{f}_{u,v}]^2 \sum_{x,y}[t(x-u,y-v) - \bar{t}]^2)^{0.5}} \tag{3.2}$$

Where $f$ was the original EUS-frame, $\bar{f}_{u,v}$ was the mean of the image of $f(x, y)$ in the region covered by the template, and $\bar{t}$ was the mean of the template intensities. [57] Perfect correlation would result in values of one, and a perfect inverse correlation would result in values of $-1$.
Correlation between the EUS-frame and the predefined templates, varying in size and orientation, resulted in 12 different correlation maps. Four correlation maps were obtained by adding the correlation maps at different scales in the same orientation. Examples of these are illustrated in Figure 3.7.

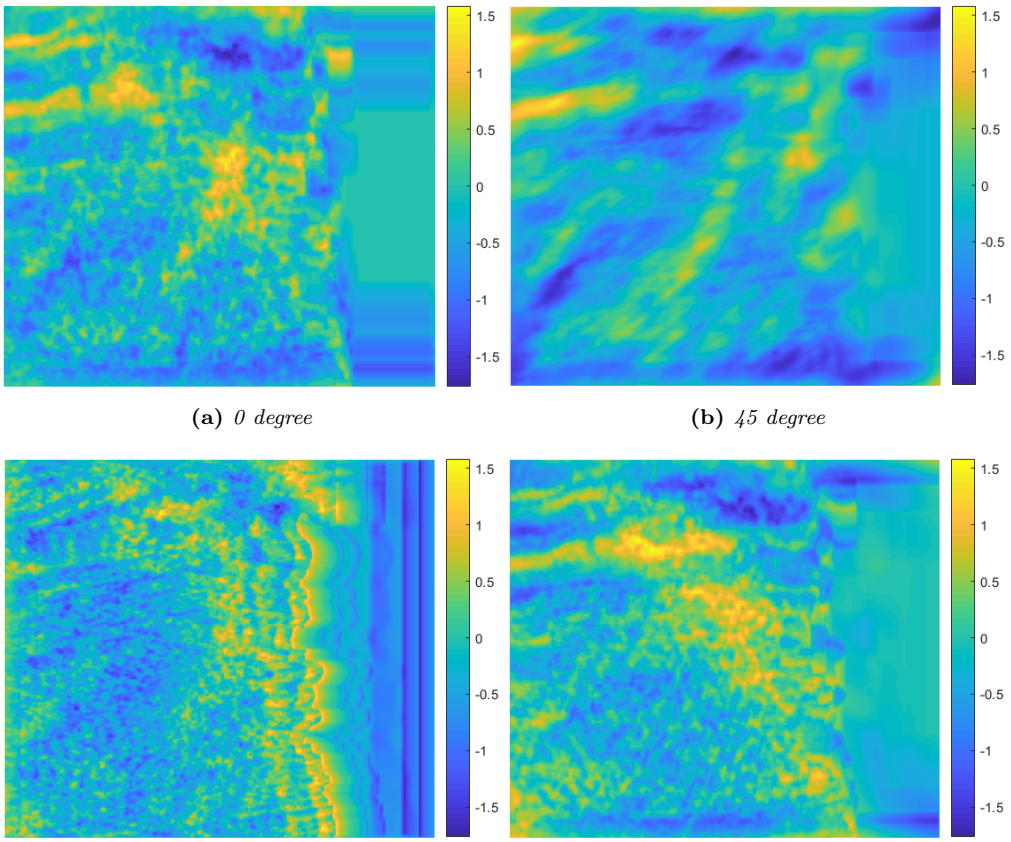


**(a)** *0 degree* **(b)** *45 degree*

**(c)** *90 degree* **(d)** *135 degree*

***Figure 3.7:*** *Four correlation maps of an EUS-frame performed with the templates at four orientations, where the three scales are added beforehand.*

The four correlation maps were further averaged to obtain one assembled correlation map. The correlation information in the assembled correlation map was limited to only contain correlation values higher than a threshold of $\frac{1}{12}$ as this would exclude inverse correlations and low correlation values. An example of an assembled correlation map with the threshold applied is illustrated in Figure 3.8(b).

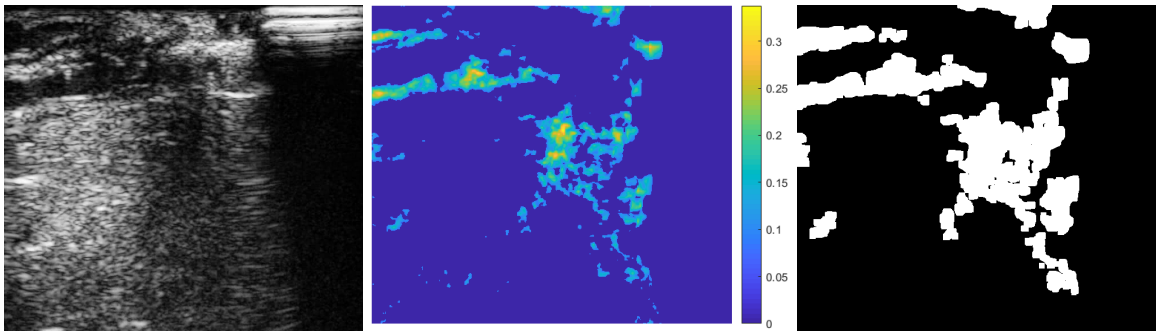


**(a)** *Original EUS-frame* **(b)** *Correlation map of an EUS-frame* **(c)** *Smoothed and binarized correlation map*

***Figure 3.8:*** *An EUS-frame with the assembled correlation map from correlation calculation between the templates and the EUS-frame, and the resulting binarized image, where objects with areas smaller than 1,000 pixels were excluded.*

The assembled correlation map was further filtered with a 2D Gaussian smoothing kernel with a standard deviation of 2, to fill in any minor holes and smooth the boundary to better mimic the true anastomosis vessels. Afterwards, the images were binarized using otsu threshold, and objects with an area smaller than 1,000 pixels were excluded, as shown in Figure 3.8(c). These small areas were excluded given that it was desired to obtain a rough contour of the larger object in the frame, and the small areas were not considered a substantial part of the anastomosis vessels. A threshold of 1,000 pixels was determined based on the analysis of the EUS-frames in section 3.2, where it was observed that the areas of anastomosis vessels consisted of at least 19,600 pixels, thus 1,000 pixels was enough to exclude small areas without excluding areas belonging to anastomosis vessels.
Furthermore, objects with a mean intensity lower than 10 were excluded as this was likely to be related to shadows or missing acoustic contact.

## Merging of vessel candidates

The remaining vessel candidates were labeled and examined to determine whether multiple candidates represented the same object, as shown in Figure 3.9(b), where the three objects outlined in the upper left corner all represented the anastomosis vessels but appeared separated.

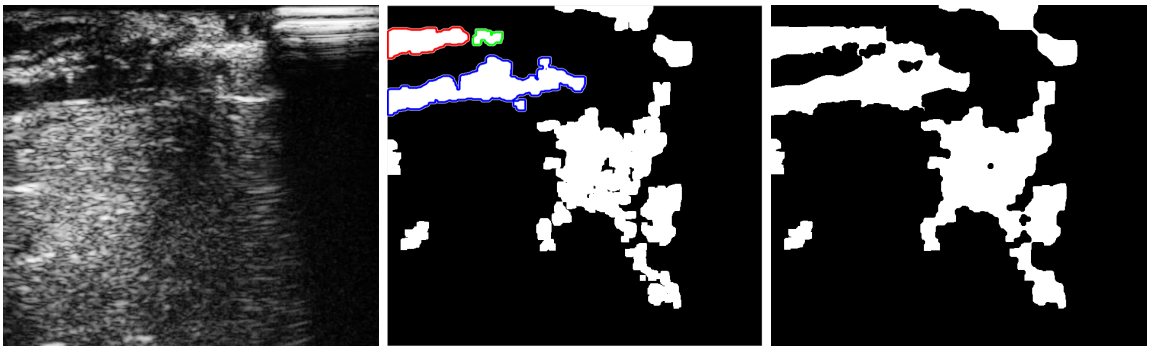

**(a)** *Original EUS-frame* **(b)** *Binarized EUS-frame* **(c)** *Merged vessel candidates*

***Figure 3.9:*** *The three vessel candidates, that are outlined with red, green, and blue, all represent objects belonging to the anastomosis vessels despite not being connected. A distance and intensity measure determine that they should be considered as one object, thus they are labeled identically in order to be identified as one vessel candidate. Subsequently, the vessel candidates labeled identically are merged to represent one vessel candidate.*

To determine whether multiple vessel candidates represented the same object, the distance between the centroid of the candidates was measured. If a distance between two candidates was less than

200 pixels and had minimum a 95 % agreement in their mean intensities, they were labeled the same. In Figure 3.9(b) the distance between the red marked and the blue marked vessel candidate was 130 pixels with a mean intensity difference of 2.18 %, and the distance between the red and green marked vessel candidate was 109 pixels with a mean intensity difference of 1.38 %. Thus, the criteria for representing the same object were satisfied, to which the three candidates were labeled identically and thereby considered as one object.
A limitation of this method was that the distance between vessel candidates was calculated based on the centroid of the candidates, to which a long object could have a long distance to the neighboring object despite their boundaries being very close. In order to accommodate this, a merging operation was implemented, where each vessel candidate was dilated with a disk shaped structuring element with a radius of six pixels. If a candidate overlapped with the neighboring candidate, they were considered the same object and were labeled identically. A disk shape with a radius of six pixels would not be big enough to merge the marked objects shown in Figure 3.9(b), to which only close objects would be merged using this operation. Using a larger radius of the disk could result in an undesirable merging of vessel candidates.
Given that the two above mentioned merging methods only assigned labels, and did not actually merge the objects, an iterative morphological closing operation was performed until the objects labeled identically were merged, as shown in Figure 3.9(c).

### Probability based selection of anastomosis vessels

The labeled vessel candidates were assigned a vessel probability with the purpose of detecting the true anastomosis vessels. The probability was calculated based on the features found in the EUS-image analysis in section 3.2, to which the vessel candidate with the highest probability was selected to be the anastomosis vessels.
To select the most likely vessel candidate to represent the anastomosis vessels, a probability for each vessel candidate was calculated. The probability was based on the most influential features in Table 3.1, which were determined through a calculation of the coefficient of variation, which was calculated by dividing the standard deviation with the mean of the properties for the anastomosis vessels in the development set. The normalized distributions for each coefficient of variation for the features; Area, MeanIntensity, MajorAxisLength, EquivDiameter, Extent, Orientation, Deformity, Ratio, WeigthedCenterY and WeigthedCenterX are shown in Figure 3.10.

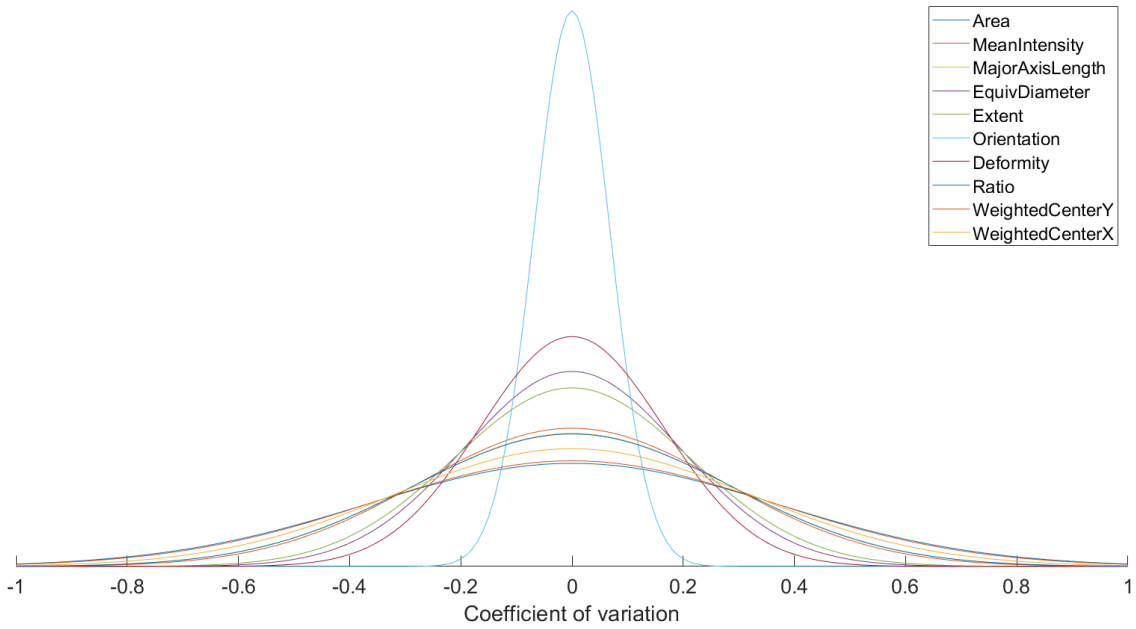


***Figure 3.10:*** *The normalized distributions for each coefficient of variation of the features in Table 3.1.*

As it appears in Figure 3.10 the orientation was the feature with the lowest coefficient of variation, meaning that the orientation of the anastomosis vessels often appeared in the same range in the development frames. Several features were included for the selection of the vessel candidate representing the true anastomosis vessels as a single feature would not be robust to differentiate between vessel candidates. Thus, the three features with the lowest coefficient variation; equivDiameter, extent, and deformity, were included. These features showed a relatively low coefficient of variation compared to the remaining features. Thereby, the four features; orientation, equivDiameter, extent, and deformity were used as features to identify the true anastomosis vessels among the possible vessel candidates.
The probabilities of being the true anastomosis vessels were determined using Mahalanobis distance, which is a statistical distance measure utilizing the mean and standard deviations of multiple features. The Mahalanobis distances were calculated through equation 3.3. [58]

$$md = \sqrt{(y-\mu)\Sigma^{-1}(y-\mu)'} \tag{3.3}$$

Where $md$ is the distance in units of standard deviation from the mean feature vector, $\mu$. $y$ represents the feature vector for the given vessel candidate, and $\Sigma$ is the covariance matrix. [58]
The vessel candidate with the lowest Mahalanobis distance was the vessel candidate with the highest probability of being the true anastomosis vessel, thus it was selected as the estimated vessel. In Figure 3.11(b), two vessel candidates with their corresponding Mahalanobis distance are illustrated.

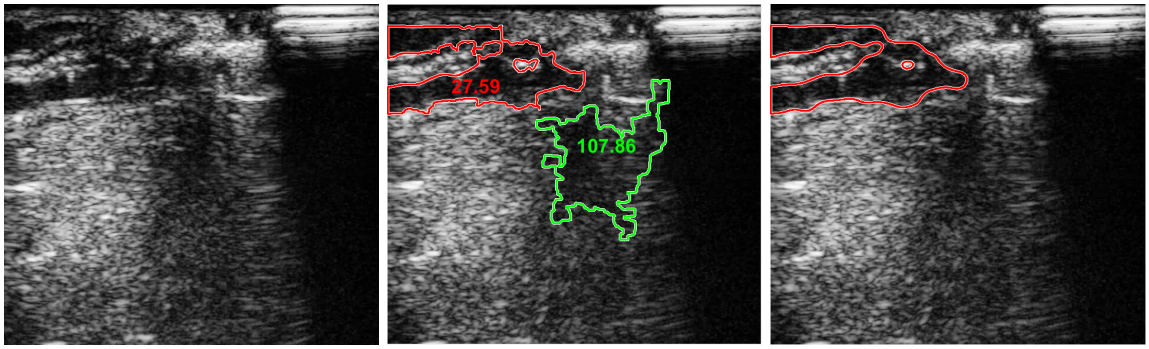


**(a)** *Original EUS-frame*

**(b)** *Mahalanobis distance of vessel candidates*

**(c)** *Final smoothed detected anastomosis vessel*

***Figure 3.11:*** *The vessel candidates with the corresponding Mahalanobis distance, based on the four features; orientation, equivDiameter, extent, and deformity. Lastly, the final detected anastomosis vessels, which was smoothed with a Gaussian filter.*

After identifying and extracting the vessel candidate with the lowest Mahalanobis distance, a filtering of the object was performed with a Gaussian filter with a standard deviation of 10 to obtain a smooth boundary of the object. The final estimated anastomosis vessel is visualized in Figure 3.11(c).
As seen in Figure 3.11(c) a hole in the detection boundary is present. This hole outlines bright intensities, which could refer to a suture error or plaque. Thus, it was retained to guide the segmentation techniques.

## 3.5 Vessel lumen segmentation

The vessel lumen detection, described in section 3.4, provided an initial estimate of the location, size and shape of the anastomosis vessels. However, the detection yielded only a coarse estimate, thus segmentation was performed to obtain a more accurate estimate of the vessel lumen in the EUS-frame. The segmentation was performed using deformable models, which is a widely used technique in medical image segmentation due to its ability to accommodate for prospective variability in anatomical structures. Deformable models are defined as curves or surfaces that deform in an image domain, based on internal and external energies as well as user defined constraints. [59, 60, 61, 62] Furthermore, knowledge about the object of interest, such as shape and appearance, could be considered and included, which potentially could improve the performance of deformable models [60]. By including this, it would be possible to adjust the models to the type of images and requirements for a segmentation, making deformable models interesting when segmenting objects in EUS-frames which contain speckle noise and indistinct or disconnected vessel boundaries.
Two types of deformable models were designed and tested to investigate which model was better suited for accurate estimation of the vessel lumen and sub-optimal patency estimation in the EUS-images; one parametric phase-based and one geometric intensity-based model. The parametric model was designed and implemented as a local-phase based snake, which was guided by local energies in the image domain, where the geometric model was designed and implemented as a Chan-Vese algorithm, which was based on region information.

### 3.5.1 Parametric deformable model

In this project it was chosen to design a parametric deformable segmentation model, to which the local-phase based snake was chosen. This segmentation technique was based on curves defined as a discrete number of control points that were located along the contour of the object obtained in the detection process. The control points were uniformly placed for every 10 pixel along the boundary of the detected vessel lumen, as this was presumed to be appropriate according to the curve's ability to adapt to the shape of the anastomosis boundary.
Displacement of the control points was influenced by internal and external energies and user defined constraints, which determined the deformation of the curve. As opposed to the traditional snake, the local-phase based snake was guided by phase information as an external energy instead of gradient information in the image domain. This possessed advantages when working with EUS-images as these generally consist of relatively poor image quality as they contain speckle noise, low contrast, or low signal-to noise ratio [47]. These characteristics of the image might have directly affected the gradient information of the image and made detection of the true edge challenging during segmentation. By using phase information of the image, a more robust and accurate segmentation might be achieved, as this technique is intensity invariant, meaning that the energies on all edges would be identical independent of their strength in intensity contrast. [47]

In order to determine a curve that estimated the boundary of anastomosis vessels, the internal and external energies had to be minimized, thus the deformation of the curve was regarded as an energy minimizing problem. [59, 63] The total energy that influenced the curve are described in equation 3.4, where the internal energy, $E_{int}$, is weighted by an adjustable parameter, $\alpha$, and the external energy, $E_{ext}$, is likewise weighted by an adjustable parameter $\gamma$.

$$E_{total} = \int_0^1 \alpha E_{int} + \gamma E_{ext} ds \tag{3.4}$$

#### Internal energy in the local-phase based snake

The purpose of internal energy was to preserve the smoothness of the curve by globally minimizing the summation of energies that influenced each individual control point along the curve. The internal energy, $E_{int}$, that influenced the parameterized curve, was expressed by equation 3.5.

$$E_{int}(C) = -\int_0^1 e_{int}(C(s)) ds \tag{3.5}$$

In equation 3.5 the parameterized curve is represented as $C(s) = \{x(s), y(s)\}$ and $e_{int}$ is the internal energies that influence the individual control points locally. In this project two types of internal energies were utilized to deform the parameterized curve, to which these can be defined as in equation 3.6.

$$e_{int}(C(s)) = \alpha \left| \frac{\delta C}{\delta s} \right|_s + \beta \left| \frac{\delta^2 C}{\delta s^2} \right|_s \tag{3.6}$$

The first term, first order derivative between the control points, determined the distance between the control points, and encouraged the curve to shrink, in order to avoid large distances between the points and thereby restrict the shape of the curve. The second term, second order derivative between the control points, controlled the rigidity of the curve, and encouraged the curve to be as smooth as possible to fit the anastomosis vessels, which had a smooth boundary. The parameters $\alpha$ and $\beta$ weighted each term, and could be adjusted according to the segmentation problem. [59, 63] In order to determine these parameters, a parameter search was performed, as described in section 3.6, to investigate which parameters and their combination resulted in the best segmentation estimation of the anastomosis vessels in the EUS-frame.

### External energy in the local-phase based snake

The external energy was derived from the image information, which in this project was defined by phase information of the EUS-image. To utilize the phase information of an EUS-image, a local-phase map was calculated. The frames were initially decomposed into several scales, which was done as vessels of different widths appeared in the frames [64]. The image scaling was achieved similarly to a method used in a study by Ma et al. [47], where a Gaussian pyramid reduction was used to scale frames, in order to detect the lines and edges of different sizes. Gaussian pyramid reduction is an iterative process that decreases the density and resolution of an image to represent pattern information at different scales [65]. The resulting image scales had dimensions that were $\frac{1}{2}$, $\frac{1}{4}$, and $\frac{1}{8}$ of the original image. An example of the Gaussian pyramid reduction of an EUS-frame is shown in Figure 3.12.

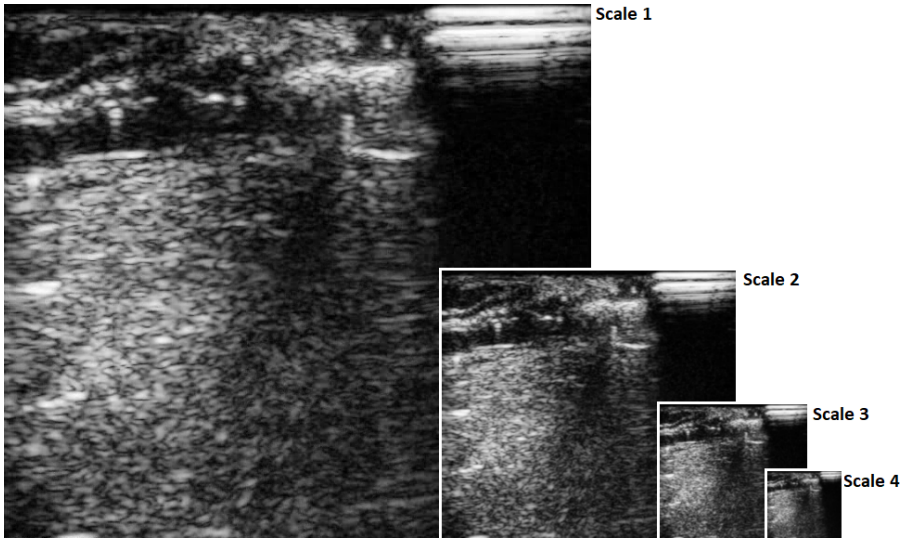


***Figure 3.12:*** *Illustration of four scales of an EUS-image produced using gaussian pyramid reduction.*

A local-phase map was constructed by filtering the frames with 2D gabor filters at each scale. The purpose of using these filters was to combine a line- with an edge-searching filter in the spatial domain [66], in order to detect both constant intensities represented by a line as well as intensity changes over an edge.
A gabor filter consists of a complex pair of filters which is represented as a real and an imaginary part, thus the filter response was a complex value [47, 64]. A gabor filter consisting of a real and an imaginary part with the filter response in the complex plane is shown in Figure 3.13.

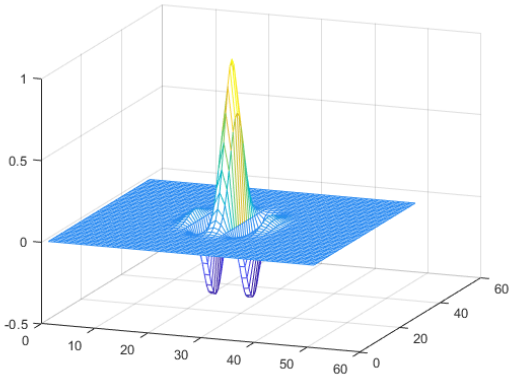


**(a)** *Real part*

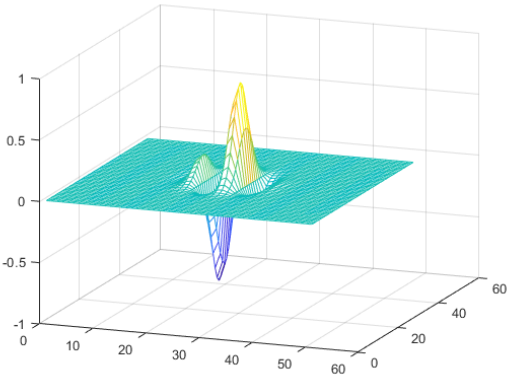


**(b)** *Imaginary part*

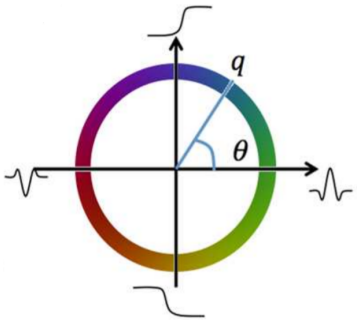


**(c)** *Filter response in the complex plane*

***Figure 3.13:*** *2D gabor filter pair consisting of a real- and imaginary part and the corresponding filter response in the complex plane. [66]*

The real part is the line-searching filter, where the imaginary part is the edge-searching filter [64]. The real part of the filter, as shown in Figure 3.13(a), was designed to detect constant intensities in a line. Contrary, the imaginary filter, as shown in Figure 3.13(c), was designed to respond on sharp intensity changes, which correspond to an edge.
The gabor filters were designed with a wavelength and spatial frequency bandwidth which determined the appearance of the filters. These parameters were tested in a structured parameter search, as described in section 3.6, to investigate which parameter values provided the most accurate segmentation of the vessel lumen.
Given that the lines and edges appeared at different orientations in the EUS-frames, several gabor filters at different orientations were designed. The filters were orientated with an angle of 0, 45, 90 and 135 degrees to the four different image scales. The four angles were chosen, as initial testing showed that four equally spaced orientations were preferable, as it was possible to detect most edge structures in EUS-image.
All of the filter responses at each image scale were subsequently summed into a single response to combine all orientations for each scale. However, a simple summation of the orientations would cause a cancellation effect in the filter response as a result of the different filter orientations. An example is that the filter response that will be produced from white to black intensities in an image may be 90 degrees and if an opposite filter passes, it will be negative 90 degrees. When the two responses are added this will result in 0 degrees, canceling the response. An illustration of this effect can be seen in Figure 3.14.

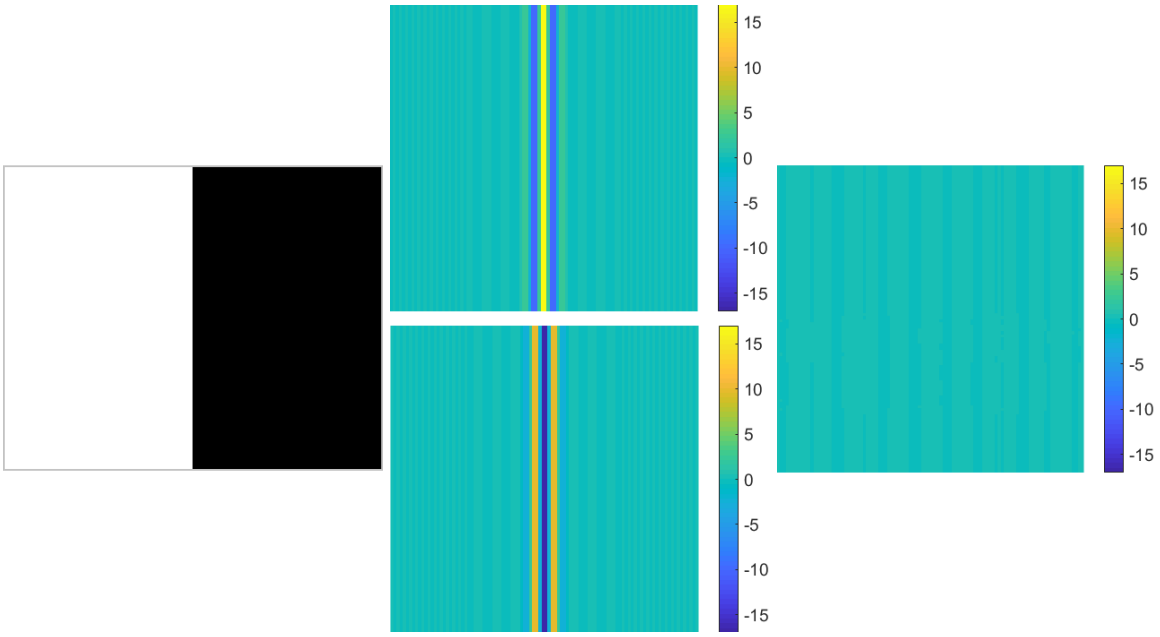


**(a)** *Binary image* **(b)** *Filter response at orientation 0 (top) and 180 (bottom) degrees* **(c)** *Added filter response*

***Figure 3.14:*** *Illustration of cancellation effect where a vertical edge in a binary image is passed by a filter with 0 degree and 180 degree orientation. Lastly, the added response of the two orientations, where the responses are canceled out, is illustrated.*

To avoid the cancellation effect, the phase of all the filter responses was flipped along the real axis as proposed by Lathen et al. [64], and then added together at each scale. This was done by taking the absolute value to the imaginary part of the filter response.

To generate a global phase map, the phase information at the different scales with the summed orientations further had to be combined. Before calculating the combined filter response between the scales, they were composed back to their original image size $574 \times 632$ pixels. This was achieved through equation 3.7.

$$p(u) = \frac{\sum_{l=1}^{N} |p_l(u)|^{\gamma} p_l(u)}{\sum_{l=1}^{N} |p_l(u)|^{\gamma}} \tag{3.7}$$

This equation was used by Lathen et al. [64] and favours high strength responses from the filter at the different scales. In the equation $p(u)$ was the combined filter responses for all scales, where $p_l(u)$ represented the filter responses from each individual scale, $l$. $N$ represented the number of scales, and $\gamma$ was a parameter that weighted the filter responses. [64]
The phase map further had to be normalized, in order to be used to guide the snake. A known way to accomplish this, was to calculate the asymmetry measure of the filter response. This produced a feature map where edges had values near 1 and homogeneous regions had values near 0. The feature asymmetry map is given by equation 3.8.

$$FA = \frac{|Im(p(u))| - |Re(p(u))| - T}{\sqrt{|Im(p(u))|^2 + |Re(p(u))|^2} + \epsilon} \tag{3.8}$$

In equation, 3.8 $Im(p(u))$ represented the imaginary part of the combined filter response $p(u)$, and $Re(p(u))$ represented the real part. $\epsilon$ was a small constant used to avoid cases of zero division, and $T$ was a noise threshold parameter, that was a constant value of 0.1. [47] An example of a feature asymmetry map constructed from an EUS-frame is visualized in Figure 3.15.

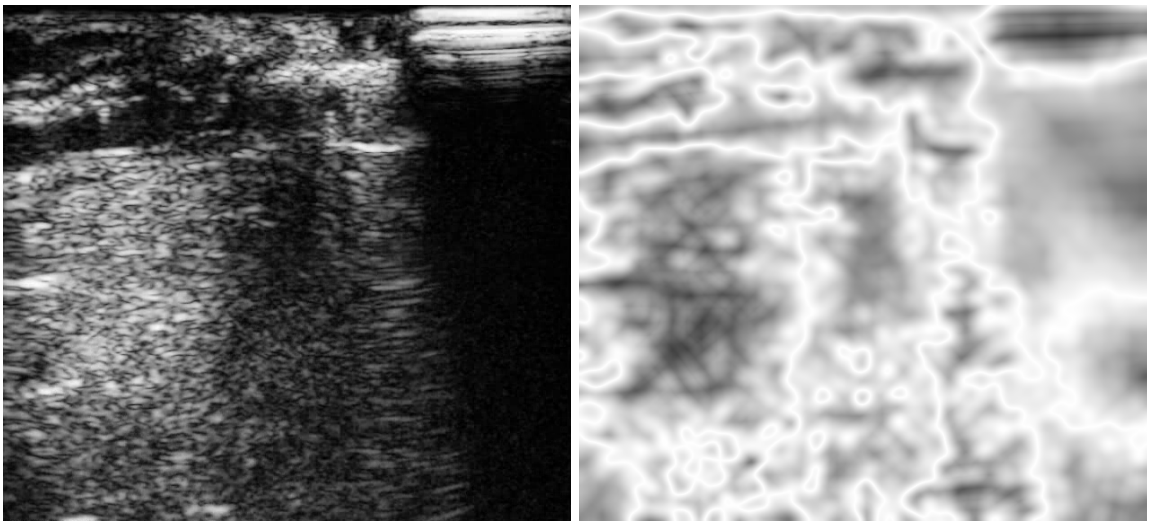

**(a)** *Original EUS-frame* **(b)** *Phase map of the EUS-frame*

***Figure 3.15:*** *An original EUS-frame with the corresponding feature asymmetry map.*

Figure 3.15(b) comprised the external energy, to which the boundary of the detected vessel lumen was guided by the information in the given phase map. When the energy was minimized or a maximum number of iterations was reached, the deformation of the curve stopped and the final segmentation was determined.

### 3.5.2 Geometric deformable model

In this project, the Chan-Vese algorithm was used as an alternative approach for segmenting the anastomosis vessels to which the vessel lumen detection was used as an initial curve. The Chan-Vese algorithm is a geometric deformable model, which is based on the level-set method, where an evolving curve is represented by an implicit level-set function. The curve is evolved by utilizing internal and external energies, where the internal energy can be derived from curve information, and the external energies can be derived from either local edge information and/or global region information. A limitation with only using local edge information is that the model may be more sensitive to noise, where a region based model may be more robust, which was assumed preferable when working with EUS-images, as these contained noise in terms of speckle, as mentioned in section 3.2. Furthermore, the initial curve, derived from the detected object, could not be guaranteed to be close to the vessel lumen boundary. Thus, a local-edge based segmentation might not be able to find the true edges as the curve might stop too early at a local minimum, to which the Chan-Vese algorithm may be preferable [60, 67].
The level-set function, which represented the contour as a distance map, was zero at the curve, known as the zero level-set, and was then either positive or negative outside and inside the curve. The concept of curve evolution is illustrated in Figure 3.16, where the curve is represented as the contour of a plane. The function evolved under the influence of internal and external energies. [60, 67] As the level-set function, $\phi(x, t)$, evolved, the topology of the implicit curve may change.

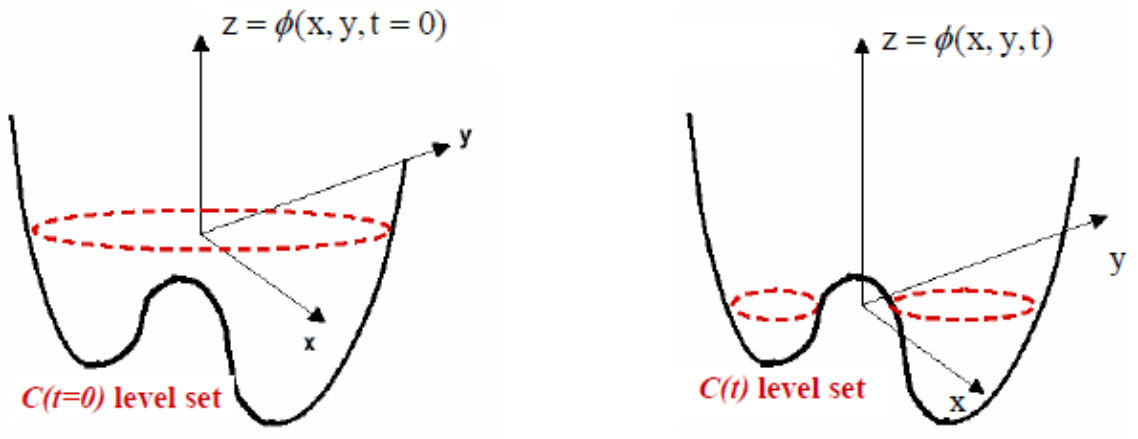


***Figure 3.16:*** *Curve evolution based on the level-set method. The contour, C, is represented by the red dotted line, where it is illustrated that the level-set method is able to adapt to topological changes during curve evolution. [68]*

The Chan-Vese algorithm is derived from the Mumford-Shah functional, which is implemented into a level-set framework. The Mumford-Shah functional segments an image into regions with homogeneous intensities. In a simplified Chan-Vese algorithm, the segmentation was based on a bimodal case, where the EUS-frame was divided into object and background; an object inside and outside the curve. A simplified equation of the Chan-Vese algorithm with the energies utilized in this project is shown in equation 3.9. [69, 70]

$$F(c_1, c_2, C) = \lambda_1 \int_{inside(C)} |I_0 - c_1|^2 dxdy + \lambda_2 \int_{outside(C)} |I_0 - c_2|^2 dxdy + \mu Length(C) \tag{3.9}$$

Where $I_0$ was the original EUS-image in the image domain $\Omega$, $c_1$ and $c_2$ represented the mean intensities inside and outside the curve, denoted $C$. The first and second terms in the equation was the data terms, which penalized the difference between the original EUS-image and the estimated model. The third term was the regularization term, which penalized the length of the curve. By including this regulation term it was possible to regulate the behavior of the curve evolution, and ensured that the intensity information in the image was not the only feature determining the curve evolution. This was relevant to include since the EUS-images contained unclear and indistinct edges due to the speckle noise and artifacts.
$\lambda_1$, $\lambda_2$, and $\mu$ were adjustable parameters that weighted the three terms. These were tested in a structured parameter search in section 3.6, in order to obtain the most accurate segmentation of the vessel lumen. By changing $\lambda_1$ and $\lambda_2$, the external energy was varied, and by increasing these parameters, the intensity information in the image was weighted higher. The parameter $\mu$ adjusted the length of the curve, where a high value resulted in a smoother curve, and a small value resulted in a more accurately fitted curve.
When transforming the Mumford-Shah functional to a level-set framework, the curve was represented by the zero level-set of the level-set function, $\phi$. In order to transform the functional to a level-set framework, the Heaviside function, $H(\phi)$, and the Dirac Delta function, $\delta(x)$, were utilized, as shown in equation 3.10. [60, 67, 69]

$$F(c_1, c_2, \phi) = \lambda_1 \int_\Omega (I_0 - c_1)^2 H(\phi) dxdy + \lambda_2 \int_\Omega (I_0.c_2)^2 (1 - H(\phi)) dxdy + \mu \int_\Omega \delta(\phi) |\nabla \phi| dxdy \tag{3.10}$$

Where the Heaviside function is approximately either one or zero depending on whether the level-set function is positive or negative, as seen in the following formula.

$$H(\phi) = \begin{cases} 1 & \phi > 0 \\ 0 & else \end{cases} \tag{3.11}$$

The Dirac Delta function was used in the length term, since it excluded everything except the boundary, as it was one at the boundary and zero everywhere else, as shown in the following formula. [67]

$$\delta(\vec{x}) = \begin{cases} 1 & \vec{x} = 0 \\ 0 & else \end{cases} \tag{3.12}$$

With the purpose of finding the best contour estimation of the anastomosis vessel boundaries, the energy, $F$, should be minimized with respect to $\phi$ to which Euler-Lagrange equations were utilized. [60, 67, 69] In order to minimize the energy, the Euler-Lagrange equation should approach zero, to which gradient descent was utilized. The level-set function adjusted the implicit curve iteratively and continued to deform until a stopping criterion was reached. The segmentation process would stop if the contour was unchanged during five consecutive iterations or if a specified maximum number of iterations was reached. A maximum number of iterations was a necessary stop criterion, due to the presence of speckle, shadows and structures around the anastomosis vessels appeared with similar intensities. This could result in the contour leaking beyond the vessel boundaries and include additional structures as shadows. To achieve the most optimal value for the maximum number of iterations, several values were tested in a parameter search.

## 3.6 Parameter search

The two segmentation methods; local-phase based snake and Chan-Vese were tested in a structured parameter search to determine which parameter and combinations would produce the most accurate estimated segmentation of the anastomosis vessel. The specific parameters and ranges are described and separated into two sections; local-phase based snake and Chan-Vese.
The parameter searches were performed on the selected development set, consisting of EUS-frames from seven patients. The two segmentation techniques were both initialized with an initial curve obtained from the vessel lumen detection.
To examine the performance of the segmentation techniques with the different parameters and combinations, a Dice similarity coefficient was calculated between the automatically segmented vessel lumen and the belonging manual expert anastomosis annotation. The Dice coefficient is a measurement for how similar two images are, where the output value is between 0 and 1, where 0 represents no similarity and 1 represents a perfect match of the two images. The Dice similarity measure was calculated using equation 3.13.

$$Dice(A, B) = \frac{2 \cdot TP}{2 \cdot TP + FP + FN} \tag{3.13}$$

The Dice coefficient was dependent on the amount of true positive ($TP$), false positive ($FP$), and false negative ($FN$) pixels that were in the automatically segmented image when compared to the manual annotations.
The optimal parameter combination for both segmentation techniques was selected through an analysis of the mean Dice coefficients and standard deviations calculated from all EUS-frames. To avoid disturbing the result of the parameter search, detections with a Dice coefficients of 0 were excluded. The Dice coefficients were plotted to get an insight into the variation of the Dice coefficients between the several parameter combinations. The parameter combination was assumed the most suitable in the segmentation of EUS-frames when a high mean of the Dice coefficients and a low standard deviation were obtained.

### Local-phase based snake

The optimal performance of the local phase-based snake segmentation was found by testing parameters for both the generation of the phase map and the behavior of the snake. The parameters associated with the phase map were related to the characteristics of the gabor filter, where wavelengths in the interval $20 - 28$ were tested for every 4th value, along with a spatial frequency bandwidth for every 0.2 value in the interval $1 - 1.4$.

The tested snake parameters were the weights of the two internal energies and external energies, all within the interval $0.25 - 0.75$ with intervals of 0.25. Furthermore, a parameter search on the maximum number of iterations was performed in the interval $30 - 50$ for every 10th value.

### Chan-Vese

In the parameter search for the Chan-Vese segmentation the weights for the internal and external energies were tested. The external energies, $\lambda_1$ and $\lambda_2$, were tested with weights in the interval $0.3 - 0.9$ for every 0.3th value, and the weight for the internal energy $\mu$, which determined the smoothness of the curve, was tested in the interval $1.5 - 3$ for every 0.5th value. Furthermore, the number of maximum iterations was tested for every 50th value in the interval $100 - 200$.

## 3.7 Patency estimation

The patency estimation was implemented to identify and highlight possible sub-optimal patencies in the vessel lumen. The intention was to provide decision support in terms of an objective assessment of the anastomoses during CABG-procedure and indicate whether a revision was to be considered. In order to determine the patency of the segmented vessels, the cross sectional diameter throughout the vessels was to be calculated. To accommodate the variations of orientation and shape of the anastomoses, a centerline along the coronary artery and graft was constructed. The purpose of the line was to measure the diameter orthogonal to the centerline which followed the vessel course. The centerline was constructed by using continuous morphological erosion, only allowing the object to maintain a width of one pixel, and thus constituting the skeleton of the anastomosis, as shown by the example in Figure 3.17(a).

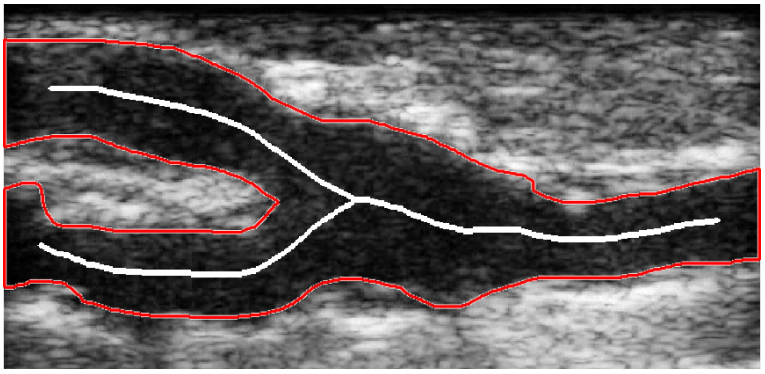

**(a)** *Centerline for the segmented vessels*

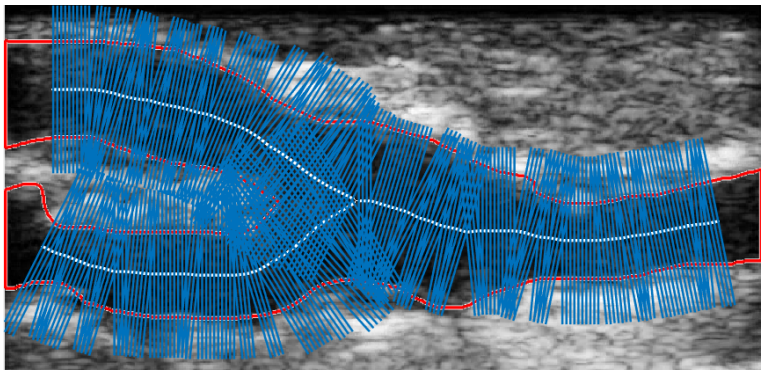

**(b)** *Orthogonal scanlines defined along the path of the centerline*

***Figure 3.17:*** *EUS-frame where the red boundary represents the boundary of the vessel lumen, and the white line within the boundary is its centerline. The blue lines are orthogonal scan lines which were used to determine the diameters of the vessels.*

As the data was sorted to contain only end-to-side anastomoses, the centerline was ideally made up of one branch point near the merge point between the graft and the coronary artery, and three endpoints; two at each end of the coronary artery and one at the end of the graft. Equivalently, this notation along with the fact that the graft was located above the coronary artery, made it possible to automatically identify which of the three lines originating from the branch point belonged to either the graft or coronary artery. In cases where just one vessel was detected or extra branches were segmented it was not possible to divide the vessels into graft and coronary artery, as there would be no specific landmarks or characteristics identifying each vessel.
To better determine the patency, the centerline was decomposed into linear segments, by selecting every 10 points along the centerline and constructing a linear line between the points. From these lines, angles were calculated to which orthogonally placed scanlines measured the diameter of the vessel. The scan lines had a fixed length covering 200 pixels, which were determined based on observations of vessel lumen diameters in the development set. In Figure 3.17(b) an EUS-frame with vessel boundaries, corresponding centerline, and the orthogonal scan lines are visualized.
Using the scan lines the diameter was determined by a distance measure between the two nearest edge points of the segmented vessels in each individual scan line. This prevented the scan lines that covered both the graft and coronary artery to be included in the distance measure. Additionally, scan lines which only covered one edge point were excluded from the distance measure. The distance was measured as the euclidean distance between the two intersection points between the scan line and the boundary of the segmentation. This was calculated using equation 3.14.

$$d_s = \sqrt{(x_1 - x_2)^2 + (y_1 - y_2)^2} \tag{3.14}$$

In equation 3.14 $d_s$ refers to the distance between the two points $(x_1, y_1)$ and $(x_2, y_2)$, representing the diameter of vessel lumen for the given scan line.
Sub-optimal patency was determined on the same criteria as the FitzGibbon grading, where sub-optimal patency is presumed if the stenotic rate is greater than 50 % of the maximum vessel diameter, as first mentioned in Table 2.1. Sub-optimal patency was determined if:

$$50 > \frac{d_s}{d_{ref}} * 100 \tag{3.15}$$

Here $d_s$ is the distance determined for a single scan line and $d_{ref}$ was the reference diameter. As errors and irregularities in the vessel boundaries could occur in the segmentation, the reference diameter was chosen to be more general, as the maximum vessel diameter could be a sensitive measure. Thus, the reference diameter was calculated through equation 3.16.

$$d_{ref} = mean(d > mean(d)) \tag{3.16}$$

Where $d$ represented all cross sectional diameters measured in the given vessel. The distance measure could be performed separately on the graft and coronary artery in segmentations with the characteristic "y"-shape, as it was possible to identify which scan lines belonged to the graft and coronary artery. This was beneficial as the internal diameter of the graft and coronary artery was observed to vary considerably in some cases. In segmentations that represented one vessel or multiple extra branches, e.g. segmented shadowing, the reference diameter would be determined by the equation using all cross sectional diameters in the vessels. In cases of sub-optimal patencies in the anastomosis vessels the area was highlighted in the EUS-frame.

## 3.8 Validation

The automatic quality assessment model was tested and validated in three parts; vessel lumen detection, vessel lumen segmentation, and patency estimation. The three parts were tested individually, despite being dependent on the preceding part.
Manual expert annotations of the anastomoses were available for all EUS-frames in the development- and test set, thus a comparison between the output of the model and a "ground truth" was possible. This was done for both the development set, consisting of 96 EUS-frames from seven patients, and the test set, consisting of 271 EUS-frames from 24 patients.

### 3.8.1 Vessel lumen detection

The vessel lumen detection was aimed to estimate an approximate location, shape, and size of the anastomosis vessels. The output images from the detection algorithm contained a rough estimation of the anastomosis vessels, which were validated through the use of Dice similarity measure between the manual expert annotations and the detected vessel boundary. As the detection was meant to produce a rough appearance of the of the anastomosis vessels, it was determined that a Dice coefficient of 0.5 or above would be sufficient when compared with the manual annotations, and would thereby count as an accepted detection of the anastomosis vessels. This Dice threshold was selected based on the assumption that a 50 % overlap between an initial boundary of the detected object and the anastomosis vessels would be enough for the segmentation methods to perform an accurate segmentation of the anastomotic structures. To get insight into the performance of vessel lumen detection algorithm, examples of both insufficient and sufficient detection boundaries are visualized. Additionally, possible tendencies will be pointed out. Furthermore, the Mahalanobis distance of the vessel candidates was investigated, to examine possible tendencies and patterns in the Mahalanobis distance in relation to the different vessel candidates.

### 3.8.2 Vessel lumen segmentation

Validation of the vessel lumen segmentation was performed by calculating Dice coefficients between the segmented anastomosis vessels and the manual expert annotation.
To evaluate the robustness of the vessel lumen segmentation independent from the performance of the vessel lumen detection, modified versions of the manual annotations from the corresponding frames in the test set were used as initial contours for the segmentation algorithms. Similarly, performance was evaluated using Dice similarity measure from which an indication of the robustness could be interpreted. Furthermore, examples of the segmentations performed with the modified initial contours will be shown to describe variations in segmentation behavior. The initial contours were created using morphological erosion on the manual annotation where two different variations were tested. The initial contours were constructed using a disk shaped structuring element with a radius of 10 pixels and 20 pixels to represent small and large variations, respectively. The segmentations were performed using the same parameters derived from the parameter search for both segmentation algorithms stated in section 3.6.

### 3.8.3 Patency estimation

The validation of the patency estimation algorithm was performed by applying the same algorithm on the manual anastomosis annotations. This was performed to test the robustness of the algorithm, as the manual annotations would represent the same anastomosis vessels as those identified by the detection and segmentation algorithms, but could vary in vessel appearance. In the case of the algorithm finding sub-optimal patency in either automated segmented vessels or manual annotations, these were divided into their respective locations of the anastomosis vessels; heel site, toe site, or the anastomosis orifice. This was to provide a better indication of agreement in the number of sub-optimal patencies between the automatically segmented vessels and manual annotations. As the purpose of the test was to identify patency of the anastomosis orifice, heel- and toe site in the vessels, only automatically segmented vessels showing these parts of the vessels were included in this test. Thus, EUS-frames where an insufficient segmentation was performed by the local-phase based snake or the Chan-Vese algorithm were excluded. The test was executed twice; one comparing the

patency in the manual annotations to the patency found in local-phase based snake segmentations, and one where it was compared to the patency found in the Chan-Vese segmentations. Patency in the anastomosis orifice, heel-, and toe site was evaluated for each segmented vessel, to which it was noted whether sub-optimal patency was present or not. Differences between the patencies estimated in the automatically- and the manually segmented vessels were calculated and presented in matrices for each vessel location. In the matrices the agreement and disagreements between the patency estimations of the automatic and manual annotations are stated.
Furthermore, it was possible to get expert observation on four selected EUS-frames from the chief physician of thoracic surgery at Aalborg university hospital. These observations were used as a qualitative analysis of the patency estimation, where observation would indicate whether actual stenosis of the anastomosis vessels was to be considered in the given EUS-frames. The observation stated the presence of stenoses, their rough locations, and whether it was as a result of either plaque or suture error in the anastomosis. The four EUS-frame observations were compared to the result of the patency estimation derived from the vessel detection and segmentation algorithms.

# 4. *Results*

Results of the parameter search, the detection-, segmentation- and patency estimation of the vessel lumen are presented in this chapter. The following will present the performance as well as specific examples showing the weaknesses and strengths of the proposed methods.

## 4.1 Parameter search

The parameter search was performed using EUS-frames from seven patients from the development set, where detections with a Dice coefficient of 0 were excluded, thus the parameter search was performed on 94 EUS-frames. A total of 729 sets of parameters were tested for the local-phase based snake algorithm and 324 sets for the Chan-Vese algorithm, where a Dice coefficient between the segmentations and the manual anastomosis annotations was calculated for each parameter set to evaluate their performance. Results showed that parameters tested for the Chan-Vese algorithm had little influence on the Dice coefficient, compared to the parameters for the local-phase based snake, where the parameters' influence on the performance can be seen in Figure 4.1.

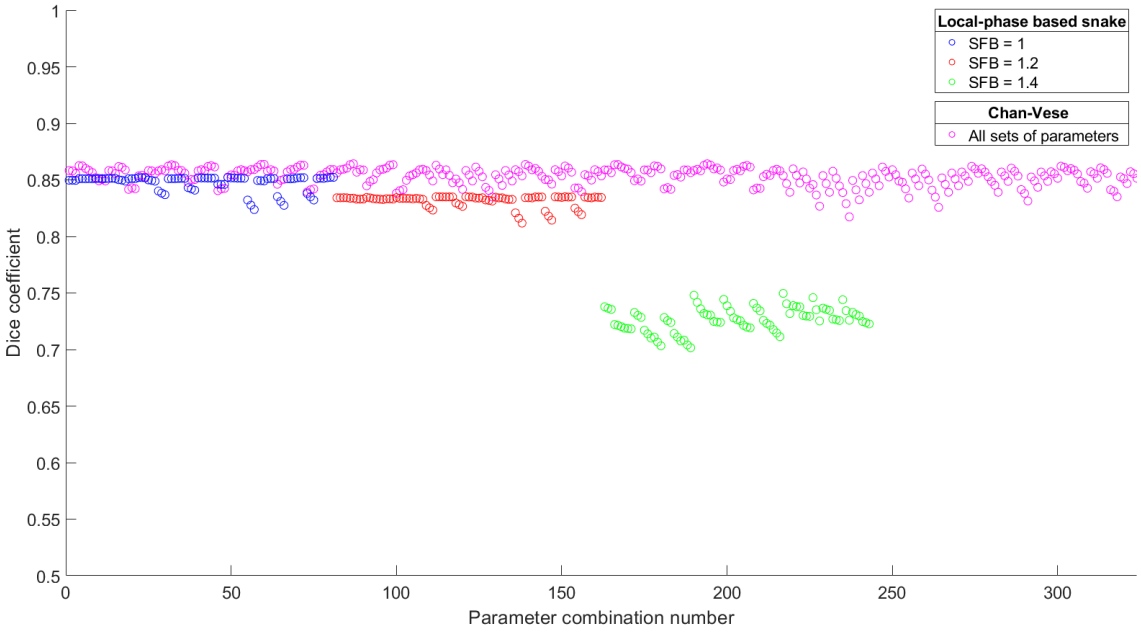


***Figure 4.1:*** *Dice coefficients calculated for the parameter combinations used for the local-phase based snake and Chan-Vese algorithm. The plot of local-phase based snake parameters includes the results for wavelength of 28, illustrating the effect of changing the remaining parameters. Changes in spatial frequency bandwidth (SFB) is indicated with the colors blue, red, and green. The plot of the parameter combinations for the Chan-Vese algorithm is indicated with magenta.*

For the local-phase based snake the plot only shows the variation of the Dice coefficients for the wavelength of 28, as the performance and tendencies of the parameter changes were near identical at a wavelength of 20 and 24. Furthermore, a step-wise variation in the Dice coefficients can be observed, which is as a result of changes to the spatial frequency bandwidth used to produce the

phase map. At a spatial frequency bandwidth of 1 and 1.2 small variations occurred when changing the remaining parameters, where the most significant drops in Dice coefficients were as a result of an external weight parameter of 0.25. At a spatial frequency bandwidth of 1.4, the performance became more unstable. Overall the most influential parameters for the local-phase based snake were the ones that produced or weighted the external energies. The sets of parameters tested for the Chan-Vese segmentation produced only a small variation between the parameters, as shown in Figure 4.1, where an overall mean Dice coefficient of $0.8532 \pm 0.0079$ was calculated. The local-phase based snake segmentation showed a higher variation in Dice coefficients compared to the Chan-Vese, having an overall mean of $0.8049 \pm 0.0492$.
The parameters that resulted in the highest segmentation performance for the local-phase based snake achieved a mean Dice coefficient of 0.8523 with a standard deviation of 0.0818, where the parameter combination for the Chan-Vese algorithm resulted in a Dice coefficient of 0.8642 with a standard deviation of 0.0946 between automatic and manual segmentations. The parameter combinations for both segmentation techniques are listed in Table 4.1.

| Local-phase based snake | | Chan-Vese | |
|---|---|---|---|
| Wavelength | 28 | Initial gaussian filter of EUS-image (SD) | 2 |
| Spectral frequency bandwidth | 1 | Smooth factor $\mu$ | 3 |
| Curve weight $\alpha$ | 0.75 | Foreground weight $\lambda_1$ | 0.3 |
| Continuity weight $\beta$ | 0.75 | Background weight $\lambda_2$ | 0.6 |
| External weight $\gamma$ | 0.75 | Maximum number of iterations | 150 |
| Maximum number of iterations | 50 | | |

***Table 4.1:*** *Parameters that resulted in the highest performance in the local-phase based snake and Chan-Vese algorithm.*

## 4.2 Vessel lumen detection

The performance of the vessel lumen detection was evaluated based on the Dice coefficients between the detected vessels and the manual anastomosis annotations, to which the mean performance in Dice coefficients and the standard deviation are shown in Table 4.2.

| Data set | Mean Dice and SD of all frames | Number of frames with Dice $\geq 0.5$ | Number of frames with 0 <Dice <0.5 | Number of false positives |
|---|---|---|---|---|
| Development set | 0.8149 ($\pm$0.1423) | 93 (96.88 %) | 1 (1.04 %) | 2 (2.08 %) |
| Test set | 0.7412 ($\pm$0.2230) | 247 (91.15 %) | 7 (2.58 %) | 17 (6.27 %) |

***Table 4.2:*** *Mean and standard deviation (SD) of the Dice coefficients between the vessel detection and manual anastomosis annotations for the EUS-frames in the development and test set. Followed by the number of vessel detections which were considered sufficient (Dice $\geq$ 0.5), sub-optimal detections (0 < Dice < 0.5), and false positive detections (Dice = 0).*

In Table 4.2, 96.88% and 91.15% frames from the development and test set, respectively, were considered sufficiently detected. Furthermore, 3.12% and 8.85% had a Dice coefficient lower than 0.5 in the development and test set, to which these were considered insufficient. Comparing the performance of the detection on EUS-frames from development and test set, a drop in the mean Dice coefficient of 0.0737 was observed. This was partly because 17 anastomosis vessels were false positively detected in the test set, compared to two anastomosis vessels in the development set.
An illustration of the distribution of the Dice coefficients for each individual frame and patient for both development and test set are visualized in Figure 4.2 and 4.3. In the figures, the frames from the same patient are visualized with the same color, and the horizontal line in each plot indicates the chosen threshold of 0.5 that determined whether the detection of anastomosis vessels was considered sufficient or insufficient.

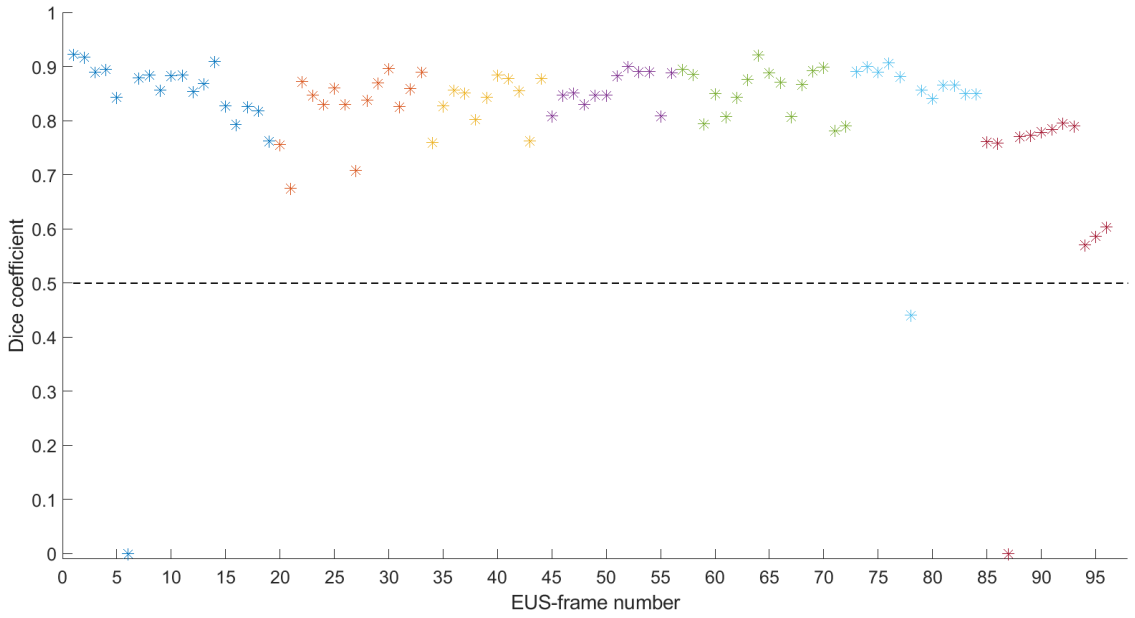


***Figure 4.2:*** *Dice coefficients between the detected vessel lumen and manual anastomosis annotations for each EUS-frame in the development set. Frames from the same patient are marked with the same color.*

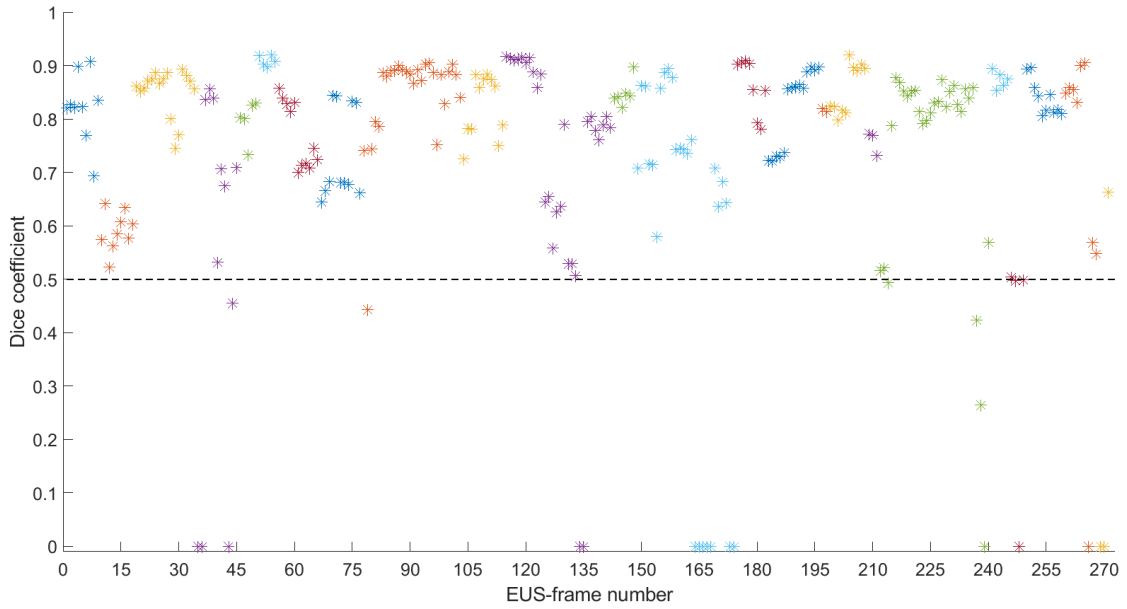


***Figure 4.3:*** *Dice coefficients between the detected vessel lumen and manual anastomosis annotations for each EUS-frame in the test set. Frames from the same patient are marked with the same color.*

In the figures, the most frames were detected with a Dice coefficient between 0.7-0.9 in both the development and test set. However, the Dice coefficients calculated from the test set were more widely distributed. An observation to be noted from the false positive detections in the test set, from Figure 4.3, is that more consecutive frames were often false positively detected.
In Figure 4.2 it is evident that the patient with the EUS-frames number $85-96$ had Dice coefficients that were separated into two clusters. EUS-frames $85-93$ had a Dice coefficient in the interval $0.75-0.80$ with the exception of one false positively detection, and EUS-frames $94-96$ had a Dice

coefficient in the interval $0.57 - 0.61$. Initially, these differences in Dice coefficients were thought to be as a result of several anastomoses from the same patient, but as shown in Figure 4.4, the EUS-frames visualized the same anastomosis vessels, but were from two different EUS-sequences. In Figure 4.4(a) and 4.4(b) the identified vessel candidates with the corresponding Mahalanobis distance are outlined with magenta, the detected vessels are marked with a cyan boundary, and the manually annotated anastomosis vessels are marked with a yellow boundary.

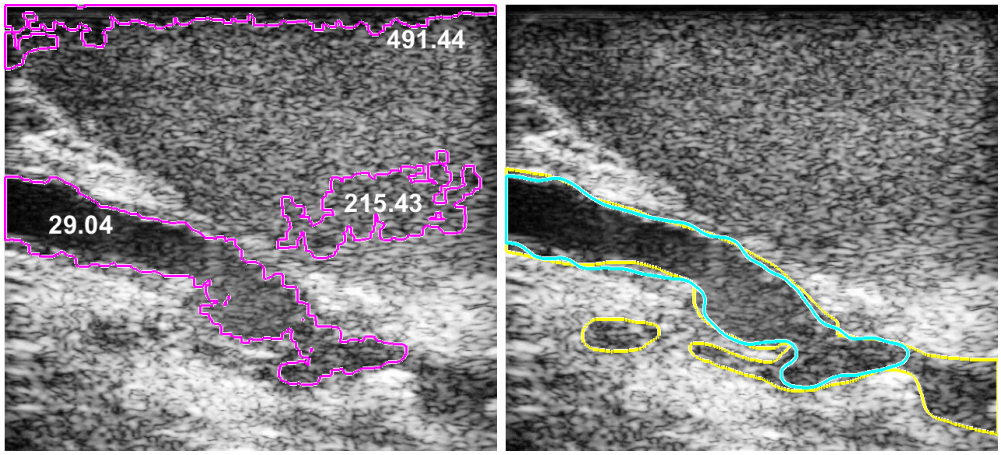


**(a)** *EUS-frame 92 with the vessel candidates and their corresponding Mahalanobis distance, and the detected vessel with a Dice coefficient of 0.7961*

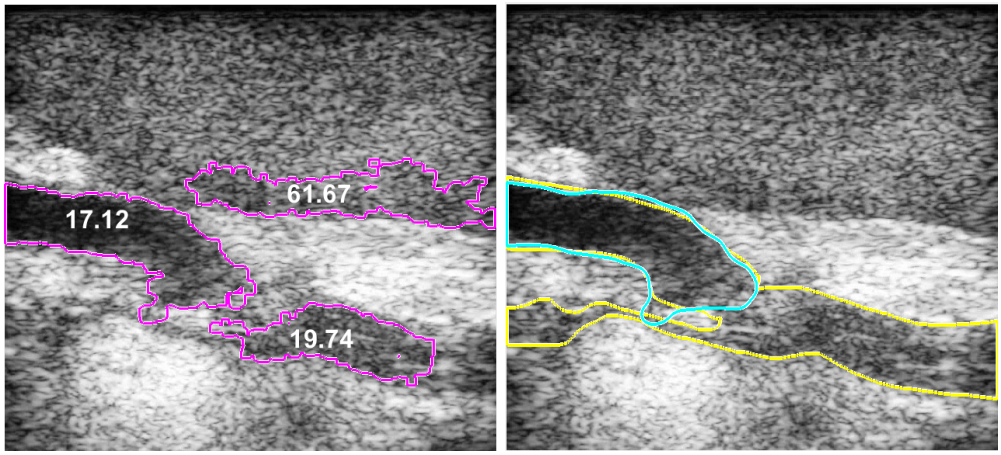


**(b)** *EUS-frame 94 with the vessel candidates and their corresponding Mahalanobis distance, and the detected vessel with a Dice coefficient of 0.5705*

***Figure 4.4:*** *Two EUS-frames from the same patient visualizing the same anastomosis. The vessel candidates, outlined magenta, with the corresponding Mahalanobis distance are shown, along with the final detected vessel, outlined cyan, and the manually annotated anastomosis, outlined yellow.*

In Figure 4.4 it is seen that more of the true vessel in Figure 4.4(a) was detected compared to the detection in Figure 4.4(b). However, a vessel candidate representing the coronary artery was identified in Figure 4.4(b), but the candidates representing the graft and coronary artery were not merged due to the variation in the mean intensities of the objects. This resulted in a lower Dice coefficient for the detection in Figure 4.4(b), due to only the graft of the anastomosis vessels was detected.
Another observation from Figure 4.2 and Figure 4.3 is that despite the false positively detected anastomosis vessels, not all frames from one single patient were detected with a Dice of 0. However, frame number 246, 247, and 249 from the same patient in the test set showed Dice coefficients between $0.48 - 0.51$, where only one frame had a Dice coefficient above the detection threshold. The vessel candidates and the detection having a Dice coefficient of 0.49, are visualized in Figure 4.5. Furthermore, the vessel detection in frame number 239 was observed to have a low Dice coefficient

of 0.27, labeling it as an insufficient detection. The vessel candidates and the detection from frame number 239 are visualized in Figure 4.5.

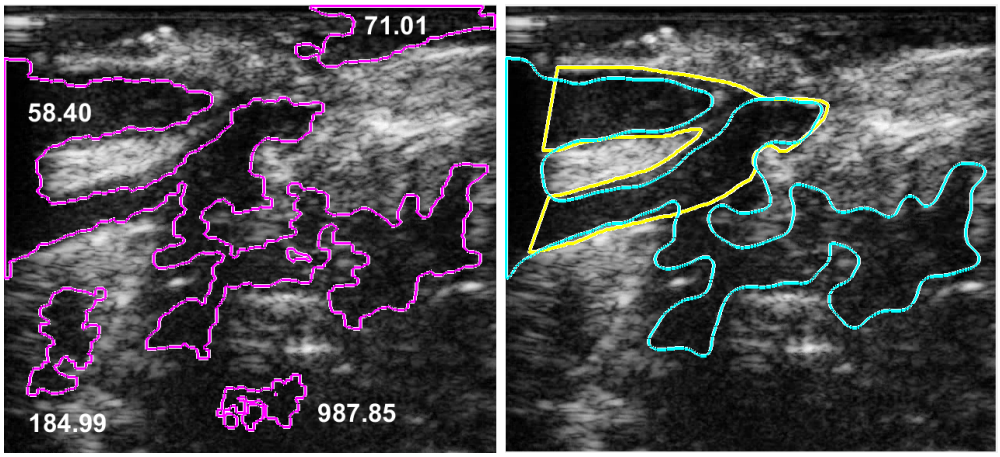


**(a)** *EUS-frame 249 with the vessel candidates and their corresponding Mahalanobis distance, and the detected vessel with a Dice coefficient of 0.4988*

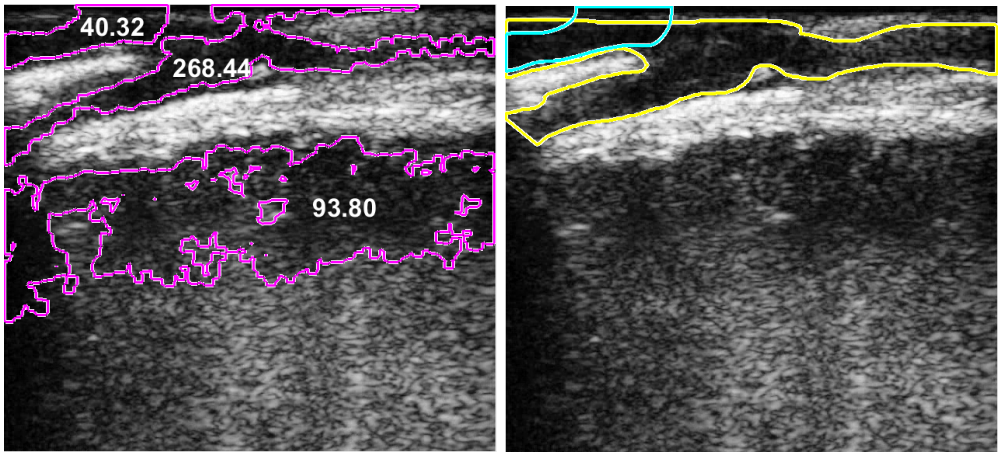


**(b)** *EUS-frame 238 with the vessel candidates and their corresponding Mahalanobis distance, and the detected vessel with a Dice coefficient of 0.2649*

***Figure 4.5:*** *Detected vessels with a Dice coefficient lower than the threshold of 0.5. The magenta boundaries represent the vessel candidates, and the yellow boundary represents the manual anastomosis annotation and the cyan boundary represents the detected object.*

In Figure 4.5(a), the detected object overestimated the actual vessel boundaries, and leaks into non-acoustic contact and surrounding tissue consisting of low intensities. However, the detection captures almost all of the actual anastomosis vessels. In Figure 4.5(b), the detection captures only a part of the graft, despite the coronary artery being identified as a vessel candidate. Ideally, these vessels should have been merged, but the mean intensities of the two objects varied with more than 5 %.

The detection algorithm was initiated with an entropy analysis with the purpose of identifying and excluding non-acoustic contact present in the EUS-frames. However, results showed that the entropy filtering operation did not always exclude the areas as intended. This is for instance shown in Figure 4.5(a), where the non-acoustic contact was included as a part of the detected object. From the results of the entropy filtering operation, three cases kept reoccurring, to which three examples showing these are illustrated in Figure 4.6.

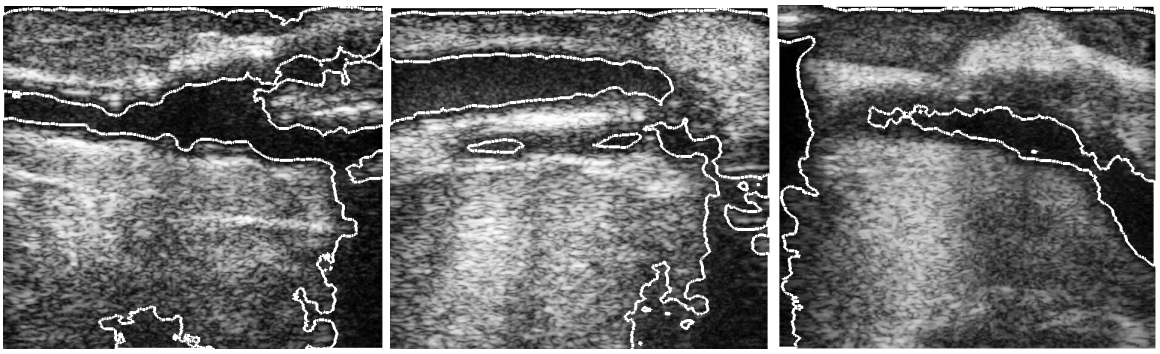

**(a)** *Case A* **(b)** *Case B* **(c)** *Case C*

***Figure 4.6:*** *Three results of the entropy filtering. Case A illustrates the entropy filtering where shadows and the anastomosis vessel are one coherent object. Case B identified the shadows in the right corner, however it was connected to the toe of the anastomosis vessels. Lastly, case C shows an example of the entropy filtering operation identifying the non-acoustic contact to the left successfully.*

Case A, shown in Figure 4.6(a), shows that the entropy filtering operation identified the vessel lumen along with shadows as areas with low randomness, thus the anastomosis vessels and the shadows were represented in one object. This resulted in the object having an orientation of 140 degrees, and thereby did not fulfill the criterion for being considered as shadows or non-acoustic contact. Case B in Figure 4.6(b), showed an example of the entropy filtering operation identifying the shadows correctly but included a small part belonging to the toe of the anastomosis vessel. In this example, this object had an orientation of 85 degrees, to which it was considered as shadows or non-acoustic contact, and the pixels within the area were replaced with pixel intensities of 255. This complicated the later detection, segmentation, and patency estimation for this given frame. The last case, shown in Figure 4.6(c), the entropy filtering operation did identify the non-acoustic contact correctly, and the object's orientation of 88 degrees fulfilled the criterion, to which the area was excluded from further processing.

In order to investigate the false positive detections, examples showing the vessel candidates with the corresponding Mahalanobis distance and the detected object along with the manual anastomosis annotations are shown in Figure 4.6. The vessel candidates are shown with magenta boundaries, manually annotated anastomosis vessels are shown as yellow boundaries, and the automatically detected object with cyan boundaries.

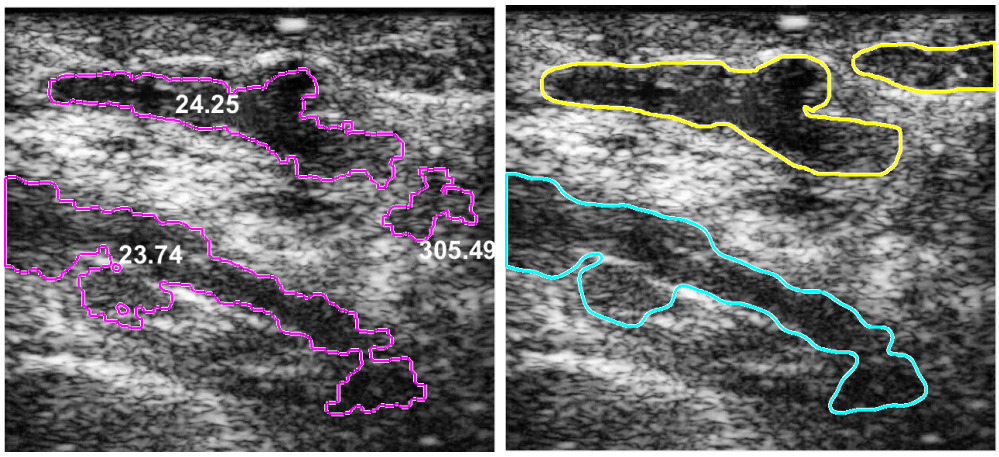


**(a)** *Vessel candidates, detected object, and the manual annotation from an EUS-frame from the development set*

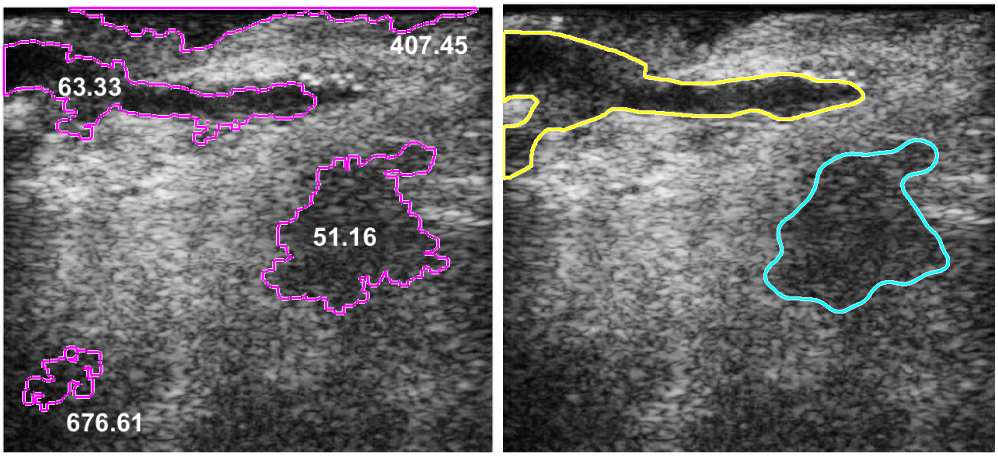


**(b)** *Vessel candidates, detected object, and the manual annotation from an EUS-frame from the test set*

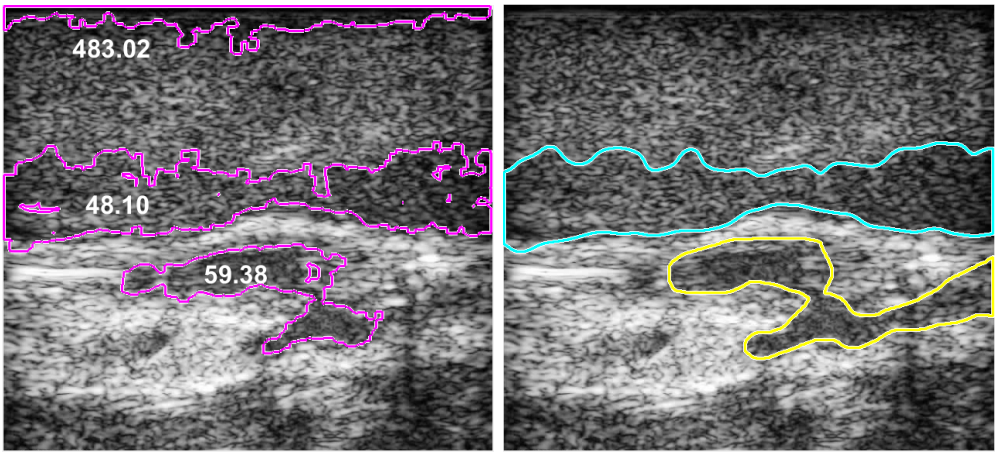


**(c)** *Vessel candidates, detected object, and the manual annotation from an EUS-frame from the test set*

***Figure 4.6:*** *Insufficient detections, where the vessel candidates and their corresponding Mahalanobis distance are visualized. Vessel candidates are represented with magenta boundaries, the detected vessels with cyan boundaries, and the manual annotated anastomosis vessels with yellow boundaries.*

The EUS-frame shown in Figure 4.7(a) belonged to the development set. In this example, three vessel candidates were identified, to which two of these represented actual vessel structures. The difference in Mahalanobis distances between these two vessel candidates was 0.51, where the Mahalanobis distance was higher for the anastomosis vessel, to which the other vessel structure was detected.
A more significant difference in Mahalanobis distance can be seen between the vessel candidates in Figure 4.7(b) and 4.7(c), which both were frames from the test set. In Figure 4.7(b) four vessel candidates were identified through the correlation calculation, to which the candidate with the lowest Mahalanobis distance did not resemble an end-to-side anastomosis. Additionally, the vessel candidate with the lowest Mahalanobis distance in Figure 4.7(c), did not appear as an end-to-side anastomosis. A tendency for the false positive detections was that the detected object appeared either as a long horizontal object or a round object similar to the two examples in Figure 4.7(b) and 4.7(c). In the two and 17 EUS-frames from the development and test set, respectively, resulting in false positive detected vessels, all contained vessel candidates representing the true anastomosis vessels.

Furthermore, the Mahalanobis distance for all the vessel candidates was investigated. In Figure 4.7, the Mahalanobis distance for the given vessel candidates in each frame are visualized, true vessel candidates are marked blue and additional vessel candidates are marked red. The maximal

Mahalanobis distance was 3,146 for the vessel candidates identified in the development set, however, only candidates with Mahalanobis distances lower than 600 were visualized in the figure, to better visualize the variation in Mahalanobis distance of the true anastomosis vessels. The insufficient detected vessels, which had a Dice coefficient lower than 0.5 and higher than 0 are represented by a magenta square. The false positive detected vessels, which had a Dice coefficient of 0, are illustrated by a magenta circle.

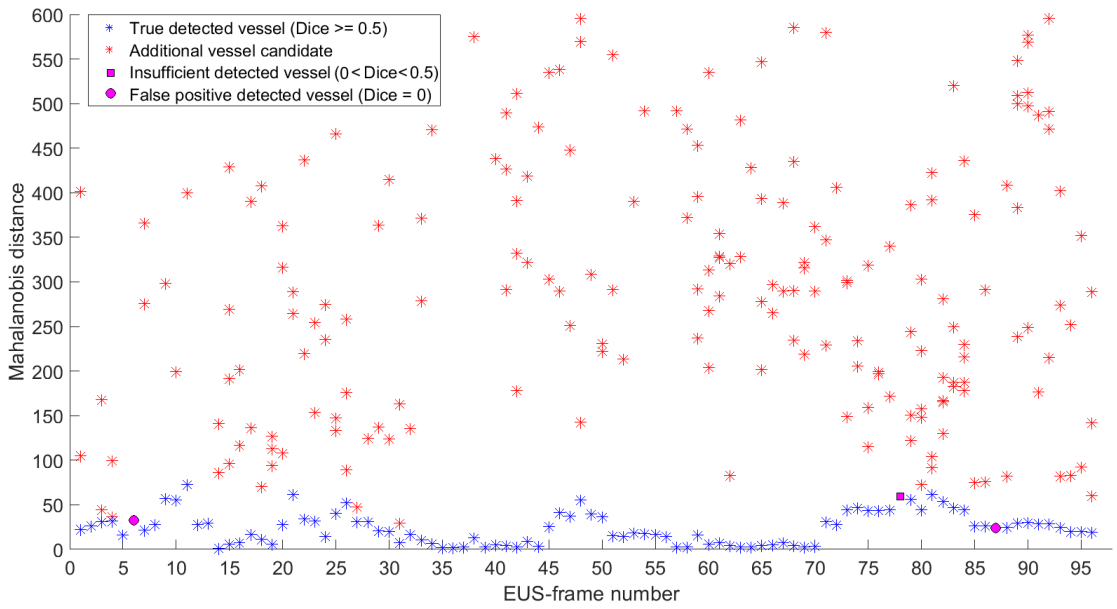


***Figure 4.7:*** *The Mahalanobis distance for the vessel candidates in each frame from the development set. The true detected vessels are represented by blue asterisks, and the presence of additional vessels candidates are represented by red asterisks. False positively detected vessels (Dice=0) are marked as magenta circles and insufficiently detected vessels (0<Dice<0.5) are illustrated with a magenta square.*

In Figure 4.7, the true detected vessels with a Dice coefficient higher than 0.5 have a relatively low Mahalanobis distance compared to the additional vessel candidates. The true detected vessels had a Mahalanobis distance in the interval $1.47 - 72.38$, to which the Mahalanobis distances for the additional vessel candidates were in the interval $29.69 - 3145.6$. A general tendency seen in Figure 4.7 is that the true vessel candidates had a Mahalanobis distance lower than 75, however additional vessel candidates were also located lower than 75. Furthermore, the two false positive detected candidates had a low Mahalanobis distance of 23.74 and 32.56.

Additionally, the Mahalanobis distances from the vessel candidates identified in the EUS-frames from the test set are shown in Figure 4.8. Not all Mahalanobis distances are plotted given the maximum distance of all vessel candidates in the test set was observed to be 3,630, thus to better visualize the variation in Mahalanobis distance of the true anastomosis vessels, the figure only included Mahalanobis distances lower than 800.

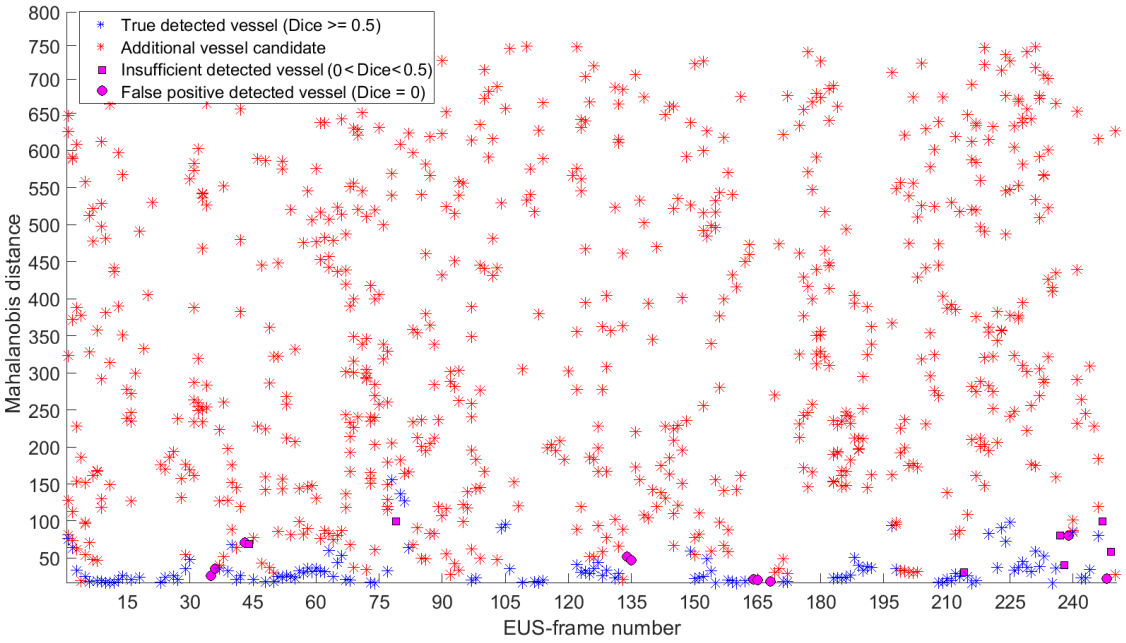


***Figure 4.8:*** *The Mahalanobis distance for the vessel candidates in each frame from the test set. The true detected vessels are represented by blue asterisks, and the presence of additional vessels candidates are represented by red asterisks. False positively detected vessels (Dice=0) are marked as magenta circles and insufficiently detected vessels (0<Dice<0.5) are illustrated with a magenta square.*

A similar tendency was observed in the Mahalanobis distances for the vessel candidates achieved in the test set, as seen in Figure 4.8. However, several true anastomosis vessels appeared with a higher Mahalanobis distance, as seen in the EUS-frames in the interval 78-81. One of these EUS-frames, which had a Mahalanobis distance of 156.2, are shown in Figure 4.9.

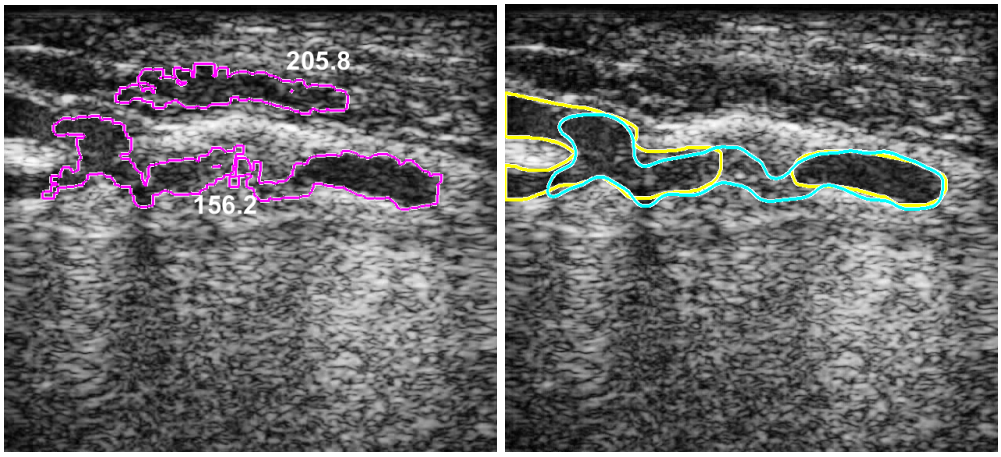


***Figure 4.9:*** *Vessel candidates and the detected anastomosis vessel along with the manually annotated anastomosis vessels from EUS-frame number 80. The vessel candidates are represented by the magenta boundaries, the detection is represented by the cyan boundary, and the manual anastomosis annotation is represented by the yellow boundary.*

In Figure 4.9 the vessel candidate with the Mahalanobis distance of 156.2 represents the true anastomosis vessels, despite having a relatively high Mahalanobis distance. The lowest and highest Mahalanobis distance achieved among all vessel candidates in the test set were 1.49 and 3630.3, respectively.

Of the 91.15 % of the anastomosis vessels that were sufficiently detected from the test set, 9.31 % of these had a Dice coefficient of 0.9 or higher. To investigate how well these anastomosis vessels were estimated by the vessel lumen detection, two examples that resulted in high Dice coefficients are shown in Figure 4.10.

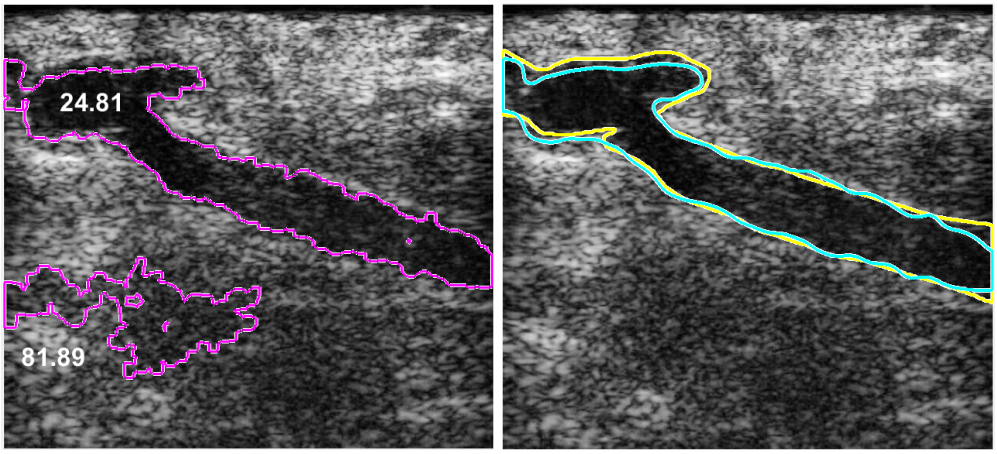


**(a)** *Dice coefficient of 0.9197*

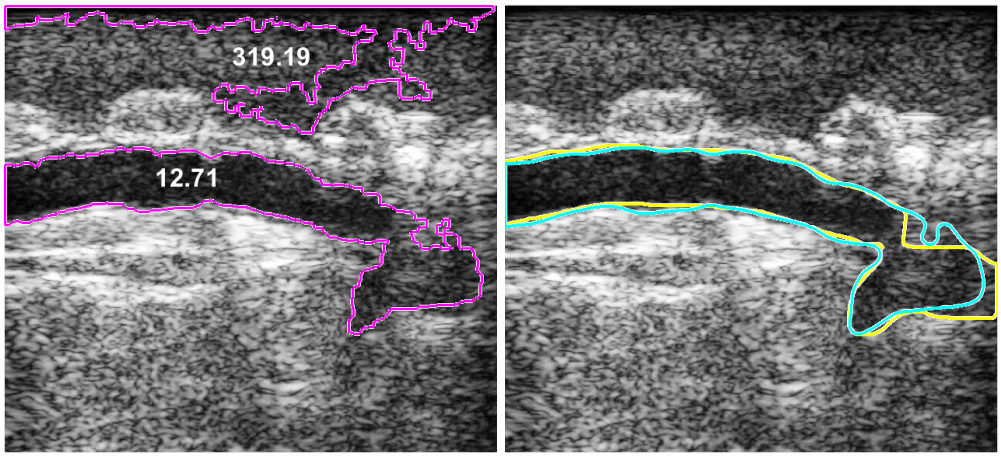


**(b)** *Dice coefficient of 0.9198*

***Figure 4.10:*** *Examples of two EUS-frames from the test set with the corresponding vessel candidates, where the detection resulted in a Dice coefficient higher than 0.9. The vessel candidates are represented by magenta, manual anastomosis annotations are represented by the yellow boundaries, and the cyan boundaries represent the detected object.*

In Figure 4.10 the boundary of the detected vessel is closely estimated to the manual anastomosis annotation. However, the detected boundary in Figure 4.10(b) is slightly overestimated as it is placed outside of the vessel lumen near the anastomosis orifice and coronary artery, presumably as a result of the presence of speckle. In both examples shown in Figure 4.10, the uncertainty of selecting the true anastomosis vessels was small given the significant variation between the Mahalanobis distances.

## 4.3 Vessel lumen segmentation

Results of the vessel lumen segmentations are presented as Dice similarity measures for the local-phase based snake and Chan-Vese segmentation. Examples of the segmentations are presented to state the potential weaknesses and strengths for each of the techniques when segmenting vessel lumen in EUS-frames. The mean Dice coefficient achieved for both the local-phase based snake and the Chan-Vese segmentation performed on frames from the development and test set are shown in Table 4.3. Additionally, the mean Dice coefficients of the segmentations initialized by sufficient vessel detections are shown in the table.

| | Local-Phase Based Snake | | Chan-Vese | |
|---|---|---|---|---|
| | Mean Dice for all detections | Mean Dice with sufficient detections | Mean Dice for all detections | Mean Dice with sufficient detections |
| Development set | 0.8345 (± 0.1467) | 0.8565 (± 0.0709) | 0.8493 (± 0.1559) | 0.8722 (± 0.0828) |
| Test set | 0.7577 (± 0.2258) | 0.8134 (± 0.1057) | 0.7589 (± 0.2273) | 0.8187 (± 0.1031) |

***Table 4.3:*** *Mean Dice coefficient from the local-phase based snake and Chan-Vese segmentations for both the development and test set. The mean Dice coefficient of the segmentations, which were performed with sufficient initial contours from the vessel lumen detection algorithm, are calculated.*

In Table 4.3 it is shown that the Chan-Vese algorithm performed best on the EUS-frames compared to the local-phase based snake. Comparing the segmentation Dice coefficients to the Dice coefficient from the vessel lumen detections, a minor increase of 0.0165 and 0.0177 can be observed in the test set for the local-phase based snake and Chan-Vese algorithm, respectively. As seven EUS-frames were detected as insufficient, a mean Dice coefficient was calculated when initialized using only sufficient detections. This raised the mean Dice performance of the local-phase based snake with 0.0722 and the Chan-Vese algorithm with 0.0775 in the test set. A slight variation between the segmentation algorithms can be observed, to which examples of segmentations with the lowest and highest difference between the two segmentation techniques are visualized in Figure 4.11, where the local-phase based snake segmentation is marked with a green boundary, the Chan-Vese segmentation with a red boundary, and the manual anastomosis annotations with a yellow boundary.

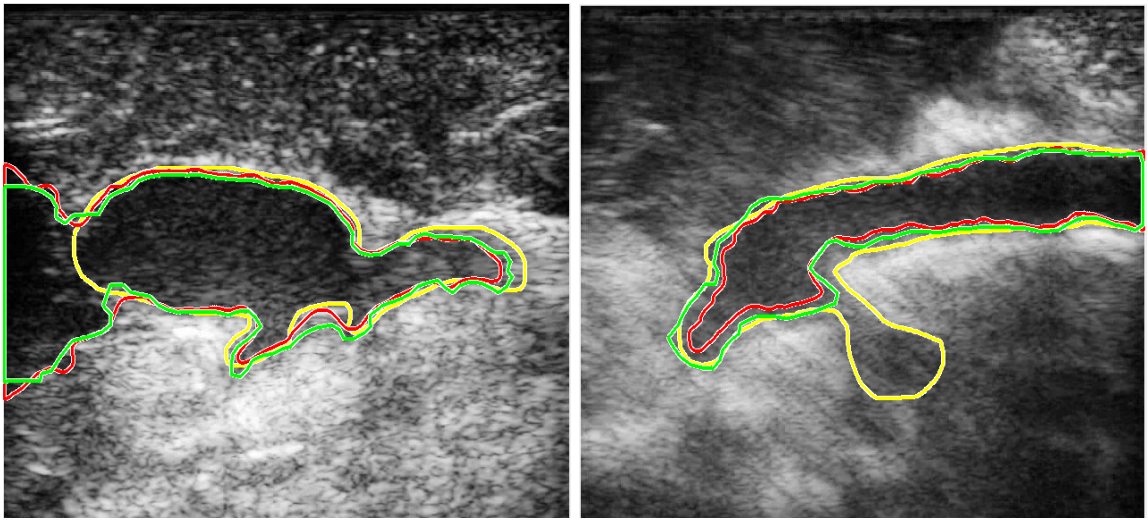

**(a)** *Dice variation of* $4.58 \times 10^{-5}$ **(b)** *Dice variation of 0.0802*

***Figure 4.11:*** *Two EUS-frames with the lowest and highest variation between the local-phase based snake and the Chan-Vese segmentation, respectively. The boundary of the local-phase based snake segmentation is green, and the boundary achieved by the Chan-Vese segmentation is red. The yellow boundary represents the manual annotation.*

In Figure 4.11(a) a small variation in Dice coefficients of $4.58 \times 10^{-5}$ was calculated between the two automatically segmented anastomosis vessels, however, the boundary of the local-phase based snake and Chan-Vese seems to vary slightly, despite the low variation between the Dice coefficients. Noticeably, the Chan-Vese segmentation was better at estimating the edge of the plaque at the lower vessel wall of the coronary artery compared to the local-phase based snake. Commonly for both segmentations, despite the overestimation of the shadowing to the left, most of the anastomosis vessels were estimated correctly by the segmentations. Thereby, the overestimation had a negative impact on the Dice coefficient, even though the boundary of the vessels was relatively accurate estimated.
The highest variation between the local-phase based snake and Chan-Vese segmentations was calculated to be 0.0802, where the segmentation boundary of the local-phase based snake and Chan-Vese are shown in Figure 4.11(b). The local-phase based snake estimated the boundary of the anastomosis vessels better with a Dice coefficient of 0.8468 compared to the Chan-Vese with a Dice coefficient of 0.7666. The main difference between the segmentations was at the toe of the anastomosis vessels where the local-phase based snake was better at estimating the edge of the vessel wall.

Furthermore, the Dice coefficients calculated for the segmentations, where the initial contour from the detection was determined insufficient, were investigated. In the vessel lumen detection, 17 EUS-frames had a Dice coefficient of 0, thus these frames also had a Dice coefficient of 0 after the segmentations. However, frames with a Dice coefficient above 0 and below 0.5, showed improvement in the Dice coefficients after segmentation. For the local-phased based snake segmentation, four of the seven EUS-frames achieved a Dice coefficient higher than 0.5 after segmentation, where the Chan-Vese segmentation only improved one frame with a Dice coefficient above 0.5 after segmentation.

Overestimation of the anastomosis vessels where side branches were included in the segmentations was observed in multiple EUS-frames, where an example is shown in Figure 4.12.

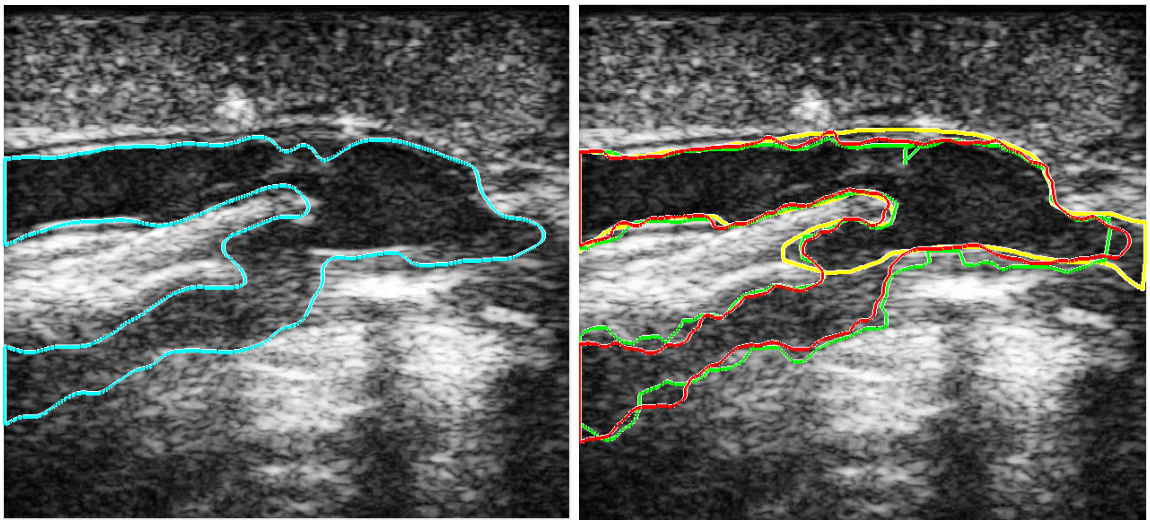

**(a)** *Detected anastomosis vessels with a Dice coefficient of 0.7428.*

**(b)** *Segmented anastomosis vessels with a Dice coefficient of 0.7331 and 0.7750 for the local-phase based snake and Chan-Vese segmentation, respectively*

***Figure 4.12:*** *An EUS-frame where elongation of the vessel appears in the detection and in the segmented boundaries. The detection boundary is marked with cyan, the boundary of the local-phase based snake segmentation is marked green, and the boundary achieved by the Chan-Vese segmentation is marked red. The yellow boundary represents the manual anastomosis annotation.*

In Figure 4.12 an overestimation of the coronary artery appears in both the detection and the segmented anastomosis vessels, which did not appear in the manual annotation. The overestimation of the coronary artery is a side branch, to which it is understandable why it is included in the segmentation. Despite the segmentations leaking into the side branch of the vessels, most of the anastomosis

vessels are captured by the segmentation algorithms. Thus, the overestimation influenced the Dice coefficient negatively, even though the boundary of the vessels was relatively accurately estimated. Similarly, this occurred in EUS-frames where shadows and non-acoustic contact were present.

Another observation that was made was that the segmentation algorithms showed a tendency to underestimate the edge of the anastomosis vessels. Two examples of this are shown in Figure 4.13.

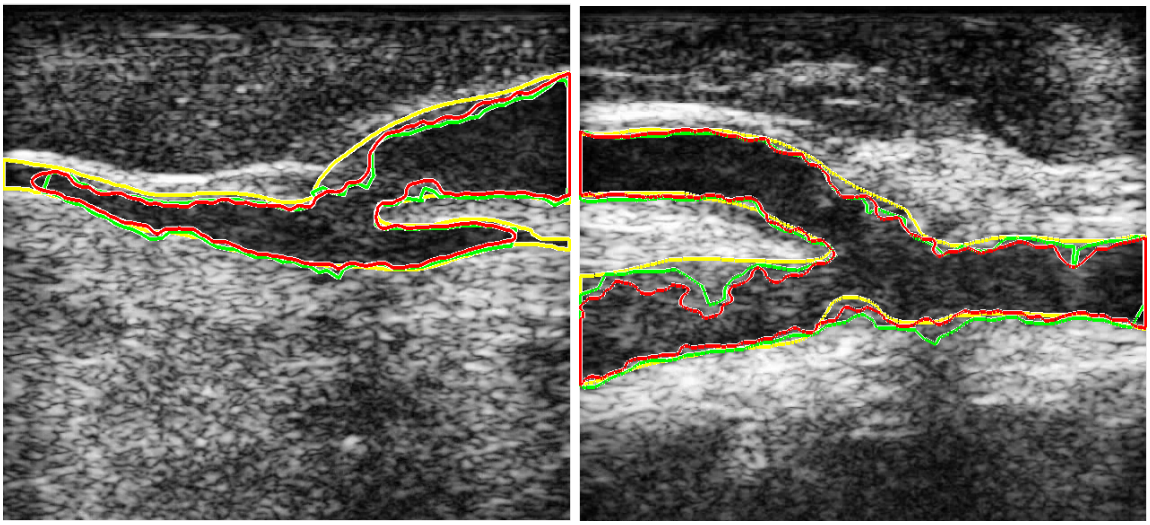

**(a)** *Dice coefficient of local-phase based snake: 0.8702 and Dice coefficient of Chan-Vese: 0.8730*

**(b)** *Dice coefficient of local-phase based snake: 0.9155 and Dice coefficient of Chan-Vese: 0.8903.*

***Figure 4.13:*** *Two EUS-frames where the segmented boundaries are located within the manual annotation. The boundary of the local-phase based snake segmentation is marked green, and the boundary achieved by the Chan-Vese segmentation is marked red. The yellow boundary represents the manual anastomosis annotation.*

In Figure 4.13(a) the boundaries of the segmentations were slightly underestimated compared to the manual anastomosis annotation. Additionally, the segmentation boundaries appeared within the manual annotation in Figure 4.13(b). In this case, the segmentations were not able to segment the edge correctly at the upper vessel wall near the heel. The area between the manual annotation and the segmentation boundaries at the heel appeared with brighter intensities, and with higher entropy, compared to the rest of the vessel lumen. The local-phase based snake estimated the boundary of the coronary artery more accurately, however, the plaque just below the anastomosis orifice was better represented in the Chan-Vese segmentation.

The highest Dice coefficients achieved in the test set for the local-phase based snake and Chan-Vese were 0.9312 and 0.9616, respectively, where the corresponding EUS-frames are shown in Figure 4.14.

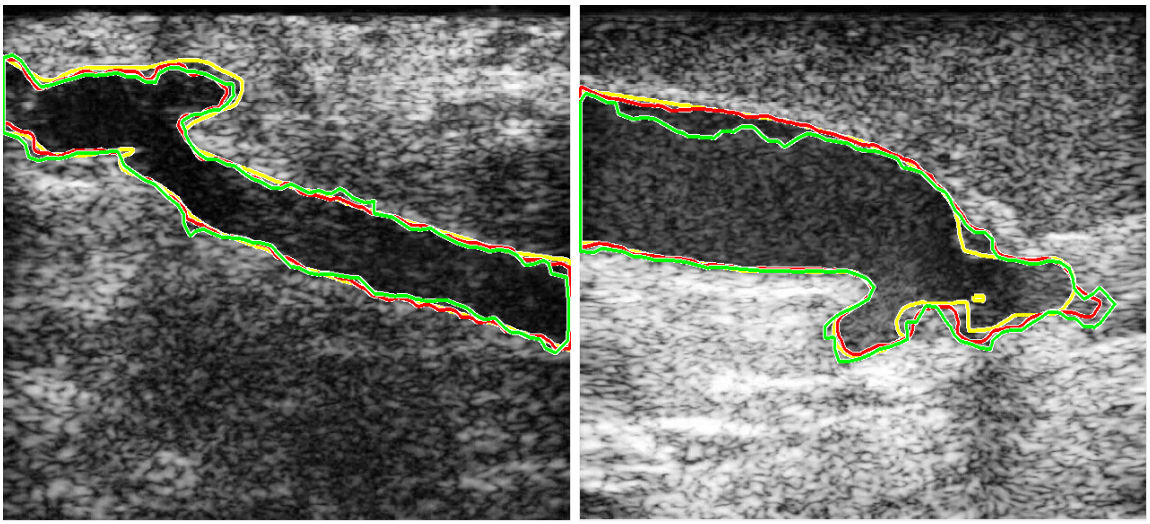

**(a)** *Dice coefficient of local-phase based snake: 0.9312 and Dice coefficient of Chan-Vese: 0.9521*

**(b)** *Dice coefficient of local-phase based snake: 0.9196 and Dice coefficient of Chan-Vese: 0.9616*

***Figure 4.14:*** *Two EUS-frames with the segmented boundaries, which resulted in the highest Dice coefficient for the local-phase based snake and Chan-Vese segmentation. The boundary of the local-phase based snake segmentation is marked green, and the boundary achieved by the Chan-Vese segmentation is marked red. The yellow boundary represents the manual annotation.*

Figure 4.14(a) shows the EUS-frame where the local-phased based snake achieved the highest Dice coefficient among all frames in the test set with a Dice coefficient of 0.9312. The Chan-Vese segmentation did, however, achieve a Dice coefficient of 0.9521, and thereby performed better than the local-phase based snake. The highest Dice coefficient for the Chan-Vese segmentation was achieved in the frame shown in Figure 4.14(b), where a Dice coefficient of 0.9616 was achieved. The local-phase based snake segmented the vessel lumen with a Dice coefficient of 0.9196 in this frame. It may be discussed whether the overestimation of the toe in Figure 4.14(b) was segmented correctly, despite the cutoff by the manual annotation, as the overestimated area appeared similar to the vessel structure of the coronary artery. Comparing the Dice coefficients achieved in Figure 4.14(a) to the Dice coefficient of the detection of the same frame, shown in Figure 4.10(a), an increase of 0.0115 and 0.0324 was observed for the local-phase based snake and Chan-Vese algorithms, respectively.

A robustness test was performed on both segmentation algorithms, where the initial contour was derived from the manual anastomosis annotations, making it independent from the vessel lumen detection. The manual annotation was eroded with a disk shaped structuring element with a radius of 10 and 20 pixels, to which the mean Dice coefficients of the segmentations are stated in Table 4.4.

| Disk radius | Dice of initial contour | Dice of local-phase based snake | Dice of Chan-Vese |
|---|---|---|---|
| 10 | 0.8423 (±0.0409) | 0.9067 (±0.0341) | 0.8957 (±0.0383) |
| 20 | 0.6197 (±0.1072) | 0.7853 (±0.1018) | 0.7921 (±0.0918) |

***Table 4.4:*** *Mean Dice coefficients for both segmentation algorithms initialized by an initial contour derived from manual annotations eroded using a disk shaped structuring element with a radius of 10 and 20 pixels.*

Table 4.4 shows that the mean Dice coefficient of the initial contour was lower before segmentation for both initial contours eroded with a disk radius of 10 and 20 pixels. The greatest increase in performance is shown as the segmentation was initiated with the contour eroded with a radius of 20 pixels. The test showed that given the initial contour was located within the vessel lumen the two segmentation algorithms were able to locate the edge of the vessel walls. Two EUS-frames are shown in Figure 4.15. Figure 4.15(a) illustrates the initial contours, where yellow is the manual annotation,

green is the contour eroded by a disk radius of 10 pixels, and the red boundary is the contour eroded with a disk radius of 20 pixels. In Figure 4.15(b) the Chan-Vese segmentation is illustrated for the two frames, the boundaries are represented with the same colors as the initial contours. Similarly, the result of the local-phase based snake segmentation is shown in Figure 4.15(c).

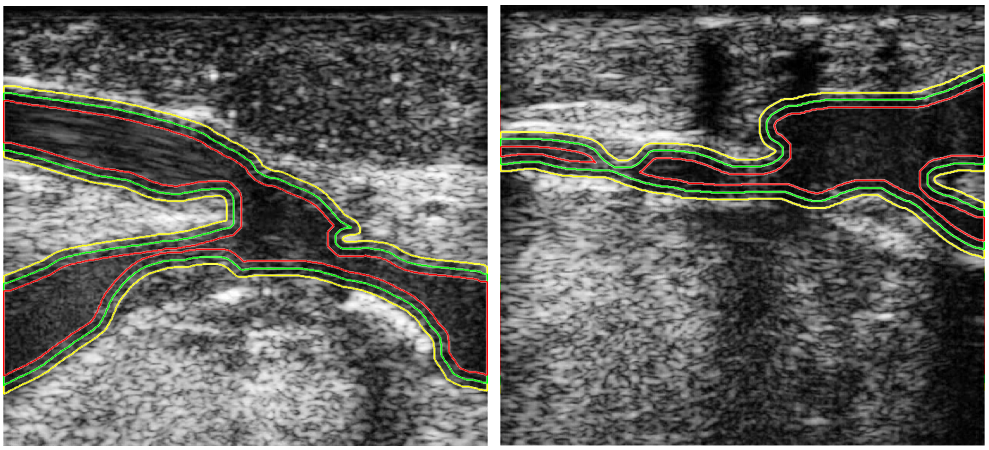

**(a)** *Initial contours*

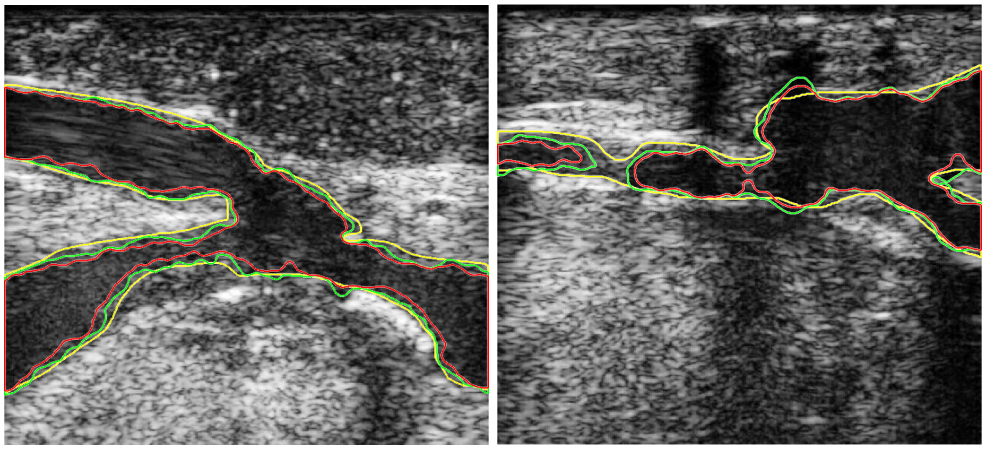

**(b)** *Chan-Vese segmentation*

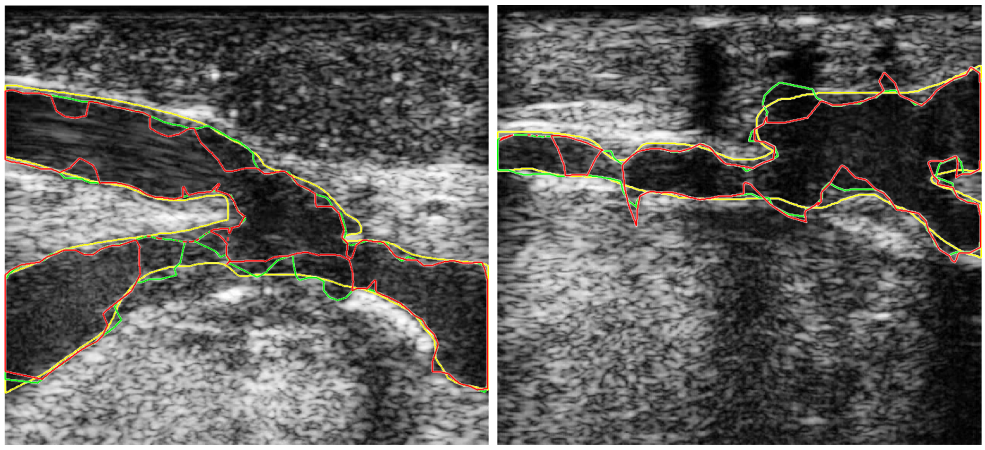

**(c)** *Local-phase based snake segmentation*

***Figure 4.15:*** *Results of subjecting local-phase based snake and Chan-Vese segmentation to varying initial contours derived from the manual annotations, marked yellow. Green boundaries represent the eroded initial contour with a disk radius of 10 pixels, and the corresponding segmentation, and red boundaries represent the initial contour eroded with a disk radius of 20 pixels with the corresponding segmentations.*

Both segmentations were able to find the edges of plaque in the frame to the left in Figure 4.15. Comparing the two segmentations, the local-phase based snake appeared more sensitive to edge information inside the vessel lumen than the Chan-Vese algorithm, when located further from the true edge. This can be seen by the red lines in Figure 4.15(c), where the Chan-Vese algorithm performed slightly better when initiated with the eroded contour using a higher disk radius. Furthermore, it is shown that the local-phase based snake segmentation, where the initial contour was narrow, had a tendency to collapse towards the same edge, which can be observed in the toe of the anastomosis vessels in the right frame in Figure 4.15(c). The Chan-Vese segmentation also showed a tendency to separate the vessels at locations near plaque as seen in the toe of the anastomosis in the right image of Figure 4.15(b).

Considering the manual annotations and the segmentations, cases were found where the boundary of the manual annotation appeared questionable. A specific example is shown in Figure 4.16.

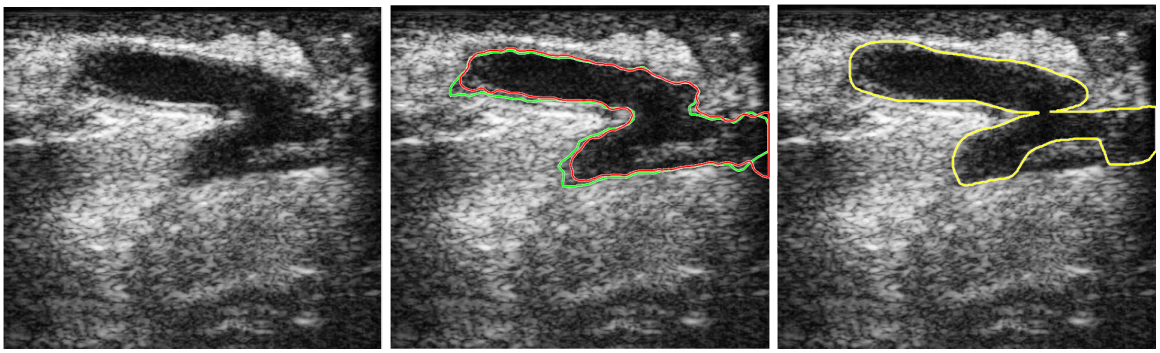

**(a)** *Original EUS-frame* **(b)** *Segmentation boundaries* **(c)** *Manual annotation*

***Figure 4.16:*** *EUS-frame where differences in the segmentation boundary and manual annotation were observed. The boundary of the local-phase based snake segmentation is marked green, and the boundary achieved by the Chan-Vese segmentation is marked red. The yellow boundary represents the manual annotation.*

From the original EUS-frame shown in Figure 4.16(a), along with the boundary of the segmentations and the manual annotation shown in Figure 4.16(b) and 4.16(c), the anastomosis orifice in the manual annotations appears very narrow. However, looking at the original EUS-frame and the segmentation boundaries the width of the anastomosis orifice appears wider, thus it is questionable whether the actual boundary near the anastomosis orifice was annotated correctly.

## 4.4 Patency estimation

The patency estimation was validated by comparing the patency estimates of the automatically and manually segmented vessels. In Figure 4.17 and Figure 4.18 the numbers of sub-optimal patency and optimal patency found of the anastomosis orifice, and at the heel- and toe site are shown.

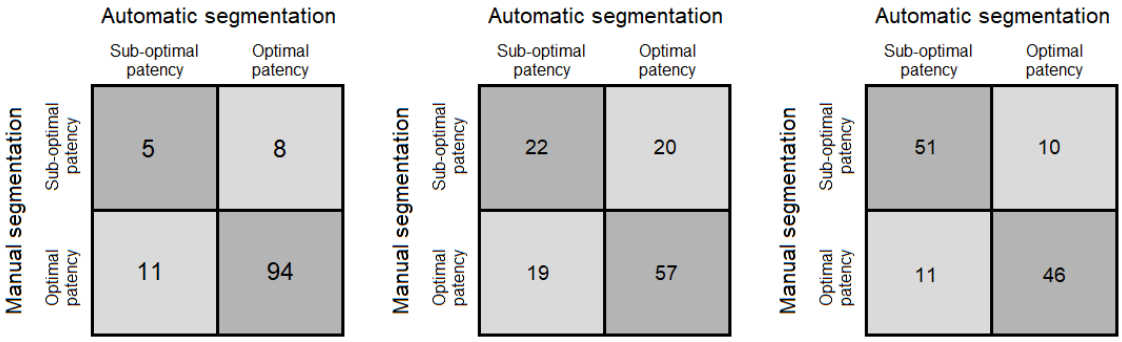


**(a)** *Anastomosis orifice* **(b)** *Heel site* **(c)** *Toe site*

***Figure 4.17:*** *The number of sub-optimal and optimal patencies found in the anastomosis orifice, heel and toe sites in all anastomosis vessels in the test set where these locations were visible in the local-phase based snake segmentations.*

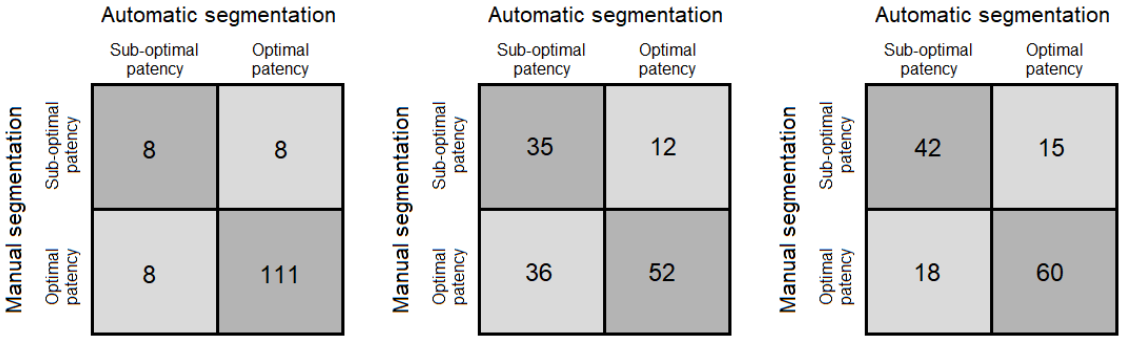


**(a)** *Anastomosis orifice* **(b)** *Heel site* **(c)** *Toe site*

***Figure 4.18:*** *The number of sub-optimal and optimal patencies found in the anastomosis orifice, heel and toe sites in all anastomosis vessels in the test set where these locations were visible in the Chan-Vese segmentations.*

Based on the figures the accuracy for estimating the patency in the anastomosis orifice, heel site, and toe site was calculated, which are shown in Table 4.5.

| | Anastomosis Orifice | Heel site | Toe site |
|---|---|---|---|
| Local-phase based snake | 83.90 % | 61.86 % | 82.29 % |
| Chan-Vese | 88.15 % | 64.44 % | 75.56 % |

***Table 4.5:*** *The performance accuracy of the patency estimation of the anastomosis orifice, heel site, and toe site for the local-phase based snake and Chan-Vese segmentation compared to manual annotations.*

As indicated by the matrices in Figure 4.17 and 4.18 and Table 4.5 the patency estimation of the anastomosis orifice and the toe site of the anastomosis performed with the highest accuracies. Comparing the two segmentations, the Chan-Vese segmentation estimated the anastomosis orifice more consistent to manual annotations, to which an accuracy of 88.15% was achieved. Contrary, the local-phase based snake estimated the toe site more consistent to manual annotations than the Chan-Vese algorithm, where a variation of 6.73% was to be seen in the performance accuracies. Both segmentation techniques showed disagreement with a higher amount of false positives and false negatives in the estimation of the heel site of the anastomosis vessels compared to the manual annotation, resulting in the performance accuracy of 61.86 % and 64.44 %.

In Figure 4.19 two EUS-frames showing disagreement between the estimation of patency was present between the manual annotated vessels and the Chan-Vese segmentation. The detection boundaries for the frames are marked in cyan, the Chan-Vese segmentations are marked in red, and the manually annotated vessel boundaries are marked in yellow. The sub-optimal patencies are marked in the frames as yellow lines, and the reference diameter is marked as green lines.

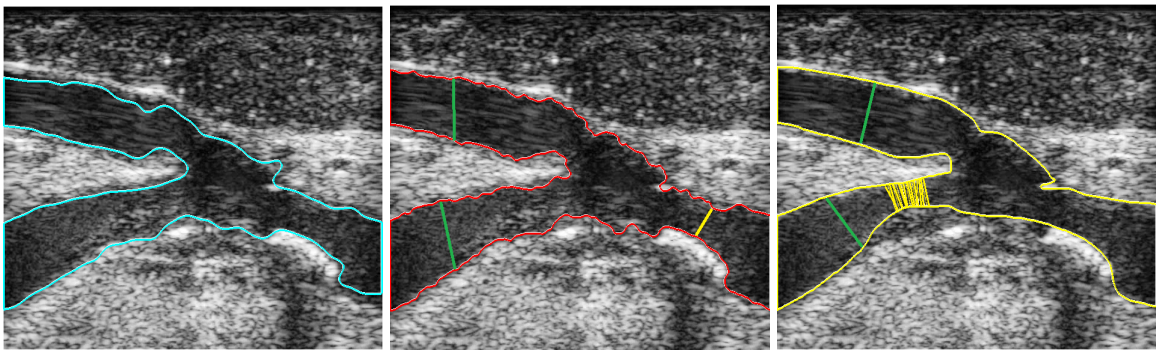

**(a)** *Detection of the vessel lumen*

**(b)** *Patency estimation on Chan-Vese segmentation*

**(c)** *Patency estimation on manual annotations*

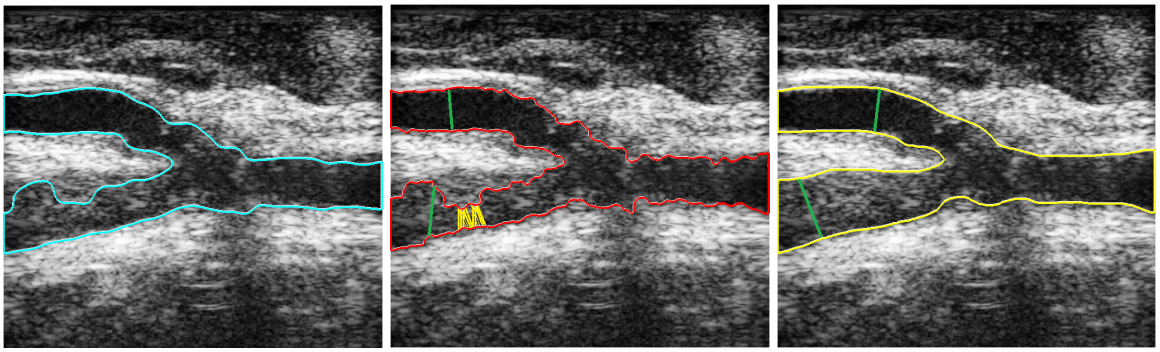

**(d)** *Detection of the vessel lumen*

**(e)** *Patency estimation on Chan-Vese segmentation*

**(f)** *Patency estimation on manual annotations*

***Figure 4.19:*** *Two EUS-frames with corresponding detection boundary, outlined cyan. A difference in patency estimation between the Chan-Vese segmentations and the manually annotated vessels is present. The Chan-Vese segmentation is oulined with a red boundary, and the manual anastomosis annotation is outlined with a yellow boundary. The sub-optimal patencies are marked with yellow lines, and the reference diameters are marked as green lines.*

In the EUS-frame shown in Figures 4.19(a), 4.19(b), and 4.19(c) the patency estimation algorithm identified sub-optimal patency at the heel site in the manually segmented vessels, while no stenoses were identified at the heel site for the Chan-Vese segmentation. However, sub-optimal patency was found at the toe site in the segmentation but not in the manual annotation. The disagreement occurred as the detection did not find the edges of the plaque at the heel site of the anastomosis vessels, to which it was included as a part of the segmented vessel lumen. Additionally, the Chan-Vese segmentation had a more jagged boundary compared to the manually segmented vessels, making it more prone to find very small areas of sub-optimal patency, as seen in Figure 4.19(c) in toe site of

the anastomosis vessels.
Conversely, segmentations occurred where soft plaque was not included in the automatic segmentation whereas these areas were included in the manual annotations, as seen in the heel site in Figure 4.19(e) and 4.19(f). Thus, the difference in patency estimations was typically as a result of the segmentation which was based on the vessel lumen detection.

In EUS-frames where the vessel lumen segmentation included surrounding structures in the segmentation, the patency estimation algorithm could find sub-optimal patency in the extra branches, as shown in Figure 4.20.

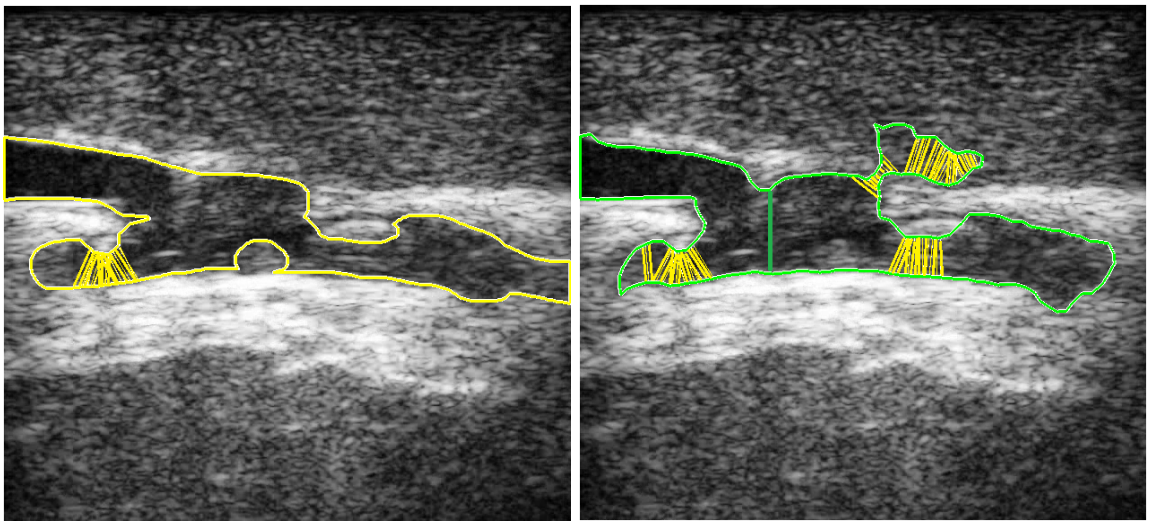

**(a)** *Manuel anastomosis annotation* **(b)** *Local-phase based snake segmentation*

***Figure 4.20:*** *Patency estimation of a manual anastomosis annotation, marked yellow, and the corresponding local-phase based snake segmentation, marked as the green boundary, where an extra branch is included in the segmentation. Sub-optimal patency is marked with yellow lines, and are present in the heel and toe site of the anastomosis vessels as well as in the extra branch.*

As shown in Figure 4.20 sub-optimal patency was highlighted in the extra branch, which was not a part of the anastomosis vessels, but the result of an overestimation. Additionally, sub-optimal patency was highlighted at the heel- and toe site of the anastomosis vessels.

A more qualitative analysis of the patency estimation was performed, where a chief physician of thoracic surgery at Aalborg University Hospital had evaluated the patency of the four anastomosis vessels shown in Figure 4.21.

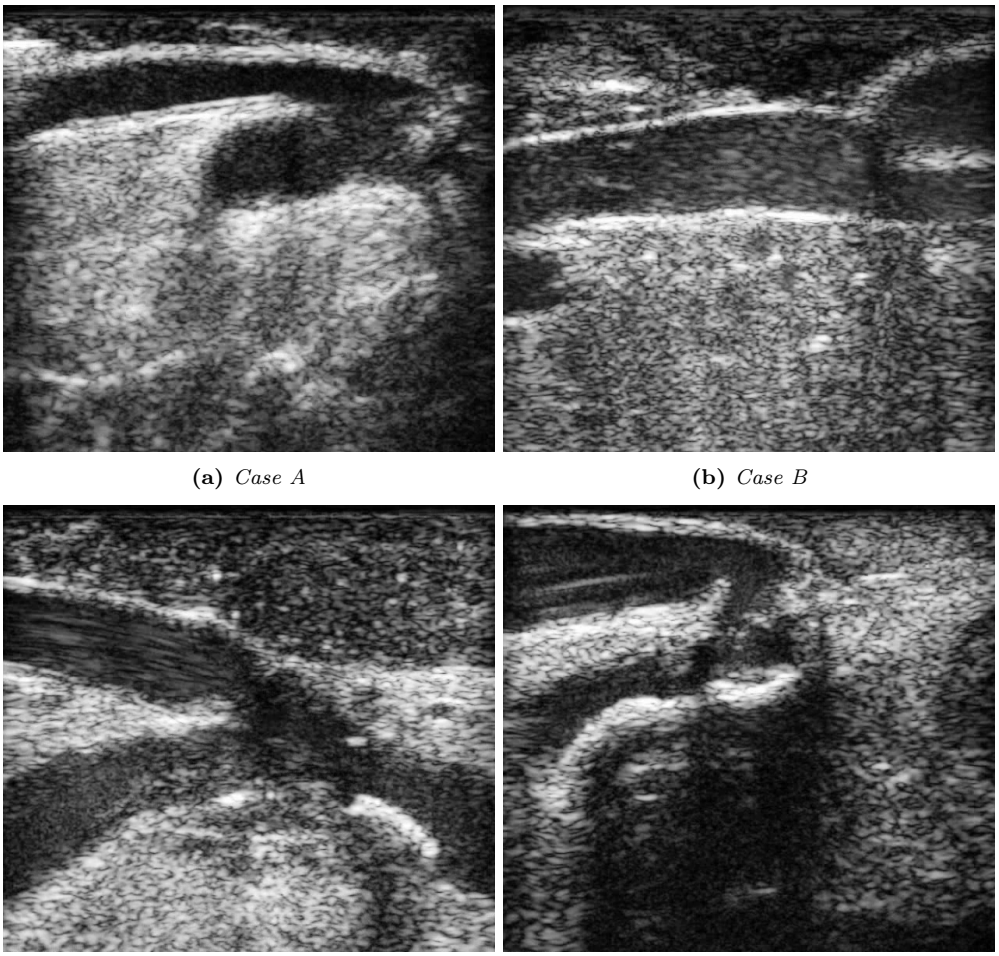

**(a)** *Case A* **(b)** *Case B*

**(c)** *Case C* **(d)** *Case D*

***Figure 4.21:*** *Specific case examples of EUS-frames that were evaluated by a chief physician of thoracic surgery at Aalborg University Hospital.*

The chief physician had the following comments to the patency of the anastomosis vessels in the four cases as seen in 4.21.

- Case A: The graft is slim, but fine patency of the anastomosis orifice
- Case B: The suture might be too tight, thus there is a stenosis in the anastomosis orifice
- Case C: Stenosis in the anastomosis orifice
- Case D: The graft appears narrowed near the anastomosis orifice

The patency estimation was performed on the local-phase based snake and Chan-Vese segmentations, where segmentations are shown in Figure 4.22, in order to identify sub-optimal patency in the four frames.

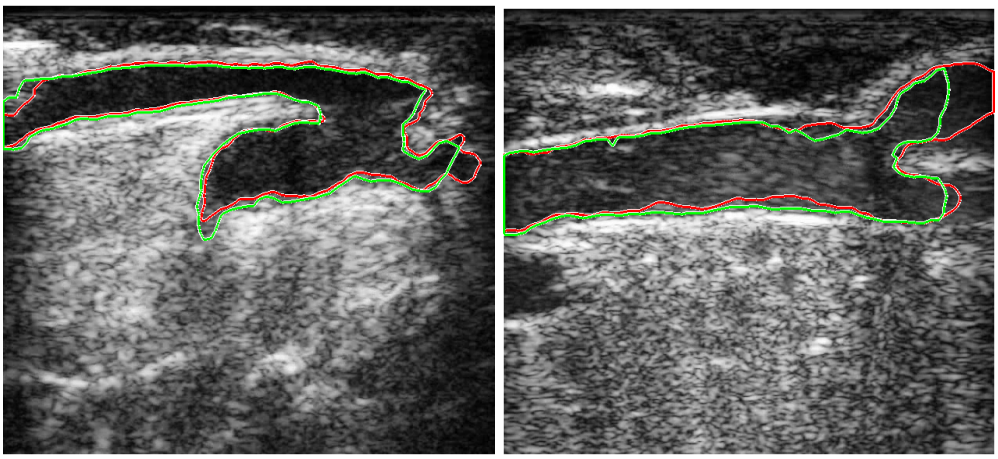

**(a)** *Case A*



**(b)** *Case B*

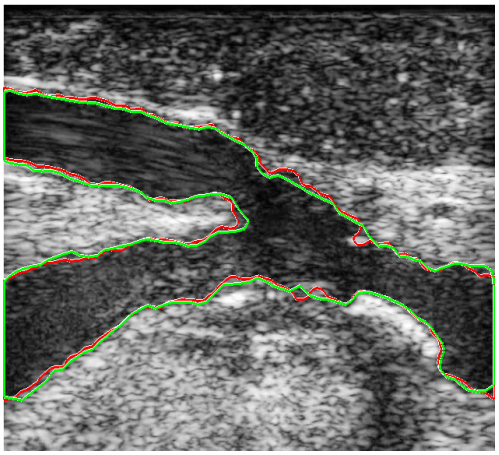

**(c)** *Case C*

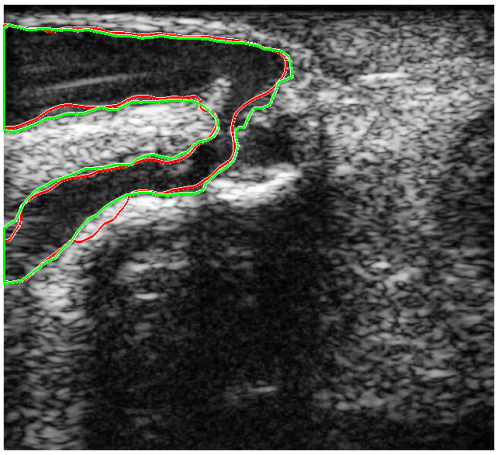

**(d)** *Case D*

***Figure 4.22:*** *The segmentations on the four cases performed by the local-phase based snake marked as the green boundary and the Chan-Vese algorithm marked with a red boundary.*

The patency was investigated in the anastomosis orifice in the automatically segmented vessels, as this was the only location of interest based on the evaluations performed by the physician. Furthermore, no stenoses were identified in the heel or toe sites in the segmentations. The manual anastomosis annotations were investigated as well to test whether sub-optimal patency was to be found in these. In Table 4.6 the reference diameter and the minimal diameter found in the anastomosis orifices are stated for the segmentations and the manual annotated anastomosis vessels. Sub-optimal patency was identified if the minimum diameter constituted a 50 % or lees of the reference diameter.

| | | Reference diameter | Minimum diameter |
|---|---|---|---|
| Case A | Local-phase based snake | 60 | 33 |
| | Chan-Vese | 56 | 35 |
| | Manual | 104 | 25 |
| Case B | Local-phase based snake | 66 | 35 |
| | Chan-Vese | 82 | 55 |
| | Manual | 90 | 70 |
| Case C | Local-phase based snake | 98 | 50 |
| | Chan-Vese | 98 | 68 |
| | Manual | 108 | 67 |
| Case D | Local-phase based snake | 66 | 25 |
| | Chan-Vese | 68 | 24 |
| | Manual | 106 | 35 |

***Table 4.6:*** *The reference diameter and the minimum diameter of the anastomosis orifice found in the local-phase based snake and Chan-Vese segmentation, as well as the manual annotation for the four cases. Sub-optimal patency was identified if the minimum diameter constituted* 50 % *or less of the reference diameter.*

The patency estimation algorithm found no sub-optimal patency in case A in either the local-phase based snake or the Chan-Vese segmentation, which was in agreement with the physician evaluation. The patency estimation of the manually segmented anastomosis vessels found sub-optimal patency in the anastomosis orifice, as the minimal diameter found was lower than 50 % of the reference diameter. The reference diameter for the manual annotation was much higher than for the two automatically segmented vessels, which was due to the algorithm finding four branches. Consequently, the reference diameter was based on the maximal reference diameter found in the segmented vessels.
The patency estimation algorithm was not able to identify sub-optimal patency in either case B or C for any of the segmentations, despite the expert identifying stenosis in the anastomosis orifice in both frames. It should be noted that the local-phase based snake segmentation was 1-2 pixels from estimating stenoses in the anastomosis orifice in case B and C. The subsequent frame in the EUS-sequence was investigated for the segmentations, to which sub-optimal patency was identified in the anastomosis orifice in the local-phase based snake in the consecutive frame in case B. The following frame had a reference diameter of 96 in the anastomosis orifice and a minimum diameter of 34, indicating the presence of a stenosis, which was in agreement with the physician's evaluation of the anastomosis. The EUS-frame with the indicated sub-optimal stenosis is illustrated in Figure 4.23.

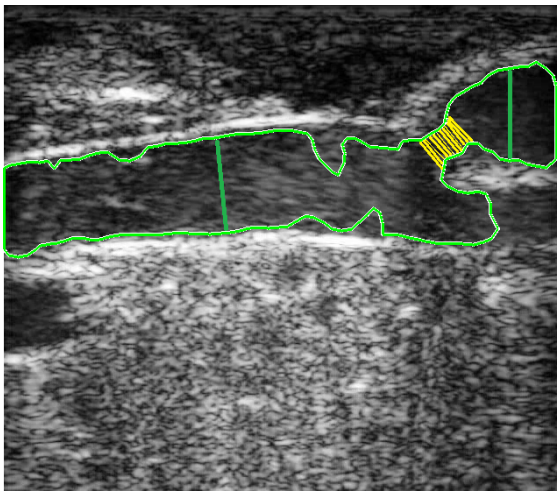

***Figure 4.23:*** *Subsequent EUS-frame to the frame in case B, where sub-optimal patency is marked in the anastomosis orifice. The patency estimation is based on the segmentation from the local-phase based snake. Sub-optimal patency is highlighted with yellow lines, and the reference diameters are marked as green lines.*

When comparing the local-phase based snake segmentation in case B, shown in Figure 4.22(b) and the segmentation of the following frame, shown in Figure 4.23, it is evident that the segmentation algorithm segmented more of the graft in the subsequent frame. This influenced the reference diameter, as the graft had a wider area in Figure 4.23, to which the anastomosis orifice was considered sub-optimal.
The patency estimation algorithm found sub-optimal patency in the anastomosis orifice in case D for both the local-phase based snake and Chan-Vese segmentation, and the manual annotation, which was in agreement with the physician evaluation of case D. In Figure 4.24 the sub-patency area in the anastomosis orifice is marked with yellow lines, the boundaries for the local-phase based snake are marked with green and the Chan-Vese segmentation is marked with red.

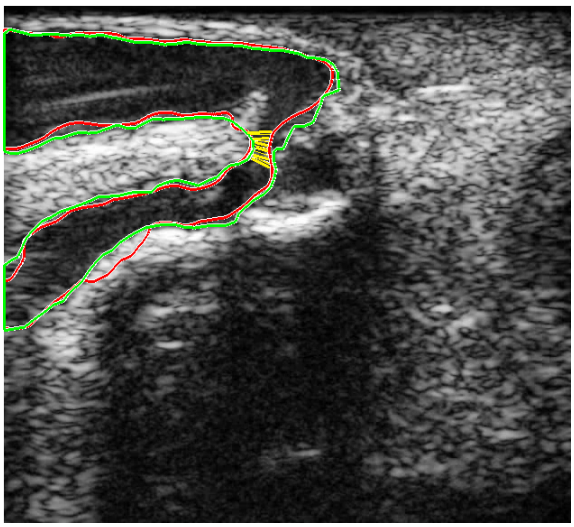

***Figure 4.24:*** *Case D, where sub-optimal patency is marked in the anastomosis orifice with yellow lines. The patency estimation is based on the segmentation from the Chan-Vese algorithm, but is similar in size and shape in the local-phase base snake segmentation. The local-phase based snake is marked green, and the Chan-Vese algorithm is marked red.*

As seen in Figure 4.24 the sub-optimal patency in the anastomosis orifice is being identified, despite the segmentation algorithms not being able to segment all of the anastomosis vessels, as the toe site is missing in both segmentations.

# 5. *Discussion*

In this chapter the methods used for designing an automatic and objective quality assessment model are discussed in terms of the performance of each of the three parts in the model; vessel lumen detection, vessel lumen segmentation, and patency estimation, as well as the overall performance of the model. Furthermore, the limitations and strengths of the model are discussed, to which further improvement of the model could be beneficial before implementing the model in practice.

## 5.1 Vessel lumen detection

The vessel lumen detection resulted in a mean Dice coefficient of 0.8149 for the development set and 0.7412 for the test set. This difference in performance between the two data sets indicated that the detection algorithm may have been developed on too few EUS-frames in order to represent the general descriptive properties of the anastomosis vessels. However, a difference in performance was expected as the detection algorithm was based on selected descriptive anastomosis features derived from the development set. Furthermore, the variation between the two mean Dice coefficients of the development and test set may partly be as a result of the 17 false positive detections in the test set, which may be as a consequence of the small development set only consisting of anastomoses from seven patients, displaying the same anastomosis vessels multiple times in the 96 EUS-frames.
The false positive detections were often round objects or longitudinal objects oriented horizontally, reflecting myocardial tissue information. This could indicate that the current features used for detecting the anastomosis vessels may be reevaluated or that more descriptive features could be included e.g. intensities or size of the object. Additionally, a feature describing the shape of the object could be included, as the traditional longitudinal end-to-side anastomosis was rarely observed circular. It could be beneficial to include more anastomosis vessels with varying appearance to deduce more general features describing the anastomosis vessels to increase the performance of the detection algorithm. However, these improvements may not accommodate for the detection algorithm not being able to differentiate between anastomosis vessel and other longitudinal vessel structures present in the EUS-frames, thus the wrong vessel structures could be detected, as observed in this project.

The initial operation in the vessel lumen detection was identification of missing acoustic contact and shadowing. Through the test of the vessel lumen detection, and subsequently the vessel lumen segmentations, it was observed that it was not always possible to exclude regions of non-acoustic contact. This was mainly as a result of low randomness in the vessel lumen, which resulted in more than the intended shadowing being identified. In these cases, the identified object did not fulfill the criterion of the orientation, thereby not considered shadowing or non-acoustic contact. A more comprehensive feature analysis of more EUS-frames containing missing acoustic contact or shadowing may be performed to better identify shadowing, or perhaps develop a classifier for classification of the regions with low entropy. However, the use of entropy filtering would not be suitable due to its tendency of considering non-acoustic contact and vessel lumen of low entropy as one object.

The detection algorithm identified several vessel candidates in the EUS-frames by using correlation between the frames and predefined templates that imitated a rough vessel structure. It could be discussed whether more tailored templates could increase the performance of the detection algorithm. For instance templates could be constructed with speckle noise or with similar intensities of the

vessels and surrounding myocardium in the given EUS-frame instead of using the extremes; black and white. Moreover, the size, angle and shape of the templates could be investigated to construct more representative correlation templates. Furthermore, additional templates could be constructed to identify shadows and non-acoustic contact in the frames.
In this project no preprocessing of the EUS-frames was performed which resulted in 91.15 % anastomosis vessels being sufficiently detected, however it may be discussed whether improvements can be achieved by despeckling or contrast enhancing in the images. Conversly these operations could reduce the edge information in the image leading to a higher risk of overestimation.
In some EUS-frames extra objects were connected to the anastomosis vessels, as a result of the merging step, where objects located within 200 pixels were merged if the mean intensities of the objects varied with less than 5 %. These extra objects were often other vessel structures present in the EUS-frame. However, the merging step prevented that only parts of the anastomosis vessels would be detected, as the model was designed to only detect one vessel candidate. An alternative approach could be to initialize the segmentation with multiple initial contours derived from more vessel candidates representing the anastomosis vessels.
The use of Mahalanobis distance identified the true anastomosis vessels in 97.92 % and 93.73 % of EUS-frames from the development and test set, to which it was indicated that anastomosis vessels could be identified with the use of Mahalanobis distance with the features; orientation, EquivDiameter, extent and deformity.
For further improvement a threshold of the Mahalanobis distance could be implemented to indicate whether a vessel candidate should be considered an anastomosis vessel. However, more frames or features could be considered implemented, as multiple alternative vessel candidates in this project had a relatively low Mahalanobis distance. Moreover, it would be possible to exclude vessel candidates based on the Mahalanobis distance, to which a vessel lumen detection was not forced to choose a vessel candidate. This could exclude detections where no anastomosis vessels were present, to which the segmentation and patency estimation should not be initiated.

The vessel lumen detection was performed on individual EUS-frames independent from the previous frames in the EUS-sequence. This limited contextual information in the sequence, as prior detection and segmentation knowledge potentially could have restricted the spatial information within a region of interest in the EUS-frame. Additionally, the prior shape information of the vessel may have been used to derive a rough initial contour of the anastomosis vessels in future frames, dependent on the amount of deformation occurring between frames.

## 5.2 Vessel lumen segmentation

The vessel lumen segmentations; local-phase based snake and Chan-Vese, had a mean Dice coefficient of 0.8134 and 0.8187, respectively, when initializing the segmentations with the vessel lumen detections that were considered sufficient in the test set. This was a relatively large improvement from using all the vessel lumen detections, including the false positively detected vessels as initial contours in the segmentation. This indicated that the two algorithms would benefit from being initialized with a curve close to the anastomosis vessel boundaries, which was also supported by the robustness test performed on the test set. According to the results of the robustness test, the local-phase based snake might be slightly more sensitive to the location of the initial curve, as this segmentation performance increased with 0.1214, when initializing the curve closer to the vessel boundary, where the Chan-Vese segmentation increased with 0.1036. This may be compatible with the theory behind the two segmentation models as the local-phase based snake deforms the curve based on local image information, where the Chan-Vese algorithm utilizes region based image information. An observation that should be taken into account when analyzing the robustness of the segmentations is that the parameters of each segmentation was identical whether the manual annotation were eroded with a disk radius of 10 or 20 pixels. Thus, the test where the manually annotated vessel was eroded with a structuring element of radius 20 pixels might need a higher maximum number of iterations for the curve to be able to reach the vessel boundary, compared to the curve that was eroded with a structuring element with a disk radius of 10. However, the use of maximum iterations as a stop criterion was preferable given the overestimation of the anastomosis vessels would be restricted. Additionally, when comparing the Dice coefficients from the segmentations to the Dice coefficients of

detections for all frames in the test set, it was apparent that the segmentation performance did not provide an overall significant improvement, and could not consistently accommodate for the possible inaccuracies of the detection. However, the segmentation of the vessel lumen was found to closely estimate the boundaries of the manual annotations, despite the lower Dice coefficients.
When comparing the segmentation performance of the local-phase based snake and the Chan-Vese algorithm, it was seen that the Chan-Vese segmentations had a slightly higher mean Dice coefficient. However, the difference in Dice coefficients between the segmentation algorithms for the test set, where insufficient detections were excluded, was only 0.0053. Despite the minor variation, the Chan-Vese segmentation appeared better to segment plaque and abrupt indentations of the vessel boundaries. Both segmentation techniques segmented the anastomosis vessels accurately despite the inclusion of shadows and non-acoustic contact, which influenced the Dice coefficients negatively.
A considerable difference between the local-phase based snake and the Chan-Vese algorithm was the ability to adapt to topological changes in the objects, as one was a parametric and the other a geometric deformable model. The initial curve, which was derived from the vessel lumen detection, was always one object due to the merging operation before using the boundary as an initial curve. In theory the Chan-Vese segmentation should be able to automatically separate the vessels in case of occlusions in the anastomosis vessels, to which the local-phase based snake segmentation could not. However, no EUS-frames in either the development- or test set showed anastomosis vessels with occlusions. However, it was observed that the Chan-Vese segmentation had a tendency to separate vessels at possible stenoses, while the local-phase based snake remained as one connected segmentation. A tendency observed of the local-phase based snake was that the snake collapsed to one edge if the initial curve was too narrow. A possible way to prevent the snake from collapsing would be to add an additional energy to the local-phase based snake algorithm, e.g. the balloon force in order to force the snake contour outwards. However, this energy could also make the local-phase based snake more susceptible to leak into shadowing or non-acoustic contact. Alternatively, the segmentation techniques could be combined, to which the level-set method could be guided by the energies derived from the phase map.

A preprocessing of the EUS-frames could potentially provide a smoother transition towards the true edge in the phase map used in the local-phase based snake algorithm. Furthermore, the amount of scaling or orientations used to derive the phase map could be analysed to find more optimal parameters. Initial experimentations of adding additional scales and orientations indicated only little to no variation to the phase map, to which the simpler setup was considered sufficient. A preprocessing of the frames, e.g. smoothing or additional intensity transformations, could influence the external weights in the Chan-Vese algorithm which were determined based on the EUS-frames smoothed with a Gaussian filter with a standard deviation of 2. Moreover, the weight modifying the internal energy in the Chan-Vese algorithm, should be tested if preprocessing was implemented.
As for the actual snake segmentation, the initial contour was uniformly parameterized for every 10 pixels from the detected vessel boundary. This was chosen as experimentations showed it to be sufficient for the snake segmentation to estimate the boundary of the vessel or plaque. However, it may be discussed whether 10 pixels were enough to catch abrupt changes in the vessel edge, which potentially could reflect suture errors.

## 5.3 Patency estimation

The patency estimation was performed on the segmented vessels from the segmentation, thus the identification of sub-optimal patency was dependent on the performance of the segmentation methods. If the segmentation was inaccurate, then the performance of the patency estimation algorithm would be affected.
The patency estimation algorithm showed an agreement between patency of anastomosis orifice in manual and automatically segmented vessels, to which accuracies of 83.90 % and 88.15 % for the local-phase based snake and Chan-Vese segmentation were achieved. The Chan-Vese segmentation was observered to estimate the boundary of the anastomosis orifice more accurately, compared to the local-phase based snake. This could be as a result of the snake being restricted by the number of control points.

The patency estimation was aimed to be used as decision support during CABG-surgery to indicate possible sub-optimal patency in the anastomosis vessels. Given that the model should be used as a decision support system the false positive sub-optimal patencies would not be considered as problematic as false negatives. The algorithm found false positively identified sub-optimal patencies in the anastomosis orifice in 9.32 % and 5.93 % for the local-phase based snake and Chan-Vese segmentation. Furthermore, 6.78 % and 5.93 % were estimated false negatively, indicating that the algorithm was more likely to estimate sub-optimal patencies in the anastomosis vessels found in the manual annotations.
The performance accuracy of the patency estimation of the toe in the anastomosis vessels were 82.29 % and 75.56 % for the local phase-based snake and Chan-Vese segmentation. This indicated that the local-phase based snake estimated the boundary at the toe of the anastomosis vessels more accurately than the Chan-Vese. Thus, a combination of the two segmentation algorithms may be preferable, as one was better at estimating the anastomosis orifice and another better at estimating the toe of the anastomosis vessels.
The algorithm resulted in a lower performance accuracy for the heel of the anastomosis vessels for both segmentations, which was a result of the heel being the most problematic part to detect and segment, as the heel often appeared small and indistinct from the surrounding myocardium.

It was observed that the segmentations of vessels in EUS-frames from the same patient could vary slightly, which consequently affected the patency estimation, to which an anastomosis could have different patency estimations. In order to accommodate for this sensitivity, the patency information from the previous EUS-frames could be taken into consideration when finding the reference diameters in the vessels. This would also be beneficial in segmentations where only a small part of the vessel was segmented.
It was observed through the patency estimation performance on the test set that the separation of the anastomosis vessels into the graft and the coronary artery was not always possible. This was due to the automatically segmented vessels not always having the characteristic "y"-shape as longitudinal end-to-side anastomoses have. If the automatically segmented vessel included extra branches, the algorithm was not able to identify which branches were the coronary artery and graft. Thus, the patency of the graft and coronary artery could not be evaluated separately based on two different reference diameters, but based on the same reference diameter. A method to accommodate for this could be to give each vessel an individual reference diameter, so that if the segmentation had included extra branches, these would be evaluated individually as well instead of based on the maximum diameter among all branches.

Consideration related to the handling of the manual annotations may also be discussed, as it was decided to include segments of the graft or coronary artery even though they were annotated as separated objects. This may have been a cause of lowering the Dice coefficients as only one vessel candidate would be chosen in the vessel detection, and that no tendency of including the segment was observed after segmentation. However, in few cases, it was observed that the vessel detection connected the segments of the vessels into one object. This could indicate that some EUS-frames contained sufficient information between the segments for them to be connected despite the separation defined in the manual annotations. An additional observation that could potentially have lowered the overall Dice coefficient of the segmentation, and caused disagreement in the patency estimation was that the manual annotation was performed on the individual vessel segments of the anastomosis. The combination of these segments may not represent the same boundary as if the anastomosis vessels were annotated as a whole.

## 5.4 Expansion of the model

The automatic quality assessment model was designed based on EUS-frames containing longitudinal end-to-side anastomoses. It may be possible to expand the model to include side-to-side anastomoses or cross sectional anastomoses as well, by modifying the three parts; vessel lumen detection, vessel lumen segmentation, and patency estimation. The vessel lumen detection was dependent of descriptive features derived from longitudinal end-to-side anastomoses, to which descriptive features from other types of anastomoses should be analyzed and implemented. However, a risk of including additional types of vessel structures in the feature analysis is the possibility of the features becoming too general to identify both types of anastomoses from the surrounding structures.
The current model used segmentation methods that were independent of the size and shape of the region of interest, to which these segmentation techniques were believed to be applicable in other segmentation problems.
The patency estimation was designed based on longitudinal vessels, to which it would be more complicated to include cross sectional vessels in this algorithm. Currently, the algorithm is able to estimate the diameter of vessels and identify sub-optimal patency in "y"-shaped structures, and was further designed to manage longitudinal end-to-side structures with extra branches as it was observed that the segmentation in some instances had extra side branches. Thus, determining the patency in side-to-side anastomoses may not be complicated to implement in the algorithm.

## 5.5 Applications

The currently proposed method is intended to provide decision support of CABG-surgery using EUS-recordings, providing an objective estimation of stenoses in the anastomoses vessels.
Implementation of the system may support physicians to intraoperatively determine whether an anastomosis requires immediate revision, eliminating additional surgery and relieve stress done to the patient. Additionally, the quality assurance support provided by the objective patency estimation may improve the long term outcome for the patient, as it would help to ensure early optimal patency of the anastomosis essential for the long term clinical outcome.
However, further investigations are recommended to improve the performance of the patency estimation, as it is currently limited to longitudinal images of anastomosis vessel. By including larger variations and types of anastomoses into the patency estimation, the method would also become more applicable as an intraoperative tool for decision support. More extensive validation tests may be performed to validate the patency estimations performance, by including larger amounts of data containing significant stenoses. The method may also be optimized for it to be used in a real-time application.

# 6. *Conclusion*

Coronary artery bypass graft surgery remains the only major vascular surgery that is not routinely intraoperatively quality assessed. The typically used methods for quality assessment are either impractical in use or may provide a false impression of the quality of the anastomosis. Epicardial ultrasonography (EUS) is a method that has shown potential for providing structural insight into the quality of anastomoses, however, the patency evaluation is currently subjective, leading to cases of missing or unnecessary revision of the anastomoses. The methods proposed in this project showed that it was possible to detect and segment vessel lumen in EUS-frames and identify sub-optimal patencies of anastomoses vessels. The performance of the methods lead to the detection of 91.15 % anastomoses with a Dice coefficient higher than 0.5. Evaluation of the segmentation results showed that the Chan-Vese algorithm performed with a higher Dice coefficient compared to the local-phase based snake. However, the difference in performance was not significant. From the 271 EUS-frames included in the test set the patency of 118 local-phase based snake segmentations and 135 segmentations performed with the Chan-Vese algorithm was investigated. Validation of the patency estimation of the anastomosis orifice resulted in a performance accuracy of 83.90% and 88.15% using the segmentations from the local-phase based snake and Chan-Vese algorithm, respectively. The overall performance of the patency estimation was 76.02% and 76.05% using the two segmentation algorithms, respectively. Further optimization of the model is recommended in order to achieve a higher and more reliable performance.

# *Acronyms*

**CABG** coronary artery bypass grafting.

**CAD** Coronary artery disease.

**CT** computed tomography.

**ECG** electrocardiography.

**EUS** epicardial ultrasonography.

**LIMA** left internal mammary artery.

**MIDCABG** minimally invasive direct coronary artery bypass grafting.

**MRI** Magnetic resonance imaging.

**OPCABG** off-pump coronary artery bypass grafting.

**PCI** percutaneous coronary intervention.

**TTFM** Transit time flowmetry.

**US** Ultrasound.

# *Bibliography*


[1] Liv Gøtzsche, Steen Pehrson, et al. *Basisbog i Medicin og Kirurgi*. Munksgaard, sixth edition, 2016. ISBN 9788762812956.

[2] Emelia J. Benjamin, Michael J. Blaha, et al. Heart Disease and Stroke Statistics—2017 Update: A Report From the American Heart Association. *Circulation*, 135(10), mar 2017. ISSN 0009-7322. doi: 10.1161/CIR.0000000000000485. URL https://www.ahajournals.org/doi/10.1161/CIR.0000000000000485.

[3] Gregory A. Roth, Catherine Johnson, et al. Global, Regional, and National Burden of Cardiovascular Diseases for 10 Causes, 1990 to 2015. *Journal of the American College of Cardiology*, 70(1):1–25, jul 2017. ISSN 07351097. doi: 10.1016/j.jacc.2017.04.052. URL https://linkinghub.elsevier.com/retrieve/pii/S0735109717372443.

[4] Allan Mattia and Frank Manetta. Medical and Surgical Management and Outcomes for Coronary Artery Disease. dec 2017. doi: 10.5772/intechopen.71979. URL http://www.intechopen.com/books/coronary-artery-bypass-graft-surgery/medical-and-surgical-management-and-outcomes-for-coronary-artery-disease.

[5] Stuart J. Head, Milan Milojevic, David P. Taggart, et al. Current Practice of State-of-the-Art Surgical Coronary Revascularization. *Circulation*, 136(14):1331–1345, oct 2017. ISSN 0009-7322. doi: 10.1161/CIRCULATIONAHA.116.022572. URL https://www.ahajournals.org/doi/10.1161/CIRCULATIONAHA.116.022572.

[6] Ragab Hani Donkol, Zizi Saad Mahmoud, et al. Evaluation of Coronary Artery Bypass by CT Coronary Angiography. dec 2017. doi: 10.5772/intechopen.70439. URL http://www.intechopen.com/books/coronary-artery-bypass-graft-surgery/evaluation-of-coronary-artery-bypass-by-ct-coronary-angiography.

[7] Thomas Frauenfelder, Evangelos Boutsianis, et al. Flow and wall shear stress in end-to-side and side-to-side anastomosis of venous coronary artery bypass grafts. *BioMedical Engineering OnLine*, 6(1):35, 2007. ISSN 1475925X. doi: 10.1186/1475-925X-6-35. URL http://biomedical-engineering-online.biomedcentral.com/articles/10.1186/1475-925X-6-35.

[8] Steven Goldman, Karen Zadina, et al. Long-term patency of saphenous vein and left internal mammary artery grafts after coronary artery bypass surgery. *Journal of the American College of Cardiology*, 44(11):2149–2156, dec 2004. ISSN 07351097. doi: 10.1016/j.jacc.2004.08.064. URL https://linkinghub.elsevier.com/retrieve/pii/S0735109704017565.

[9] Emir Mujanović, Emir Kabil, et al. Transit time flowmetry in coronary surgery–an important tool in graft verification. *Bosnian journal of basic medical sciences / Udruženje basičnih mediciniskih znanosti = Association of Basic Medical Sciences*, 7(3):275–278, 2007. ISSN 15128601. doi: 10.17305/bjbms.2007.3059.

[10] Ricardo P. J. Budde, Patricia F. A. Bakker, et al. High-frequency epicardial ultrasound: review of a multipurpose intraoperative tool for coronary surgery. *Surgical Endoscopy*, 23(3):467–476, mar 2009. ISSN 0930-2794. doi: 10.1007/s00464-008-0082-y. URL http://link.springer.com/10.1007/s00464-008-0082-y.

[11] Ricardo P.J. Budde, Rudy Meijer, et al. Detection of construction errors in ex vivo coronary artery anastomoses by 13-MHz epicardial ultrasonography. *The Journal of Thoracic and Cardiovascular Surgery*, 129(5):1078–1083, may 2005. ISSN 00225223. doi: 10.1016/j.jtcvs.2004.09.002. URL https://linkinghub.elsevier.com/retrieve/pii/S0022522304013066.

[12] Gabriele Di Giammarco, Carlo Canosa, et al. Intraoperative graft verification in coronary surgery: increased diagnostic accuracy adding high-resolution epicardial ultrasonography to transit-time flow measurement. *European Journal of Cardio-Thoracic Surgery*, 45(3):e41–e45, mar 2014. ISSN 1873-734X. doi: 10.1093/ejcts/ezt580. URL https://academic.oup.com/ejcts/article-lookup/doi/10.1093/ejcts/ezt580.

[13] Saad F. Jaber, Steven C. Koenig, et al. Role of graft flow measurement technique in anastomotic quality assessment in minimally invasive CABG. *The Annals of Thoracic Surgery*, 66(3):1087–1092, sep 1998. ISSN 00034975. doi: 10.1016/S0003-4975(98)00752-8. URL https://linkinghub.elsevier.com/retrieve/pii/S0003497598007528.

[14] Thomas C Dessing, Ricardo P.J Budde, et al. Geometry assessment of coronary artery anastomoses with construction errors by epicardial ultrasound. *European Journal of Cardio-Thoracic Surgery*, 26(2):257–261, aug 2004. ISSN 10107940. doi: 10.1016/j.ejcts.2004.05.011. URL https://academic.oup.com/ejcts/article-lookup/doi/10.1016/j.ejcts.2004.05.011.

[15] HarishBabu Ravulapalli, RanjithB Karthekeyan, et al. Intraoperative anastomotic site detection and assessment of LIMA-to-LAD anastomosis by epicardial ultrasound in off-pump coronary artery bypass grafting - A prospective single-blinded study. *Annals of Cardiac Anaesthesia*, 13 (3):231, 2010. ISSN 0971-9784. doi: 10.4103/0971-9784.69069. URL http://www.annals.in/text.asp?2010/13/3/231/69069.

[16] Dhanjoo N Ghista and Foad Kabinejadian. Coronary artery bypass grafting hemodynamics and anastomosis design: a biomedical engineering review. *BioMedical Engineering OnLine*, 12(1):129, 2013. ISSN 1475-925X. doi: 10.1186/1475-925X-12-129. URL http://biomedical-engineering-online.biomedcentral.com/articles/10.1186/1475-925X-12-129.

[17] L. Maximilian Buja. Coronary Artery Disease: Pathological Anatomy and Pathogenesis. pages 1–20, 2015. doi: 10.1007/978-1-4471-2828-1_1. URL http://link.springer.com/10.1007/978-1-4471-2828-1{_}1.

[18] Frederic H. Martini, Judi L. Nath, et al. *Fundamentals of Anatomy and Physiology*. Pearson, 2012. ISBN 978-0-321-70933-2.

[19] Kaan Kirali and Hakan Saçli. Coronary Artery Bypass Surgery. nov 2015. doi: 10.5772/61404. URL http://www.intechopen.com/books/coronary-artery-disease-assessment-surgery-prevention/coronary-artery-bypass-surgery.

[20] Jacob Fog Bentzon, Fumiyuki Otsuka, et al. Mechanisms of Plaque Formation and Rupture. *Circulation Research*, 114(12):1852–1866, jun 2014. ISSN 0009-7330. doi: 10.1161/CIRCRESAHA.114.302721. URL https://www.ahajournals.org/doi/10.1161/CIRCRESAHA.114.302721.

[21] Aldons J. Lusis. Atherosclerosis. *NATURE*, 407, 2000.

[22] Jan Nilsson. Atherosclerotic plaque vulnerability in the statin era. *European Heart Journal*, 38(21):1638–1644, jun 2017. ISSN 0195-668X. doi: 10.1093/eurheartj/ehx143. URL https://academic.oup.com/eurheartj/article-lookup/doi/10.1093/eurheartj/ehx143.

[23] Andrew Cassar, David R. Holmes, et al. Chronic Coronary Artery Disease: Diagnosis and Management. *Mayo Clinic Proceedings*, 84(12):1130–1146, dec 2009. ISSN 00256196. doi: 10.4065/mcp.2009.0391. URL https://linkinghub.elsevier.com/retrieve/pii/S0025619611603005.

[24] Christian Albus, Jörg Barkhausen, Eckart Fleck, et al. The Diagnosis of Chronic Coronary Heart Disease. *Deutsches Aerzteblatt Online*, oct 2017. ISSN 1866-0452. doi: 10.3238/arztebl.2017.0712. URL https://www.aerzteblatt.de/10.3238/arztebl.2017.0712.

[25] James T. Leung and Dominic Y. Leung. Utilization of Functional Tests Prior to and Adherence to Guidelines on Coronary Angiography. 2011.

[26] Mohanaluxmi Sriharan, Paula McParland, et al. Non-Invasive Coronary Angiography. 2010.

[27] David J. Cohen, Ben Van Hout, et al. Quality of Life after PCI with Drug-Eluting Stents or Coronary-Artery Bypass Surgery. 2011.

[28] Peter F. Ludman. Percutaneous coronary intervention. 2019.

[29] Spencer B. King, John Jeffrey Marshall, et al. Revascularization for Coronary Artery Disease: Stents Versus Bypass Surgery. *Annual Review of Medicine*, 61(1):199–213, feb 2010. ISSN 0066-4219. doi: 10.1146/annurev.med.032309.063039. URL http://www.annualreviews.org/doi/10.1146/annurev.med.032309.063039.

[30] J. E. M. Sels, W. A. L. Tonino, et al. Fractional Flow Reserve. pages 349–361, 2013. doi: 10.1007/978-3-642-27676-7_20. URL http://link.springer.com/10.1007/978-3-642-27676-7{_}20.

[31] Seung-Jung Park and Duk-Woo Park. Percutaneous Intervention for Left Main Coronary Artery Disease: Treatment for Left Main Coronary Artery Disease. pages 531–554, 2013. doi: 10.1007/978-3-642-27676-7_30. URL http://link.springer.com/10.1007/978-3-642-27676-7{_}30.

[32] MLF Brooks and DLF Brooks. *Basic medical language*. Myrna LaFleur, 4 th edition, 2015. ISBN 9780323277679.

[33] Yunpeng Ling, Liming Bao, et al. Minimally invasive direct coronary artery bypass grafting with an improved rib spreader and a new-shaped cardiac stabilizer: results of 200 consecutive cases in a single institution. *BMC Cardiovascular Disorders*, 16(1):42, dec 2016. ISSN 1471-2261. doi: 10.1186/s12872-016-0216-4. URL http://www.biomedcentral.com/1471-2261/16/42.

[34] Michael J Mack, James A Magovern, et al. Results of graft patency by immediate angiography in minimally invasive coronary artery surgery. *The Annals of Thoracic Surgery*, 68(2):383–389, aug 1999. ISSN 00034975. doi: 10.1016/S0003-4975(99)00648-7. URL http://linkinghub.elsevier.com/retrieve/pii/S0003497599006487.

[35] Rune Haaverstad, Nicola Vitale, et al. Intraoperative color Doppler ultrasound assessment of LIMA-to-LAD anastomoses in off-pump coronary artery bypass grafting. *The Annals of Thoracic Surgery*, 74(4):1390–1394, oct 2002. ISSN 00034975. doi: 10.1016/S0003-4975(02)04058-4. URL http://linkinghub.elsevier.com/retrieve/pii/S0003497502040584.

[36] Peter B. Berger, Edwin L. Alderman, et al. Frequency of Early Occlusion and Stenosis in a Left Internal Mammary Artery to Left Anterior Descending Artery Bypass Graft After Surgery Through a Median Sternotomy on Conventional Bypass. *Circulation*, 100(23):2353–2358, dec 1999. ISSN 0009-7322. doi: 10.1161/01.CIR.100.23.2353. URL https://www.ahajournals.org/doi/10.1161/01.CIR.100.23.2353.

[37] Gerald M. Fitzgibbon, Henryk P. Kafka, et al. Coronary bypass graft fate and patient outcome: Angiographic follow-up of 5,065 grafts related to survival and reoperation in 1,388 patients during 25 years. *Journal of the American College of Cardiology*, 28(3):616–626, sep 1996. ISSN 07351097. doi: 10.1016/0735-1097(96)00206-9. URL https://linkinghub.elsevier.com/retrieve/pii/0735109796002069.

[38] Hubert Stein, John Michael Smith, et al. Target Vessel Detection and Coronary Anastomosis Assessment by Intraoperative 12-MHz Ultrasound. *The Annals of Thoracic Surgery*, 82(3):1078–1084, sep 2006. ISSN 00034975. doi: 10.1016/j.athoracsur.2006.03.040. URL https://linkinghub.elsevier.com/retrieve/pii/S0003497506005868.

[39] Janne J. Jokinen, Kalervo Werkkala, et al. Clinical value of intra-operative transit-time flow measurement for coronary artery bypass grafting: a prospective angiography-controlled study. *European Journal of Cardio-Thoracic Surgery*, 39(6):918–923, jun 2011. ISSN 10107940. doi:

10.1016/j.ejcts.2010.10.006. URL https://academic.oup.com/ejcts/article-lookup/doi/10.1016/j.ejcts.2010.10.006.

[40] Sanaz Amin, Raphael S. Werner, et al. Intraoperative Bypass Graft Flow Measurement With Transit Time Flowmetry: A Clinical Assessment. *The Annals of Thoracic Surgery*, 106(2): 532–538, aug 2018. ISSN 00034975. doi: 10.1016/j.athoracsur.2018.02.067. URL https://linkinghub.elsevier.com/retrieve/pii/S0003497518304077.

[41] Michael J Mack. Intraoperative coronary graft assessment. *Current Opinion in Cardiology*, 23 (6):568–572, nov 2008. ISSN 0268-4705. doi: 10.1097/HCO.0b013e3283121cbf. URL https://insights.ovid.com/crossref?an=00001573-200811000-00008.

[42] Guido Beldi, Andreas Bosshard, et al. Transit time flow measurement: experimental validation and comparison of three different systems. *The Annals of Thoracic Surgery*, 70(1):212–217, jul 2000. ISSN 00034975. doi: 10.1016/S0003-4975(00)01246-7. URL http://linkinghub.elsevier.com/retrieve/pii/S0003497500012467.

[43] Gabriele Di Giammarco, Pano, et al. Predictive value of intraoperative transit-time flow measurement for short-term graft patency in coronary surgery. *The Journal of Thoracic and Cardiovascular Surgery*, 132(3):468–474, sep 2006. ISSN 00225223. doi: 10.1016/j.jtcvs.2006.02.014. URL https://linkinghub.elsevier.com/retrieve/pii/S0022522306003187.

[44] L. F. Hiratzka, D. D. McPherson, et al. Intraoperative evaluation of coronary artery bypass graft anastomoses with high-frequency epicardial echocardiography: Experimental validation and initial patient studies. *Circulation*, 73(6):1199–1205, 1986. ISSN 00097322. doi: 10.1161/01.CIR.73.6.1199.

[45] Alex Skovsbo Jørgensen, Samuel Emil Schmidt, et al. An Improved Algorithm for Coronary Bypass Anastomosis Segmentation in Epicardial Ultrasound Sequences. *Ultrasound in Medicine & Biology*, 42(12):3010–3021, dec 2016. ISSN 03015629. doi: 10.1016/j.ultrasmedbio.2016.07.014. URL https://linkinghub.elsevier.com/retrieve/pii/S0301562916301739.

[46] André M. F. Santos, Jão Manuel R. S. Tavares, et al. Automatic segmentation of the lumen of the carotid artery in ultrasound B-mode images. page 86703I, feb 2013. doi: 10.1117/12.2007259. URL http://proceedings.spiedigitallibrary.org/proceeding.aspx?doi=10.1117/12.2007259.

[47] Lei Ma, Hidemichi Kiyomatsu, et al. Accurate vessel segmentation in ultrasound images using a local-phase-based snake. *Biomedical Signal Processing and Control*, 43:236–243, may 2018. ISSN 17468094. doi: 10.1016/j.bspc.2018.03.002. URL https://linkinghub.elsevier.com/retrieve/pii/S1746809418300624.

[48] Mehdi Hassan, Asmatullah Chaudhry, et al. Robust information gain based fuzzy c-means clustering and classification of carotid artery ultrasound images. *Computer Methods and Programs in Biomedicine*, 113(2):593–609, feb 2014. ISSN 01692607. doi: 10.1016/j.cmpb.2013.10.012. URL https://linkinghub.elsevier.com/retrieve/pii/S0169260713003544.

[49] Medistim. MiraQ Cardiac. URL https://medistim.com/our{_}products/miraq-cardiac/.

[50] Kristen M. Meiburger, U. Rajendra Acharya, et al. Automated localization and segmentation techniques for B-mode ultrasound images: A review. *Computers in Biology and Medicine*, 92: 210–235, jan 2018. ISSN 00104825. doi: 10.1016/j.compbiomed.2017.11.018. URL https://linkinghub.elsevier.com/retrieve/pii/S0010482517303888.

[51] Tejas Sudharshan Mathai, Lingbo Jin, et al. Fast Vessel Segmentation and Tracking in Ultra High-Frequency Ultrasound Images. jul 2018. URL http://arxiv.org/abs/1807.08784.

[52] Faouzi Benzarti and Hamid Amiri. Speckle Noise Reduction in Medical Ultrasound Images. 2012.

[53] Ricardo G. Dantas, Eduardo T. Costa, et al. Ultrasound speckle and equivalent scatterers. *Ultrasonics*, 43(6):405–420, may 2005. ISSN 0041624X. doi: 10.1016/j.ultras.2004.11.003. URL https://linkinghub.elsevier.com/retrieve/pii/S0041624X04003063.

[54] Niels-Henrik Staalsen, Benedict Kjaergaard, et al. A new technique facilitating intraoperative, high-frequency echocardiography of coronary bypass graft anastomoses. *The Journal of Thoracic and Cardiovascular Surgery*, 141(1):295–296, jan 2011. ISSN 00225223. doi: 10.1016/j.jtcvs.2009.11.074. URL https://linkinghub.elsevier.com/retrieve/pii/S0022522310012717.

[55] Rui Rocha, Jorge Silva, et al. Automatic detection of the carotid lumen axis in B-mode ultrasound images. *Computer Methods and Programs in Biomedicine*, 115(3):110–118, jul 2014. ISSN 01692607. doi: 10.1016/j.cmpb.2014.04.004. URL https://linkinghub.elsevier.com/retrieve/pii/S0169260714001291.

[56] Rafael C. Gonzalez and Richard E. Woods. Representation and Description. 2003.

[57] J. P. Lewis. Fast Normalized Cross-Correlation. *Vision Interface*, 1995.

[58] Panagiotis Moutafis, Mengjun Leng, et al. An Overview and Empirical Comparison of Distance Metric Learning Methods. *IEEE Transactions on Cybernetics*, 47(3):612–625, 2017. ISSN 2168-2267. doi: 10.1109/TCYB.2016.2521767. URL http://ieeexplore.ieee.org/document/7407637/.

[59] Tim McInerney and Demetri Terzopoulos. Deformable models in medical image analysis: a survey. *Medical Image Analysis*, 1(2):91–108, jun 1996. ISSN 13618415. doi: 10.1016/S1361-8415(96)80007-7. URL https://linkinghub.elsevier.com/retrieve/pii/S1361841596800077.

[60] Y. Bai, X. Han, et al. Geometric Deformable Models. 2015. doi: 10.1007/978-0-387-09749-7__5.

[61] Chenyang Xu, Dzung Pham, et al. Image Segmentation Using Deformable Models. pages 129–174, 2000. doi: 10.1117/3.831079.ch3. URL http://ebooks.spiedigitallibrary.org/content.aspx?doi=10.1117/3.831079.ch3.

[62] Pamela Juneja and Ramgopal Kashyap. Energy based Methods for Medical Image Segmentation. *International Journal of Computer Applications*, 146(6), 2016.

[63] Gavriil Tsechpenakis. Deformable Model-Based Medical Image Segmentation. pages 33–67, 2011. doi: 10.1007/978-1-4419-8195-0_2. URL http://link.springer.com/10.1007/978-1-4419-8195-0{_}2.

[64] Gunnar Lathen, Jimmy Jonasson, et al. Phase based level set segmentation of blood vessels. pages 1–4, dec 2008. ISSN 1051-4651. doi: 10.1109/ICPR.2008.4760970. URL http://ieeexplore.ieee.org/document/4760970/.

[65] E H Adelson, Hans C. Andersen, et al. Pyramid methods in image processing. *RCA engineer*, 29(6):33–41, 1984. doi: 10.1.1.59.9419. URL http://citeseerx.ist.psu.edu/viewdoc/download?doi=10.1.1.59.9419{\&}rep=rep1{\&}type=pdf.

[66] Chunliang Wang and Örjan Smedby. Multi-organ Segmentation Using Shape Model Guided Local Phase Analysis. pages 149–156, 2015. doi: 10.1007/978-3-319-24574-4_18. URL http://link.springer.com/10.1007/978-3-319-24574-4{_}18.

[67] Lishui Cheng, Jie Yang, Xian Fan, and Yuemin Zhu. A Generalized Level Set Formulation of the Mumford-Shah Functional for Brain MR Image Segmentation. pages 418–430, 2005. doi: 10.1007/11505730_35. URL http://link.springer.com/10.1007/11505730{_}35.

[68] M. Airouche, L. Bentabet, et al. Image Segmentation Using Active Contour Model and Level Set Method Applied to Detect Oil Spills. *Proceedings of the World Congress on Engineering*, 2009.

[69] Tony F. Chan and Luminita A. Vese.

[70] Pascal Getreuer. Chan-Vese Segmentation. *Image Processing On Line*, 2:214–224, aug 2012. ISSN 2105-1232. doi: 10.5201/ipol.2012.g-cv. URL http://www.ipol.im/pub/art/2012/g-cv/?utm{_}source=doi.